THE FALLING-STAGE PROGRADATION OF AN OPEN-COAST TIDAL FLAT: UAV-ASSISTED SEQUENCE STRATIGRAPHY OF THE JURASSIC WINDY HILL SANDSTONE, WYOMING U.S.A.

by

SARAH N. WRIGHT

(Under the Direction of Steven M. Holland)

ABSTRACT

The Jurassic Windy Hill Sandstone in Wyoming contains features consistent with deposition on an open-coast tidal flat, like those along the coast of Korea today, and this study uses field and UAV-based methods to investigate the sequence stratigraphic context of these deposits. Surfaces of forced regression are present and indicate deposition in the FSST and LST, re-enforcing the idea that tidal deposition can occur in many contexts. The recognition of surfaces of forced regression at stratigraphic positions previously interpreted as the J5 unconformity suggest that this surface may be at a stratigraphically higher position, implying that portions of the Redwater Shale, Windy Hill Sandstone, and Morrison Formation are contemporaneous in Wyoming. The Morrison Formation displays continuous progradation that is attributed to a slowed rate of tectonic subsidence, illustrating how tectonics can result in deviations from predicted sequence stratigraphic architecture, with the TST apparently absent from the rock record.

INDEX WORDS: Sequence Stratigraphy, Falling Stage Systems Tract, Tidal Flat, UAV, Windy Hill Sandstone, Sundance Formation

THE FALLING-STAGE PROGRADATION OF AN OPEN-COAST TIDAL FLAT: UAV-ASSISTED SEQUENCE STRATIGRAPHY OF THE JURASSIC WINDY HILL SANDSTONE, WYOMING U.S.A.

by

SARAH N. WRIGHT

B.S., University of New Mexico, 2015

A Thesis Submitted to the Graduate Faculty of The University of Georgia in Partial Fulfillment of the Requirements for the Degree

MASTER OF SCIENCE

ATHENS, GEORGIA

2017

THE FALLING-STAGE PROGRADATION OF AN OPEN-COAST TIDAL FLAT: UAV-ASSISTED SEQUENCE STRATIGRAPHY OF THE JURASSIC WINDY HILL SANDSTONE, WYOMING U.S.A.

by

SARAH N. WRIGHT

Major Professor:	Steven M. Holland
Committee:	David S. Leigh
	Clark R. Alexander, Jr.

Electronic Version Approved:

Suzanne Barbour
Dean of the Graduate School
The University of Georgia
December 2017

DEDICATION

This work is dedicated to all the people in my life who have worked so hard to make it possible for me to get an education and enjoy doing it. To my family, for always supporting me and being wonderful role models, to Erik, for being my rock among rocks, and to Marty 'GMa' Allard, for showing me all the things that hard work and perseverance can accomplish and for the constant effort that has put so many people—past, present, and future—in positions to succeed and experience a better world. Thank you.

ACKNOWLEDGEMENTS

Many thanks go out to Steve Holland for being a patient and understanding advisor who was always willing to help and whose guidance made this project possible. I am also grateful to David Leigh and Clark Alexander for serving on my committee and asking insightful questions along the way. Thank you also to Carson Walters for assistance in the field and Melissa Connely for suggesting outcrop localities and showing us valuable field areas in Wyoming.

My gratitude also goes out to the Geological Society of America, the American Association of Petroleum Geologists, the Tobacco Root Geological Association, the Wyoming Geological Association, and the Miriam Watts-Wheeler fund for generously funding field work and other expenses of this research project.

TABLE OF CONTENTS

APPENDICES

LIST OF TABLES

LIST OF FIGURES

Page

CHAPTER 1

INTRODUCTION AND LITERATURE REVIEW

This thesis has been organized into four chapters. This chapter introduces general concepts that led to the development of this project and summarizes previous research. Chapter two outlines the development and testing of unmanned aerial vehicle (UAV)-based research methods that were applied to a sequence stratigraphic research project that comprises the bulk of this thesis and is discussed in the third chapter. Chapter three is written as a manuscript to be submitted to the *Journal of Sedimentary Research*. The fourth and final chapter outlines the conclusions from this research.

Field geology is often limited by topographic obstacles. Rough terrain, deep gullies, and cliffs deny researchers access to sites that could provide critical evidence to support or reject an interpretation. Topographic obstacles result in gaps between lithologic columns measured for stratigraphic analyses. Physical gaps do not have to be excessively large to be accompanied by data gaps that can completely change interpretations. Erosional relief, for example, can be such that surfaces at different outcrops may appear to be at the same level and be incorrectly correlated to one another when they are of different ages (Fig. 1.1). Some researchers use closely spaced sections (~0.5 km apart; Fig. 1.1) and field tracing of contacts to avoid this issue presented by data gaps (Zhu et al. 2012). This is an effective but tedious method and recent advances in modern technology such as unmanned aerial vehicles, or UAVs, has opened new and more efficient avenues for data collection (Carrivick et al., 2013; Jordan 2015). UAV-based data has many similar applications to lidar data and terrestrial laser scanning, such as the digital reconstruction of planar geologic features such as faults and bedding (García-Sellés et al. 2011). Ground-based lidar and three-dimensional surface modelling can also be used to examine complex internal architecture associated with erosional surfaces (Phelps et al. 2008). Quadcopter UAVs can also be used to this end, allowing surfaces to be traced between outcrops for better correlations. Additionally, 3D point-cloud models of outcrops provide a way to digitally measure stratigraphic columns, allowing variability to be characterized and data gaps to be minimized. The Jurassic Windy Hill Sandstone of the Sundance Formation is a thin but complex sandstone containing previously interpreted erosional surfaces and often outcropping as cliffs or ridges, making it ideal for the application of UAV-based stratigraphic methods.

The Jurassic Sundance Formation has been a topic of geologic interest for well over fifty years. Imlay (1956) described and correlated the formation in portions of Wyoming, Montana, and South Dakota. Pipiringos (1968) described and named the Windy Hill Sandstone as a member of the Sundance Formation. Prior to this, equivalent intervals were described as the "Upper Sundance" or "member A". The regional unconformities within the Sundance Formation, including the J5 unconformity at the base of the Windy Hill Sandstone, were described and named by Pipiringos and O'Sullivan (1978). Numerous publications have interpreted the depositional environment for the Windy Hill Sandstone, and have suggested that it is a tidal estuary (Kvale et al. 2001; McMullen et al. 2014), a prograding tidal delta (Zeiner 1974), a barrier coastline (Uhlir et al., 1988), and offshore sandbars (Brenner and Davies 1973, 1974b). The most recent study places the Windy Hill Sandstone in a sequence stratigraphic context, interpreting it as an incised valley fill deposited in the lowstand or transgressive systems tract (McMullen et al. 2014). Sand bodies deposited in the lowstand systems tract often serve as hydrocarbon reservoirs, so understanding the internal architecture and depositional processes of units like the Windy Hill Sandstone is important to assess porosity, permeability, and connectivity to updip or downdip deposits. Additionally, fluvial rocks of the terrestrial Morrison Formation that overlies the Windy Hill Sandstone are known for their Salt Wash uranium deposits in Utah and Colorado (Guilbert and Park 1986). These deposits, along with roll-front uranium deposits that are found in Wyoming, form in part because of accumulations of pyrite or reduced organic material in channel lags (Guilbert and Park 1986). Pyrite typically forms in marine conditions, and, since lags can form in tidal channels as well as in fluvial channels, understanding marginal marine and coastal plain deposits, such as the Windy Hill Sandstone and Morrison Formation, could prove valuable in exploration for these uranium resources. The vertical distributions of pyrite and organic material, both essential in creating the reducing conditions needed to for these uranium deposits to form, are stratigraphically controlled and are associated with surfaces that form with fluctuations in water depth. Because of this, placing nearshore and coastal deposits in a sequence stratigraphic framework is essential to understanding and predicting where in a system uranium deposits are likely to occur.

The purpose of this research is to place the Jurassic Windy Hill Sandstone in a sequence stratigraphic context and evaluate the conflicting interpretations of the depositional environment by creating, testing, and applying a workflow to use a quadcopter UAV to supplement the measurement of stratigraphic columns with minimal data gaps.

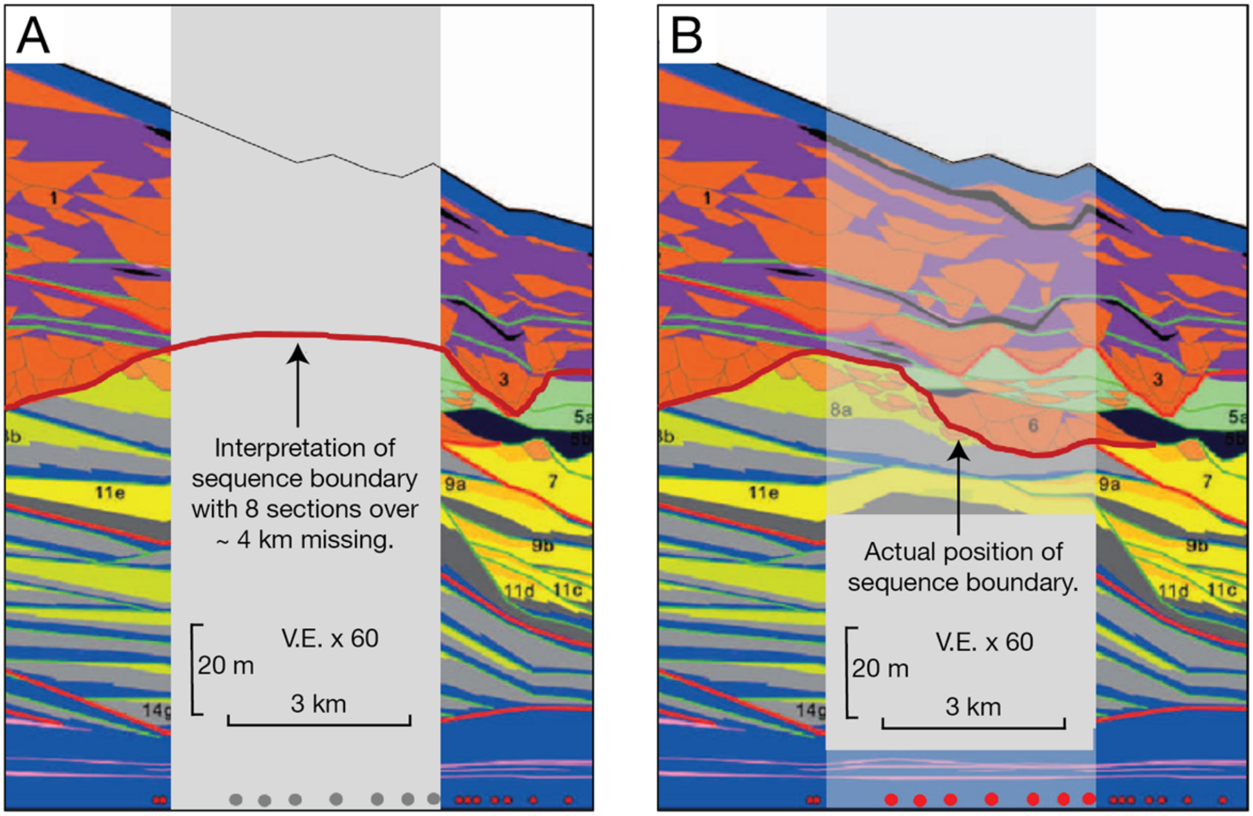

FIG. 1.1—Example illustrating the need for closely spaced sections. Figure shows a depositional dip-oriented cross-section from complex fluvial and incised valley fill deposits of the Cretaceous Notom delta. **A)** Incorrectly correlated sequence boundary caused by a data gap separating the left and right sides. Dots near the bottom of the cross-section represent measured columns, grey color indicates a hypothetical gap where section were not measured. **B)** Correct correlation of sequence boundary when the data gap is removed and additional columns are included. Modified from Zhu et al. (2012).

CHAPTER 2

UAV-BASED STRATIGRAPHIC COLUMN MEASUREMENT

Introduction

The growing availability of unmanned aerial vehicles, or UAVs, has led to the development of new methods for mapping and measuring features from digital data, such as 3D models and point clouds (Vasuki et al. 2014; Nieminski and Graham 2017; Chesley et al. 2017). A workflow to generate and rotate three-dimensional point clouds constructed from UAV imagery was developed for use in this study to fill in data gaps created by wide outcrop spacing and to measure columns that are topographically inaccessible. Similar methods have been proposed by Nieminski and Graham (2017), but they require the use of expensive commercial software to create models that are georeferenced in true three-dimensional space. The workflow presented in this study does not require a georeferenced model and is thus a cost-efficient option for UAV-based stratigraphy. The purpose of this workflow is to digitally measure multiple, closely spaced sections from a point cloud that is rotated to a stratigraphically horizontal position by transforming the axes so that z-coordinates represent stratigraphic position. Field tests of the workflow were conducted at an outcrop along a railroad cut near Hagan, Virginia to test the viability of the process and to confirm that the measurements are comparable to traditional field methods.

Workflow

The UAV workflow presented in this study consists of nine steps, beginning with UAV image collection and ending with the measurement of a lithologic column from the point cloud (Fig. 2.1). Each step uses the output from the previous step as the input. The steps in the workflow are described in detail below.

Outcrop imagery must first be collected by flying the UAV along parallel and overlapping transects in front of and over outcrops while taking nearly continuous photos. Additional photographs can be taken from the ground by carrying the UAV in front of outcrops where hazards exist or by using a hand-held digital camera. Photogrammetry software user guides suggest 60% photograph overlap as the optimal value and give more information regarding optimal flight paths based on the software and the nature of the object being modelled. In general, flying multiple transects over the same target while taking as many photographs as possible is a reliable way to ensure adequate data coverage. Multiple memory cards are required so that the storage of photographs is not a limiting factor.

An educational license of the Agisoft Photoscan was used as the photogrammetry software in this study, but other comparable structure-from-motion software, such as Pix4D, could also be used. The photographs from any one outcrop are easily aligned and three-dimensional point clouds are created using the workflow detailed in the Agisoft Photoscan user manual. Processing can be time intensive, but the resulting model has many benefits, including point clouds that can be edited to remove unwanted features such as vegetation. The educational license of this software is affordable compared with full licensing, but does not include the ability to use GPS ground control points or to georeference models with respect to a global reference frame. The correct orientation of a model is not necessary to use the workflow presented here, as dip, dip direction, and the digital rotational transformation of the point cloud are all measured and completed with respect to the local reference frame. This saves time in both data collection and image processing, but it also means that the digitally measured dip and dip direction do not correspond to actual field measurements of these values and cannot be compared between models of different outcrops. This means that, consistent with best practices for geological research, strike and dip measurements should be made in the field to better understand any regional structural trends.

If true orientation is desired, it can be most precisely completed by purchasing a license that allows for georeferencing or the use of ground control points. Alternatively, orientation can be completed visually without the use of ground control points by using the ‘rotate object’ tool in Agisoft Photoscan. This visual orientation method was used in the field test at the Hagan, Virginia outcrop to orient the model so that meaningful comparisons of actual and digitally measured strike and dip could be made to evaluate the viability of the method. Visual orientation was conducted by matching the orientation of the model to vertical Google Earth imagery. This was done multiple times and from several different perspectives (i.e. looking north, looking south, etc.) to improve the quality of the orientation. A highly visible, bright orange cross was also placed on the ground during image collection such that each 0.5 m arm of the cross pointed in a cardinal compass direction to assist with orientation. Objects in the model known to be horizontal, such as the railroad tracks at the Hagan test outcrop, were also used for orientation with respect to the tilt of the model. Measurements can also be made in the field during image collection to assist with the orientation step. Compass bearings of features such as roads or railroad tracks are essential in making an orientation as accurate as possible. Where features such this are absent, orientation will likely not be accurate and this step can be skipped, as a local reference frame is all that is needed to move forward with the method.

While it is not necessary for the model to be oriented with respect to a global reference frame, it is necessary for it to be scaled such that the measurements made are comparable to one another and to actual field measurements. If a professional license of photogrammetry software is purchased, then scaling is accomplished in conjunction with orientation using GPS ground control points. To keep research costs low, a different method was used in this study to scale the model without having to purchase an expensive software license. The point cloud was exported from Agisoft Photoscan as a .las file and opened in the free point-cloud viewer Quick Terrain Reader (by Applied Imagery; appliedimagery.com). The mensuration tool in Quick Terrain Reader was used to measure the distance, in native units, between two points in the model whose actual distance is known. An orange cross with a fifth vertical arm was used for this and was placed on the outcrop prior to image collection. Ideally, both the vertical and horizontal arms should be used to check the scaling of the model after the calibration process is complete. This was not always possible because of a misalignment of the vertical arm of the orange cross. This misalignment likely occurred because of insufficient photos and because the color of the vertical arm was the same color as the horizontal arms. In the point clouds, the vertical arm often appears flattened onto the horizontal plane because this is where the highest density of bright orange points was located in the model. Care should be taken to ensure sufficient photo coverage of the vertical arm and the scale calibration cross should be redesigned so that the vertical arm is a different, but equally contrasting, color. From the native and known measurements, a scaling factor is calculated by dividing the actual measurement by the native measurement. The scaling factor is applied to each axis of the model using the las2las tool of the LAStools suite. The potential error introduced by the scaling process is currently unknown, although comparisons of known measurements to the models indicate it that this error small enough to have a negligible effect on the overall stratigraphic interpretation. Future tests should be done to quantify and minimize this error, perhaps by using a larger distance for scale calibration. The next step of the workflow is to identify points in the model that lie on a single surface that was originally horizontal when the rocks were deposited, such as a bedding plane. This was done by exporting the point cloud as a .las file and opening it Quick Terrain Reader. In Quick Terrain Reader, the marker tool was used to obtain x-y-z coordinates of selected points, which were exported as a text file.

These points were used to construct a best-fit plane using a least-squares method, although other methods could also be applied (Fischler and Bolles 1981; Fernández 2005; Vasuki et al. 2014). The least-squares regression was completed by first converting the .las file into a text file using the las2txt tool in the LAStool suite and then by calculating the best-fit plane in R (see Appendix A for equations and code). Strike, dip, and dip-direction were calculated from this plane. If the model is not spatially aware with respect to a global reference frame, these measurements do not correspond to real-world measurement, but can still be used to rotate the axes so that bedding is in a stratigraphically horizontal position with respect to the locally defined z-axis. This rotation is the final step before the digital measurement of lithologic columns can be completed and is done in R by applying a series of matrix transformations (see Appendix C) to the points in the point cloud. After rotation, the z-value of each point corresponds to stratigraphic position and the x-y plane represents the earth's surface at the time of deposition.

The size of a point-cloud for any particular model may necessitate the splitting of the model into separate chunks that can be rotated individually and merged back together. This can be done in a number of different ways, including using the LAStool suite. After rotation, measurement of a column can be completed in Quick Terrain Reader by placing markers on points at bedset boundaries or other surfaces of interest. The z-values of these points correspond to stratigraphic position.

Field Tests

This method was tested on an exposure of the Silurian Clinch Formation near Hagan, Virginia, USA, in the Valley and Ridge Province. At this locality, strata dip between approximately 47° and 57° and are exposed along both sides of a railroad cut, allowing a three-dimensional view of the stratigraphy. A variety of experiments were performed to test (1) the fit of the calculated plane to data, (2) the most effective arrangements of points on a bedding plane, (3) the optimal number of points used on a bedding plane, (4) the viability of measuring strike and dip from a visually oriented model, and (5) the reliability of digital thickness measurements compared to field-based measurements. Estimates of uncertainty were also calculated where appropriate.

First, the fit of the plane to the points chosen from the point cloud was tested for seven beds, each with a different number of points picked on the bedding plane. In all cases, the R^2 of the fitted plane (i.e., the proportion of explained variance) is nearly 100% (Table 2.1). Such high R^2 values are not unexpected, given that the bed is exposed over meters laterally whereas the uncertainty in the bed top at any one point is on the order of a centimeter. As a result, points are unlikely to deviate substantially from a plane and the R^2 is correspondingly nearly 100%. In practice, R^2 should be used to check for cases in which points are clearly not from the same bed, for covered faults that offset a bed, or for subtle folding.

The effect of the spatial configuration of points picked on a bedding plane was also tested by using different combinations of points on one or both sides of the railroad cut and by varying how close points were to one another (i.e. wide vs. tight; Fig. 2.2). The best agreement to field measured strike and dip was predictably obtained when the fullest extent of the exposed bed was measured (both sides - wide and tight; Table 2.2), even with the small number of points used. Similarly, clustered and tight spacing of measured points produced the greatest difference from field values (clustered and one side – tight; Fig.

2.2) and should be avoided, as should picking points in a linear fashion, as this will result in an infinite number of solutions for the best fit plane (Fernández 2005).

A statistical resampling method, bootstrapping (Crowley 1992), was used to create a distribution of the mean dip estimate for each of seven beds at the Hagan outcrop. The number of points that were sampled was varied to determine the threshold after which the dip estimate did not substantially change. This occurs around 40 points (Fig. 2.3; Appendix A), and thus this is the minimum number of points that should be used to apply these methods. The bootstrapped distributions were also used to calculate 95% confidence intervals on the mean dip estimates (Fig. 2.3; Appendix A).

Bootstrapped dip estimates from the UAV-based point cloud model of the Hagan outcrop were compared to an average of field measurements taken for each bed (Table 2.3). All estimates of the dip were within 5 degrees of the averaged field measurements, which is within the uncertainty range of the field measurements themselves. Furthermore, the field measurements for Bed F have the largest deviation (5 degrees; Table 2.3) and were noted in the field as a low-quality measurement because it was uncertain whether it was taken on the bed or on a foreset if this measurement represented dip of the bedding plane or was actually reflecting dip of foresets within the bed. When this measurement is discarded, the average field dip is 53 degrees, decreasing the deviation from 5 degrees to 2 degrees. This underscores some of the sources of error in field-based measurements, especially when the terrain and difficult access to flat bedding planes at the Hagan outcrop is considered.

The point-cloud model of the Hagan, Virginia outcrop was rotated to a stratigraphically horizontal position based on the n = 40 bootstrapped dip estimate from Bed D. Bed D was chosen because it falls near the center of the range of dip estimates. Bed D is also interpreted as a storm bed in the offshore transition facies association rather than the tidal association. Beds in the tidal facies association that were sandy portions of heterolithic inclined strata rather than horizontal bedding planes were avoided for use in rotation of the point cloud for this reason.

A stratigraphic column was measured from the rotated point cloud, and these thicknesses were compared with previous measurements of the same exposure (Ginn 2014; Table 2.4; Fig. 2.4). These comparisons indicate strong agreement, with an overall cumulative difference in thickness of only 1% and a maximum cumulative difference of 7.3%. Of the individual intervals, all differ by less than 1 m and the average difference is 30 cm (Table 2.4). Given the difficulty in measuring the section with traditional Jacob staff techniques owing to the dip of the beds, their orientation relative to the railroad cut, as well as incomplete exposure and the difficulty of reaching areas of good exposure, it is likely that the Jacob-staff measurements have greater error than the point-cloud estimates. Further testing could quantify this. When the facies and environments of both columns are compared side by side the depositional patterns and surfaces appear at approximately the same stratigraphic elevations (Fig. 2.4).

The good agreement of the thickness measurements from the point cloud with the field measurements from Ginn (2014) illustrates the general viability of this workflow, but an estimate of uncertainty in these measurements is also useful. The bootstrapped distribution of the dip estimate of Bed D was used to calculate a 95% confidence interval on that estimate. This range in dip from 49.2° to 50.1° can be used to calculate a margin of error on the stratigraphic column measurement. The total thickness of strata measured from the UAV point-cloud model at the Hagan outcrop was 51.32 m. If this measurement is adjusted to account for the 95% confidence interval of the dip estimate, then an upper and lower estimate of total thickness can be calculated, giving a range of 51.21–52.17 m.

These calculations are all performed with the assumption that the bedding in the outcrop is dipping uniformly and does not change systematically along the column. This assumption is commonly made in the field, but may not always be an accurate representation of bedding behavior. The Hagan outcrop is an excellent example of this, where an approximately 10° range in dip is observed in field measurements and in the bootstrapped dip estimates from the point cloud (Fig. 2.5). Variation in dip is an additional source of uncertainty in stratigraphic column measurement regardless of the technique used. These uncertainties can also be estimated based on the high and low values in the range of bootstrapped dip estimates. The dip estimated from the point cloud varies from 46° (Bed H) to 57° (Bed A), and if the lower and upper confidence intervals are considered, then the thickness could be off by as much as 9.37 m, a difference of 20%. This indicates that care should be taken when measuring section to correct for dip that changes systematically. In the field this can be done be re-measuring strike and dip at regular intervals. When using UAV-based methods, different segments of the models could in principle be easily rotated by different amounts to account for variation in the strike and dip, and uncertainty in the measurements can be calculated and considered during interpretation.

The demonstrated success of this workflow at the Hagan outcrop indicates that it is a reliable and effective method to measure lithologic columns and can serve as a valuable tool to decrease the data gap between columns in larger scale sequence stratigraphic studies. It is beneficial to orient the axes of the point cloud so that bedding is in an originally horizontal position for easy and repeatable column measurement that outweighs the cost of processing time. This is similar in principle to multiplying the apparent thickness of a column by the cosine of the dip angle, but with the added advantage that the points used for measurement can exist anywhere on the given bedding plane within the point cloud and do not have to possess the same x- and y- coordinates. Additionally, the workflow presented here allows for a calculation of uncertainty in dip angles and column measurement that is unattainable from field data and provides a lasting outcrop model that can be re-visited as necessary.

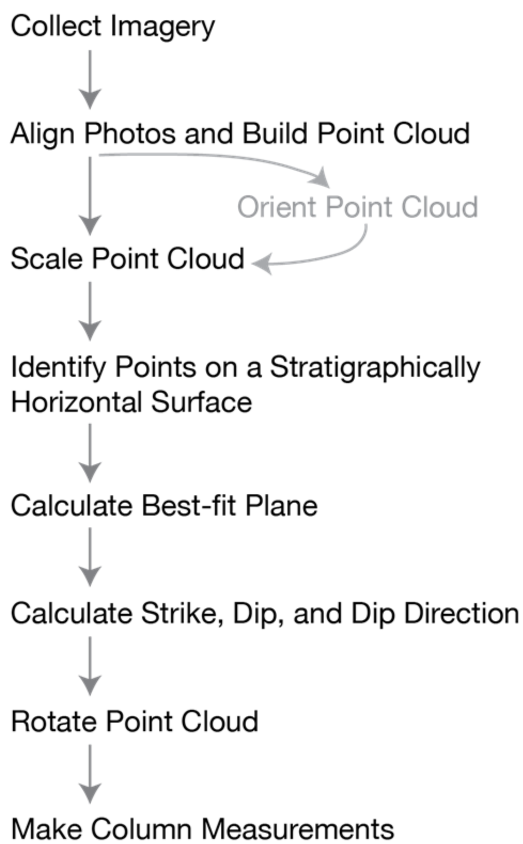

FIG. 2.1—Basic workflow for UAV-based stratigraphic column measurement.

TABLE 2.1—Test for fit of plane to points on multiple beds at the Hagan, Virginia outcrop.

Bed	n	R^2 of fitted plane
A	32	0.997
B	15	0.999
D	12	1.000
E	10	0.996
F	15	0.999
H	7	0.999
I	10	1.000

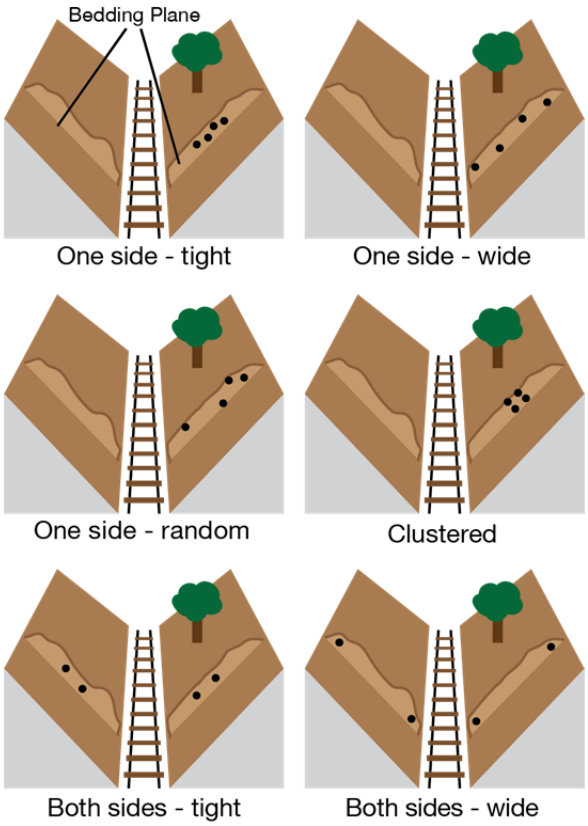

FIG. 2.2—Spatial configurations of points tested. In all cases care was taken to avoid co-linear points to the greatest extent possible. Configurations such as one side - tight and one side - wide appear co-linear because the configuration was limited by the extent of the bedding plane but are not truly co-linear at the outcrop scale.

TABLE 2.2—Test for spatial arrangement of points used for dip estimate. All arrangements were tested on Bed A with n=4. The average field measurement for strike and dip of Bed A taken with a Brunton transit is 263° / 55°, with a range in strike of 256°–276° and a range in dip of 51°–59° for seven measurements.

Point Geometry	R^2 of fitted plane	UAV estimate of strike / dip	Deviation from field measurement
Clustered	0.996	259° / 58°	-4° / +3°
One side - tight	0.999	230° / 70°	-33° / +15°
One side - wide	0.999	261° / 57°	-2° / +2°
One side - random	1.000	265° / 59°	+2° / +4°
Both sides - tight	1.000	264° / 57°	+1° / +2°
Both sides - wide	1.000	265° / 55°	+2° / 0°

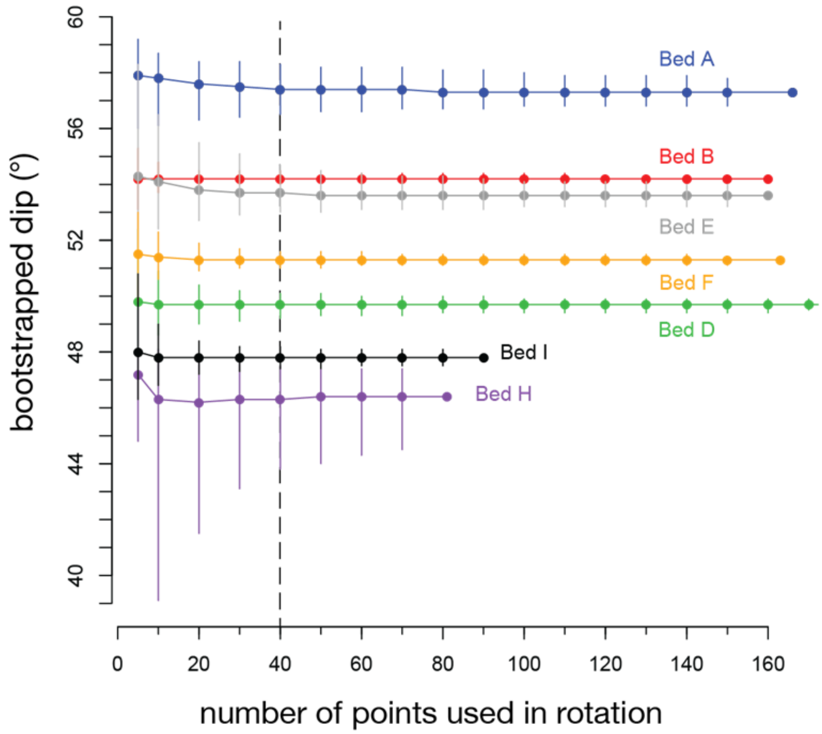

FIG. 2.3—Plot of bootstrapped dip estimates at the Hagan, Virginia outcrop. Plot shows dip estimates for all beds with a varied sample size and 95% confidence intervals. Dashed line at n=40 indicates the threshold after which estimate is not improved by the further addition of points. Plots for individual beds can be found in Appendix A.

TABLE 2.3—Comparison of UAV dip estimates to field measurements. UAV dip estimates were bootstrapped with n=40. Field measurements were taken with a Brunton transit compass and averaged for each bed.

Bed	UAV dip estimate	95% confidence interval	Field measurements of dip average, dip range, sample size	Deviation from field measurement
A	57°	56.5–58.3°	55°, 51°–59°, n=7	+2°
B	54°	54.0–54.5°	55°, 53°–58°, n=5	-1°
D	50°	49.2–50.1°	51°, 49°–52°, n=3	-1°
E	54°	53.0–54.7°	58°, 56°–61°, n=4	-4°
F	51°	51.0–51.6°	56°, 52°–63°, n=3	-5°
H	46°	43.8–47.5°	48°, 44°–50°, n=5	-2°
I	48°	47.4–48.2°	48°, 44°–50°, n=5	0°

TABLE 2.4—Comparison of stratigraphic thickness measurements derived from traditional Jacob's staff methods and UAV-based methods.

	Thickness based on Jacob's staff (m)	Thickness based on UAV methods (m)	Difference (m)
Tidal flat 3	5.0	4.8	0.2
Tidal channel 2	1.7	1.5	0.2
Tidal flat 2	7.6	6.8	0.8
Tidal channel 1	1.7	2.3	0.6
Tidal flat 1	1.9	2.3	0.4
Shoreface	2.1	2.4	0.3
Offshore transition 3	1.8	1.5	0.3
Offshore 3	2.2	2.1	0.1
Offshore transition 2	1.9	2.2	0.3
Offshore 2	3.1	2.9	0.2
Offshore transition 1	5.6	6.0	0.4
Offshore 1	16.2	16.7	0.5
Total	50.8	51.3	0.5

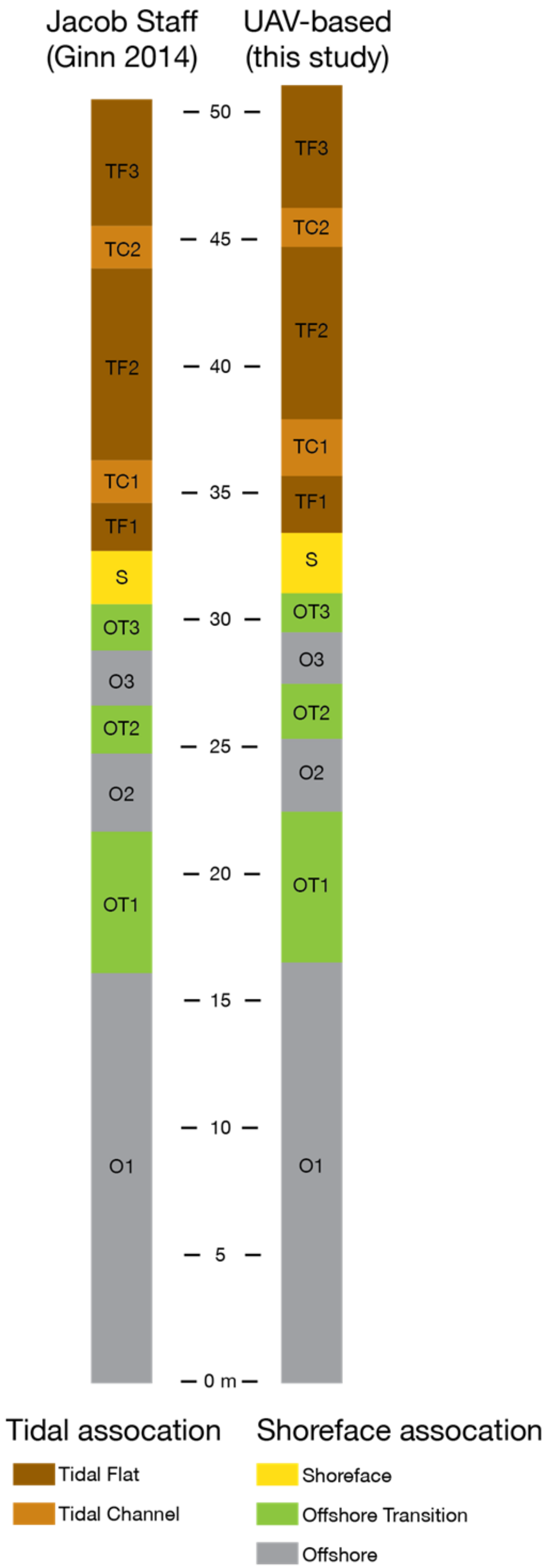

FIG. 2.4—Comparison of interval thicknesses from UAV-based column and field-based column. Facies associations after Ginn 2014.

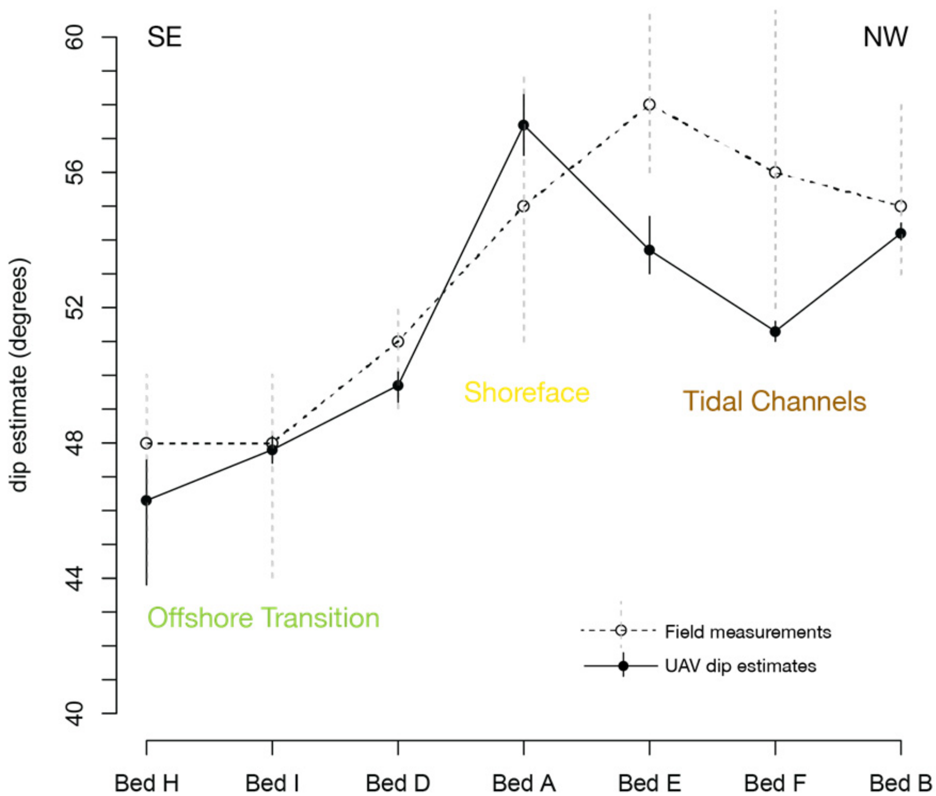

FIG. 2.5—Dip variation at the Hagan, Virginia outcrop. UAV dip was estimated by bootstrapping with n=40 and 95% confidence intervals are shown as solid vertical lines. The field measurements are averages for each bed measured with a Brunton transit and the range of measurements is shown as dashed vertical lines. Beds are arranged from stratigraphically lowest (H) to highest (B).

CHAPTER 3

THE FALLING STAGE PROGRADATION OF AN OPEN-COAST TIDAL FLAT: THE JURASSIC SUNDANCE-MORRISON TRANSITION OF WYOMING, U.S.A.[1]

[1] Wright, S.W. and S.M. Holland. To be submitted to *Journal of Sedimentary Research.*

Abstract

The Upper Jurassic Windy Hill Sandstone of Wyoming exhibits many of the criteria consistent with deposition on an open-coast tidal flat. Open-coast tidal flats have been described from sedimentological studies along the modern Korean coast, and represent an intermediate environment between wave-dominated shorefaces and tidal flats. The Windy Hill Sandstone allows this mixed energy environment to be placed in a sequence stratigraphic context. Multiple surfaces of forced regression are present in the Windy Hill Sandstone and underlying Redwater Shale, placing these units in the falling-stage and lowstand systems tracts and re-enforcing the idea that tidal deposits can occur in a wide variety of sequence stratigraphic contexts. The identification of multiple surfaces of forced regression at stratigraphic positions previously interpreted as the J5 unconformity calls for a re-evaluation of the placement of this surface, placing it higher in the section than previously thought. This interpretation implies that the Redwater Shale, Windy Hill Sandstone, and overlying Morrison Formation are partly contemporaneous within Wyoming. The Morrison Formation displays continuous but episodic progradation in the study area, and is an example of a case where the accommodation succession method of sequence stratigraphy is useful, allowing deviations from standard sequence stratigraphic models to be recognized and the causes of the deviations, such as regional tectonic variation, to be inferred.

Introduction

Tidal deposits in the rock record have been observed in a wide variety of environments and sequence stratigraphic contexts. They are found in overall regressive contexts (Willis and Gabel 2001, 2003; Lee et al. 2007; Desjardins et al. 2012; Willis and Fitris 2012; Legler et al. 2014; Ainsworth et al. 2015; Burton et al. 2016) and are commonly described in the lowstand or transgressive systems tracts (Shanley and McCabe 1991; Van Wagoner 1991; Dalrymple et al. 1992; Mellere 1994; Cattaneo and Steel 2003; Plint and Wadsworth 2003; Li and Bhattacharya 2013; Chentnik et al. 2015; Jordan et al. 2016). Tides have been shown to be a primary mode of deposition on modern open coasts even where wave energy also prevails (Alexander et al. 1991; Yang et al. 2005), calling into question the commonly reported association of tidal deposits with protected estuaries or deltas at discrete ends of the coastal environment spectrum (Boyd et al. 1992). The existence of modern open-coast tidal flats implies that this is also a possibility for the past, both in terms of depositional environment and position in a sequence stratigraphic framework. Along the western Korean coast, tidal deposits formed during the last Pleistocene highstand and were subaerially exposed during the sea-level lowstand (Park et al. 1998; Lim and Park 2003). Subsequent transgression of these is overlain by a second set of highstand tidal flat deposits (Lim and Park 2003). This entire succession is tide-dominated, underscoring that tidally dominated facies are not limited to the transgressive systems tract. The commonly reported association of tidal deposits with the transgressive systems tract could in some cases be misleading if the deposits were inferred to be estuarine based on an abundance of tidal features. The sequence stratigraphic context of tidal deposits is important because tide-dominated deposits in lowstand incised valleys have been shown to host a disproportional number of hydrocarbon reserves (Van Wagoner et al. 1990), so understanding the internal architecture and depositional processes behind units like the Windy Hill Sandstone is important for developing depositional models, as well as for assessing variations in porosity, permeability, and lateral connectivity.

The Upper Jurassic Windy Hill Sandstone is a tidal unit that sits in an overall regressive position between the offshore Redwater Shale and the terrestrial Morrison Formation. The Windy Hill Sandstone typically has an erosional base (Imlay 1956; Pipiringos 1968; Uhlir et al. 1988; McMullen et al. 2014), and this contact between the Windy Hill Sandstone and the underlying Redwater Shale has been previously identified as a subaerial unconformity (Pipiringos and O'Sullivan 1978; McMullen et al. 2014). Multiple interpretations exist for the depositional environment of the Windy Hill Sandstone and its abundant tidal features, but most are unsatisfactory when modern analogues are considered. This study aims to address this issue by using closely spaced sections to place the Windy Hill Sandstone in a sequence stratigraphic context, keeping in mind the criteria for recognizing stratigraphic surfaces and recent work regarding modern tidal depositional systems and their sequence stratigraphic settings. The depositional origin and sequence stratigraphic framework of the Windy Hill Sandstone has implications for regional correlation and interpretations of relative sea level and paleogeography, as well as for the occurrence of ancient open-coast tidal flats where both shoreface and tidal flat deposits, previous thought of as distinct environments, co-exist.

Geologic Setting and Previous Research

Stratigraphic Context and Age

The Windy Hill Sandstone is a resistant unit that is exposed in Wyoming and southern Montana, and it separates underlying marine mudstones of the Redwater Shale from the overlying coastal plain deposits of the Late Jurassic Morrison Formation (Imlay 1956; Pipiringos 1968). The Windy Hill Sandstone is the uppermost member of the Jurassic Sundance Formation, and it is separated from the rest of the formation by a regional unconformity (Fig. 3.1; Pipiringos 1968; Uhlir et al. 1988; McMullen 2014). Ammonite biostratigraphy and radiometric dating of bentonites places deposition of the Redwater Shale in the early Oxfordian, with the Windy Hill Sandstone being middle to late Oxfordian (Pipiringos and O'Sullivan 1978; Callomon 1984; Imlay 1982; Kvale et al. 2001). Deposition of the coastal plain Morrison Formation, radiometrically dated using ash beds, began in the latest Oxfordian to the earliest Kimmeridgian and persisted until the Tithonian (Kowallis et al. 1998).

Paleogeography and Tectonic Setting

The Redwater Shale and Windy Hill Sandstone were deposited in the elongate, epicontinental Sundance Seaway in western North America that is somewhat comparable to the modern Yellow Sea. This seaway sat in a retro-arc foreland basin (Bjerrum and Dorsey 1995) and had a connection to the Pacific Ocean at the northern end of British Columbia (Fig. 3.2; Blakey 2014; McMullen et al. 2014). The Sundance Seaway was bordered to the west by a fold and thrust belt with the Cordilleran volcanic arc beyond, and it was bounded to the east by the North American craton (Imlay 1956; Brenner and Peterson 1994; Lawton 1994; Bjerrum and Dorsey 1995). Middle Jurassic thrust faulting created a retroarc foredeep in the western portion of the Sundance Seaway, and the Redwater Shale and Windy Hill Sandstone were deposited on the northwest-facing ramp that developed to the east of the foredeep

(Bjerrum and Dorsey 1995; McMullen et al. 2014; Clement and Holland 2016). Also forming in the Middle Jurassic, the northeast-southwest trending Sheridan Arch is a pre-Laramide structural high in south-central Wyoming (Fig 3.2) that is thought to have influenced Sundance deposition and is responsible for the thinning and truncation of lower Sundance deposits as they onlap onto it in the Bighorn Basin (Pipiringos and O'Sullivan 1978; Schmude 2000; Kvale et al. 2001; McMullen et al. 2014). Paleogeographic reconstructions place Wyoming at either 22°–33°N (Kocurek and Dott 1983) or at 35°N–40°N (Blakey 2014) during the Middle and Late Jurassic, suggesting an arid to semi-arid climate (Kocurek and Dott 1983; Kvale et al. 2001; Blakey 2014). Northern drift of the continent, however, may have moved the region into a wetter climatic zone by the Late Jurassic (Imlay 1980; Kocurek and Dott 1983; Parrish and Peterson 1988; Johnson 1992). The geometry of the Sundance Seaway suggests that tidal influence may have been amplified because of the narrow width, but long reach (2000 km) of the seaway, although shallow water depths may have inhibited tidal exchange. Prevailing winds have been interpreted as towards the west (Fig. 3.2; Parrish and Peterson 1988).

Previous Interpretations

Previous studies on the upper Sundance Formation and lower Morrison Formation agree that the Redwater Shale represents deposition in the offshore-transition zone of a wave-dominated shelf and that the lower Morrison Formation represents a coastal plain environment (Mirsky 1962; Imlay 1980; Uhlir et al. 1988; Johnson 1992; McMullen et al. 2014). The Windy Hill Sandstone sits in a regressive position between these two units and tidal features are commonly reported within it (Imlay 1980; Uhlir et al. 1988; Kvale and Vondra 1985; Johnson 1992; Ufnar 1994; McMullen et al. 2014). Even so, the depositional environment of the Windy Hill Sandstone has been variously interpreted as a tidal estuary (Kvale and Vondra 1985; McMullen et al. 2014), a prograding tidal delta (Zeiner 1974), a barrier coastline (Uhlir et al. 1988), and offshore sandbars (Brenner and Davies 1973, 1974b).

While each of these interpretations may be consistent with observations at some localities, none reconcile the observed geographic variation in the unit over its outcrop area. For example, the geographic extent of the Windy Hill Sandstone (~ 70,000 km^2) is much larger than even the largest of modern tidal estuaries. Similarly, the Windy Hill Sandstone, exposed as long continuous ridges of resistant sandstone, is more consistent with a shoreface (Fig. 3.3). The interpretation of the Windy Hill Sandstone as a tidal estuary has been previously considered and dismissed based on the observed lateral extensiveness of the sandstone and shelly lags within it (Uhlir et al. 1988). For the tidal estuary interpretation to be valid, an exceptionally large amount of lateral migration is required to achieve the observed tabular geometry (Uhlir et al. 1988).

The interpretation of the Windy Hill Sandstone as a barrier coastline was proposed as an alternative to the tidal estuary interpretation (Uhlir et al. 1988), but it also requires extensive lateral migration to explain the tabular geometry and laterally extensive nature of the Windy Hill Sandstone. There are no observed clinoforms in the Windy Hill Sandstone (Fig. 3.3C; Uhlir et al. 1988; Johnson 1992; Ufnar 1994; McMullen et al. 2014), which is inconsistent with the interpretation of deltaic deposition. The sharp basal contact of the Windy Hill Sandstone with the underlying Redwater Shale is also difficult to explain through delta progradation, as conformable contacts would be expected.

Offshore sandbars have also been cited as the depositional environment for the Windy Hill Sandstone (Brenner and Davies 1973, 1974b). Although offshore bars were once described from many settings, most of these have been re-interpreted, commonly as detached shoreface deposits formed during the falling-stage systems tract (Bergman and Walker 1999; Plint 2010; Fielding et al. 2014; Hutsky and Fielding 2016). As such, it is possible that the Windy Hill Sandstone represents detached falling-stage shorefaces rather than offshore bars.

These contradictions and problems with existing interpretations of the Windy Hill Sandstone as a tidal estuary, a barrier coastline, a prograding tidal delta and offshore bars indicate the need for renewed study with an emphasis on modern analogues and a consideration of the spatial scale of modern depositional environments.

Coupled with this is disagreement on the nature and existence of an unconformity between the Redwater Shale and Windy Hill Sandstone. A regional unconformity, called the J5, at this contact has been variously described as a flat peneplain surface (Pipiringos and O'Sullivan 1978; Johnson 1992) with no evidence of channels, to one displaying meters of relief and truncating beds of the Redwater Shale (McMullen et al. 2014). Others have described physical evidence of this unconformity as weak, especially in the Bighorn Basin, (Johnson 1992), and others hesitate to place an unconformity at this stratigraphic level (Imlay 1980; Uhlir et al. 1988; Johnson 1992). In these cases, any observed erosion or sharp contact between the Redwater Shale and Windy Hill Sandstone has been attributed to the migration of tidal channels or inlets (Uhlir et al. 1988). The contact between the Windy Hill Sandstone and overlying Morrison Formation has been described as gradational and laterally inter-fingering (Pipiringos 1968; Pipiringos and O'Sullivan 1978; Uhlir et al. 1988; Johnson 1992; McMullen et al. 2014), suggesting that the Morrison records conformable progradation of a coastal plain over the deposits of the Windy Hill Sandstone. Because of this, the Windy Hill is regarded by some as the basal member of the Morrison Formation (Johnson 1992; Peterson 1994).

Field and UAV-Based Methods

Nine exposures of the Windy Hill Sandstone across Wyoming and southern Montana (Fig. 3.4A, 3.4B) were studied to characterize its facies, geometry, and contacts with surrounding units. At each locality, lithology, bedding, sedimentary structures, trace fossils, and body fossils were described. Thirty-five hand samples were collected and twenty-seven thin sections were prepared to assist in lithologic descriptions (Appendix B). These characteristics were used to outline facies, build a depositional model, and identify stratigraphic surfaces and depositional sequences. Lithologic columns (Appendix C) were measured using traditional Jacob staff methods as well as UAV-based methods.

Sixteen closely spaced (~1 km apart) columns were measured along the eastern flank of Sheep Mountain in the Bighorn Basin (Fig. 3.4C). Closely spaced sections were used to ensure that surfaces could be correctly correlated, and contacts were walked out in the field where possible. A DJI Phantom 3 Advanced quadcopter UAV with 1080p-video capability and a 12-megapixel camera was also used to trace bedding and contacts between these columns. The sixteen columns at the Sheep Mountain exposure form an approximately 11 km northwest to southeast transect (Fig. 3.4C, B-B') that is roughly parallel to depositional dip (Fig. 3.2; Blakey 2014; McMullen et al. 2014). A second, approximately dip-oriented cross-section was constructed with eight columns over 420 km to characterize regional variation (Fig. 3.4B, A-A'). At the Red Gulch locality (Fig. 3.4B, C-C'), eleven short columns were logged over a distance of 1.1 km to characterize the incision observed there. Traditionally measured columns at Red Gulch were tied into a UAV point-cloud model to supplement field data.

A quadcopter UAV was used to collect aerial imagery at twelve exposures by flying a series of parallel and overlapping transects in front of and over outcrops. This imagery was processed using the photogrammetry software Agisoft Photoscan to produce structure-from-motion 3D point-cloud models, which were used to examine facies relationships, trace contacts, measure incision, and to measure columns that were not accessible. Eleven stratigraphic columns were measured from the point clouds after they were rotated to a stratigraphically horizontal position. Rotation was completed by first picking points on bedding planes in Quick Terrain Reader and using least squares to fit a plane to these points (Appendix A). Strike and dip were calculated from the plane and used to rotate the entire point cloud via a series of matrix transformations, which restored bedding to a stratigraphically horizontal attitude (Appendix A). After this rotation, the z-coordinate of every point in the point cloud is equivalent to stratigraphic position, making digital lithological column measurement possible. The use of point clouds allows additional stratigraphy to be documented, lateral heterogeneity to be characterized, and the distances between lithologic columns to be decreased.

Facies Analysis

Fourteen facies are described from the upper Redwater Shale, the Windy Hill Sandstone, and the basal Morrison Formation. Facies are based on distinctive combinations of lithology, bedding, sedimentary structures, and trace fossils, as well as stratigraphic relationships with other facies. These facies are grouped into four facies associations. The wave-dominated shelf facies association (Table 3.1) is present in the Redwater Shale, the shoreface facies association (Table 3.2) and the tidal-coast facies association (Table 3.3) make up the Windy Hill Sandstone, and the alluvial plain facies association (Table 3.4) comprises the basal Morrison Formation.

Wave-dominated Shelf Facies Association

Description.—The wave-dominated shelf facies association consists of a single facies, mudstone (facies M) with sparse, thin interbeds of fine sand (Fig. 3.5). Facies M (Table 3.1) is laterally continuous and geographically widespread. Isolated occurrences of laterally discontinuous rippled sand beds (facies Sr-s) encased by facies M indicates a close genetic association of the two facies (Fig. 3.5A). Marine body fossils are common and include the belemnite *Pachyteuthis*. Trace fossils are consistent with the *Cruziana* ichnofacies (Table 3.1). Facies M coarsens upwards at some localities but generally forms thick units with little vertical or lateral variation.

Interpretation.—The dominance of mud in this facies association indicates an environment with low shear stress which allowed fine-grained sediment to settle from suspension. The presence of marine body fossils and components of the *Cruziana* ichnofacies also indicate a low-energy, low-stress, marine depositional environment (Buatois and Mángano 2011). This, along with the widespread nature of the facies association, is consistent with deposition in the offshore to offshore transition zones of a wave-dominated shelf (Clifton 2006; Plint 2010). Within this facies association, Facies M is interpreted to represent deposition below fairweather wave base (Brenner and Davies 1974a; Wright 1971), making it the deepest-water facies observed in the study area. The isolated sand interbeds are interpreted as distal storm deposition (Brenner and Davies 1973, 1974b; Specht and Brenner 1979; McMullen et al. 2014). Other typical features of storm deposition, such as hummocky cross-stratification, were rarely observed and have not been reported in previous studies on the Redwater Shale (McMullen et al. 2014). This is attributed to a lack of the specific conditions required to form hummocky cross-stratification, such as a moderately strong long-period oscillatory current with a superimposed weak unidirectional current (Dumas et al. 2005; Plint 2010). Given the limited fetch to the west, waves in the Sundance Seaway were likely not strong enough to provide such conditions, and hummocky cross-stratification did not form.

Shoreface Facies Association

Description.—Units of the shoreface facies association are exposed as laterally continuous ridges composed of shell beds and gravels, along with rippled fine sandstone that coarsens upwards into large-scale cross-stratified sandstone (Table 3.2). Some packages consist only of rippled sandstone (facies Sr-s) and cross-stratified sandstone (facies Sd-le), occasionally directly overlying the wave-dominated shelf facies association. Small (~2 cm) sand intraclasts and mud rip-ups are locally observed in facies Sd-le. Facies Sr-s also occurs as thin interbeds encased within facies M of the wave-dominated shelf association, with beds typically becoming thicker and more frequent at higher stratigraphic positions.

Other packages of the shoreface facies association include combinations of cross-stratified and tabular shell gravels (facies Gsd and Gst), some composed entirely of the scallop *Camptonectes* (facies Gc). These shelly gravels are much coarser grained than any other facies in the shoreface or wave-dominated shelf facies associations, and all shelly gravel facies have sharp basal contacts and some degree of bed amalgamation (Table 3.2). Facies Gsd and facies Gst typically occur in close stratigraphic association, with facies Gsd overlying facies Gst. Facies Gsd is often also associated with facies Sd-le, with the facies locally interfingering and grading laterally into one another as shell content varies. Occurrences of Facies Gc show no close vertical relationship to any other facies of the shoreface facies association and are instead encased within the offshore mudstone of the wave-dominated shelf facies association. Both the upper and lower contacts of Facies Gc are sharp. The vertical occurrences of facies Gsd, facies Gst, and facies Gc are associated with flooding surfaces or surfaces of forced regression.

Interpretation.—The rippled fine sandstone bedsets of facies Sr-s are interpreted as a more proximal equivalent to the thin isolated sandstone beds observed in the wave-dominated shelf facies association, and they represent deposition above fairweather wave base in the lower shoreface (Clifton 2006; Plint 2010). The upward increase in the number and thickness of beds of facies Sr-s indicates progressive shallowing upwards. The large-scale cross-stratification in facies Sd-le is interpreted to represent the migration of dunes in the upper shoreface, so the coarsening upwards of facies Sr-s into facies Sd-le again supports an overall regressive trend (Clifton 2006; Plint 2010).

The shelly gravels of facies Gsd, facies Gst, and facies Gc, however, do not fit this trend. These shell gravel facies occur in two contexts, one in which the gravels disconfomably overly facies M of the wave-dominated shelf facies association, and one in which the gravels sharply overly facies of the tidal flat facies association. In both cases the gravels generally fine upwards into facies Sr-s and facies Sd-le. These basal contacts of the shell gravels are interpreted as flooding surfaces or surfaces of forced regressions formed by changes in water depth. These facies, although associated with surfaces more than distinct environments, are assigned to the shoreface facies association based on the presence of marine fossils, the association with facies Sd-le and facies Sr-s, and the vertical position in the column between offshore and coastal plain deposits.

Facies Gc is unique in that it appears to be related to the wave-dominated shelf facies association rather than the other shoreface deposits. However, the coarse-grained nature of the beds and the abundant fragments of the scallop *Camptonectes,* shown to have been a shallow water, attached suspension feeder (Wright 1971; Wright 1974; Brenner and Davies 1974b), indicate an environment with higher shear stress than expected for the offshore. Individual beds of facies Gc are therefore interpreted as proximal event beds similar to facies Sr-s, forming in a lower shoreface environment (Clifton 2006; Plint 2010). Previous work on the Redwater Shale and on similar accumulation of *Camptonectes* in other deposits also invoke storms as the depositional process and place the shell beds in the lower shoreface (Brenner and Davies 1973; Fürsich and Heinberge 1983; McMullen et al. 2014). The exceptionally low diversity of the shell fragments observed in facies Gc is attributed to the particular conditions of the Sundance Seaway, such as a single northern opening and strong environmental gradients (Danise and Holland 2017). The high degree of amalgamation observed in Facies Gc, along with the sharp contacts of facies Gc with the underlying wave-dominated shelf association, suggests that this facies forms from sudden shallowing at surfaces of forced regression. The amalgamation and concentrations of shell fragments form from stratigraphic condensation accompanying slower rates of deposition (Kidwell 1991).

Facies Gsd and facies Gst also display evidence of sediment starvation in the shoreface (Kidwell 1991) and are interpreted as sharp-based shorefaces bounded below by surfaces of forced regression when they directly overlie facies M and display sudden shallowing from the wave-dominated shelf facies association into the shoreface facies association (Posamentier and Allen 1999; Catuneanu 2006). More commonly, however, facies Gsd and Gst are associated with a sudden deepening into the shoreface facies association from the tidal flat facies association and are interpreted to represent stratigraphic condensation and small transgressive lags at minor flooding surfaces (Van Wagoner et al. 1990; Kidwell 1991; Catuneanu 2006).

Tidal Flat Facies Association

Description.—Deposits of this facies association comprise thick bedsets of channelized large-scale cross-stratified sandstone that fines upwards into rippled, planar laminated, and massive sandstone. Complete fining-upward successions of this facies association include facies Gtl, facies Sd-ch, facies Sr-t, facies Sm-t, and facies Sp-t (Table 3.3), but it is also common for facies Sr-t, facies Sm-t, and facies Sp-t to fine upwards from units of the shoreface facies association (Fig. 3.6). Facies Sr-t, facies Sm-t, and facies Sp-t all co-exist within single bedsets and exhibit a close stratigraphic association (Fig. 3.7F). Facies Gtl is the coarsest facies observed in the tidal flat facies association, and it contains sand intraclasts, mud rip-ups, wood, and chert (Fig. 3.8). Facies Gtl and facies Sd-ch often occur in stratigraphic association with one another and can exhibit channel-scale erosion into underlying units (Fig. 3.8F). Trace fossils in the tidal flat facies association comprise the *Cruziana* and *Skolithos* ichnofacies (Fig. 3.9; Seilacher 2007; MacEachern et al 2010; Buatois and Mángano 2011).

Interpretation.— The presence of herringbone cross-stratification (Fig. 3.7A), current ripples with bimodal paleocurrents (Fig. 3.7B), sigmoidal cross-stratification (Fig. 3.10A), and compound dunes (Fig. 3.10B) in this facies association indicate tidal influence (de Raaf and Boersma 1971; Dalrymple 2010). These features are common in the study area and have been reported by many researchers (Imlay 1956; Pipiringos 1968; Uhlir et al. 1988; Ufnar 1994; McMullen et al. 2014). Previously collected data indicate bimodal to polymodal paleocurrent orientations with reactivation surfaces, tidal bundling, and mud drapes (Uhlir et al. 1988; Ufnar 1994), further supporting a tidal interpretation (de Raaf and Boersma 1971). Paleocurrent data indicate primarily northwest to southeast tidal currents (Fig. 2.7B; Uhlir et al.

1988) with a lesser east-west component that has been attributed to tidal channel migration (Uhlir et al. 1988).

The abundance of tidal sedimentary structures, fine grain size, and close stratigraphic association within single bedsets indicate that facies Sr-t, facies Sm-t, and facies Sp-t were deposited in a sandy tidal flat (Yang et al. 2005; Dalrymple 2010). The trace fossil associations further support this, as *Skolithos* has been shown to grade landwards into *Cruziana* on tidal coasts (Buatois and Mángano 2011). Pterosaur tracks are also observed in facies Sr-t (Fig. 3.9F), indicating shallow water depths with intermittent exposure (Logue 1977; Lockley and Wright 2003; Connely 2006), consistent with periods of low tide on a tidal flat. Within the tidal flat facies association, facies Sd-ch is interpreted to represent small tidal channels based on its channelized geometry, tidal sedimentary features, and large-scale cross-stratification (Fig. 3.8; 3.10; Dalrymple 2010). Facies Gtl is interpreted to represent lag deposits in tidal channels based on its grain size, its association with erosional surfaces, and its association with facies Sd-ch (Fig. 3.8; Dalrymple 2010). The fining-upward successions from facies Gtl to facies Sd-ch to facies Sr-t, facies Sm-t, and facies Sp-t (Fig. 3.6) is consistent with tidal flat progradation and tidal channel migration (Alexander et al. 1991; Dalrymple 2010).

Alluvial Plain Facies Association

Description.—The alluvial plain facies association is dominated by fine-grained sediments that are commonly poorly exposed in the study area. Where well exposed, successions consist of variegated muddy and silty deposits of facies Slt (Table 3.4; Fig. 3.11A) with thin beds of fine sand that comprise facies Sr-a, facies Sm-a, and facies Sp-a (Table 3.4; Fig. 3.11B). These intervals are usually truncated by a large-scale trough cross-bedded sandstone of facies Sd-a (Table 3.4; Fig. 3.11D). Wood and dinosaur bone fragments are locally observed at the base of the sandstone, and no marine body or trace fossils are present. Facies Sp-a is often associated with facies Sd-a. Facies Sr-a contains current ripples with no indication of tidal influence. Facies within the alluvial plain facies association are observed to coarsen upwards from mud-dominated intervals to cross-stratified sandstones.

Interpretation.—The truncation of variegated mudstones by sandstones in this facies association, along with the lack of marine body or trace fossils, and the lack of tidal structures indicate deposition in a near-shore fluvial environment. The variety of colors observed in facies Slt (Fig. 3.11; Moberly 1960; Mirsky 1962; Imlay 1980; Kvale and Vondra 1985; Johnson 1992) reflect the carbon content and iron oxidation state of the deposits, with green and red siltstones and shales like those observed in facies Stl having less carbon than dark colored or black marine shales more similar to facies M of the wave-dominated shelf facies association (Maynard 1982). Oxidation state plays an important role in color, with red being related to an oxic environment and green being related to a post-oxic environment (Maynard 1982; Berner 1981), both of which are consistent with fluvial deposition. This interpretation is consistent with previous sedimentological studies of the Morrison Formation, as the combination of greenish-grey mudstones and red mudstones have been interpreted to represent stagnant water and floodplain deposits (Moberly 1960). Facies Sd-a is interpreted to represent fluvial deposition in a channel and point bar, based on the large-scale trough cross-stratification, association with a basal lag deposit, and stratigraphic relationship to facies Stl and other facies in this association (Mirsky 1962). The association of facies Sp-a with facies Sd-a suggests that the planar lamination formed in a fluvial channel as an upper flow regime deposit (Ashley 1990; Miall 2010), but planar lamination can also form in overbank, abandoned channel, or waning flood deposits (Miall 2010).

Depositional Model: Open-coast Tidal Flats

The four facies associations described above display consistent relationships with one another and form a complete depositional system. The wave-dominated shelf facies association is in the stratigraphically lowest position and is usually sharply overlain by either the shoreface or tidal flat facies association. The shoreface and tidal flat facies associations are strongly associated with one another, alternating in some places to make up the middle portion of the stratigraphic column. Finally, the alluvial plain facies association caps the succession, generally sitting conformably on the deposits of the tidal flat association. A disconformable relationship between the alluvial plain facies association and the shoreface or tidal flat facies association is observed at depositionally updip locations.

The close stratigraphic relationship between the shoreface facies association and the tidal flat facies association is unusual in that tidal flats and wave-dominated coast are generally thought of as distinct environments, existing at opposite corners of the environmental spectrum (Boyd et al. 1992; Yang et al. 2005). In the study area, however, deposits of the shoreface facies association pass conformably upwards into deposits of the tidal flat association, indicating the lateral adjacency of co-existing environments (Fig. 3.12). Studies of the Korean and Indian coasts have documented the existence of open-coast tidal flats, similar to the recently described tidally modulated shorefaces (Dashtgard et al. 2009), which seasonally display features consistent with both wave-dominated shorefaces and tidal flats (Alexander et al. 1991; Yang et al. 2005; Saha et al. 2011; Fan 2012; Jo and Choi 2016). Seasonal variation is generally not well preserved in the rock record, and no evidence of seasonality was observed in this study.

Many features in the Windy Hill Sandstone are consistent with deposition on an open-coast tidal flat. Yang et al. (2005) lists several criteria for the distinction of open-coast tidal flats, including an abundance of mud pebbles and rip-up clasts, herringbone cross-stratification and other indicators of tidal influence, commonly observed climbing ripples, and the formation of planar lamination. A wide variety of rip-up clasts are observed in the study area and exhibit a range of grain-sizes from mud to sand (Fig. 3.8). The large sizes of these intraclasts is attributed to a combination of high shear stress and partial cementation on a sandy, open-coast tidal flat. Herringbone cross-stratification and climbing ripples are also common in the study area (Fig. 3.7A), further supporting the interpretation that the shoreface and tidal flat facies association together comprise an open-coast tidal flat. Additionally, studies of modern open-coast tidal flats predict a sharp-based fining-upward succession that overlies an erosional lag with shell fragments and mud rip-ups (Alexander et al. 1991), similar to the Windy Hill Sandstone (Fig. 3.6). Successions in modern open-coast tidal flats are not capped by landward salt marshes or extensive mudflats as typical tide-dominated deposits would be (Alexander et al. 1991), also consistent with the Windy Hill. The upper shoreface portion of an open-coast tidal flat does not pass landwards into a foreshore as it does on a wave-dominated coast because the coastal gradient is not as steep (Masselink and Short 1993; Yang et al. 2005). Therefore, wave ripples and planar lamination similar to the tidal bedding described in macrotidal environments along the Korean coast form instead of foreshore structures such as seaward-inclined laminae (Park et al. 1995; Yang et al. 2005). In the Windy Hill Sandstone, wave ripples are common and planar lamination, diagnostic of facies Sp-t, is regularly observed in the study area. The formation of facies Sp-t and its association with facies Sr-t and facies Sm-t (Fig. 3.7F) is attributed to the swash and backwash processes that act on open-coast tidal flats in combination with the spring and neap tide processes that are responsible for tidal bedding (Clifton et al. 1971; Park et al. 1995; Yang et al. 2005).

The interpretation of the shoreface facies association and the tidal flat facies association as an ancient open-coast tidal flat is also consistent with the observed relationships of these facies associations with the wave-dominated shelf facies association and the alluvial plain facies association, since these environments are expected downdip and updip of an open-coast tidal flat (Fig. 3.12). This suggests that the Redwater Shale, Windy Hill Sandstone, and Morrison Formation were contemporaneous within the basin rather than representing temporally distinct environments as has been suggested previously (Pipiringos and O'Sullivan 1978; McMullen et al. 2014).

Sequence Stratigraphic Framework

Sheep Mountain Transect

The approximately 11 km long Sheep Mountain transect is located in the central part of the study area and is roughly parallel to depositional dip (Fig 3.4, B-B'). In this area, the wave-dominated shelf facies association of the Redwater Shale contains one or more bedsets of facies Gc encased in facies M of the wave-dominated shelf facies association (Fig. 3.13). These shell beds have sharp, erosional bases with evidence of stratigraphic condensation and are interpreted as surfaces of forced regression. Stratigraphic condensation, i.e. slow net rates of deposition, is indicated by concentrations of pyrite, large shell accumulations, and firm ground trace fossils, such as *Thalassinoides* (Fig. 3.14; Posamentier et al. 1992; Catuneanu 2006; Buatois and Mángano 2011). Facies changes over uncharacteristically small intervals in the column, or telescoped sections, are also present and are consistent with the presence of surfaces of forced regression (Fig. 3.14; Catuneanu 2006). Additionally, carbonate concretions, which have been shown to be associated with forced regressions and hiatal deposits (Raiswell and Fisher 2000; Raiswell et al. 2002; Machent et al. 2012; Marshall and Pirrie 2013), are locally observed in facies M along the Sheep Mountain transect (Fig. 3.13, Sheep SWF). Where concretions form because of decreased sedimentation rate at a hiatus, they form within the sediment below the hiatal surface (Raiswell and Fisher 2000; Raiswell et al. 2002; Machent et al. 2012; Marshall and Pirrie 2013), allowing for the identification and correlation of a surface of forced regression above these features. The identification of surfaces of forced regression places the upper Redwater Shale in the falling-stage systems tract (Hunt and Tucker 1992; Posamentier et al. 1992; Catuneanu 2006).

The upper contact of the Redwater Shale with the Windy Hill Sandstone is generally sharp and overlain by a shelly lag or amalgamated beds of the shoreface or tidal flat facies associations. These abrupt shifts to the shoreface facies association are interpreted as surfaces of forced regression where marine erosion resulted in the formation of sharp-based shorefaces (Posamentier et al. 1992; Catuneanu 2006). The close spacing of columns measured at the Sheep Mountain exposure and the use of UAV-based methods allowed surfaces of forced regression to be correlated along the B-B' line (Fig. 3.13). At Sheep Mountain, sharp-based deposits bounded below by surfaces of forced regression form shingled depositional tongues that have internal facies relationships consistent with Walther's Law, but that are surrounded by the deeper water facies of the wave-dominated shelf facies association. Within an individual depositional tongue, facies Gc is found downdip, followed by sandy facies of the shoreface facies association at medial locations and by facies of the tidal flat association at the most updip positions. These depositional packages pinch out downdip as the sudden shallowing has progressively less environmental effect in deeper water. Surfaces of forced regression become less apparent downdip, presumably because wave erosion is less efficient downdip (Bruun 1962).

Surfaces of forced regression terminate updip at a prominent and laterally traceable flooding surface. This flooding surface merges downdip with the uppermost and most distal surface of forced regression. There is no direct evidence for subaerial exposure at the Sheep Mountain exposure, implying that this surface of forced regression and the combined surface is the sequence boundary, marking the end of the falling-stage systems tract (Hunt and Tucker 1992; Catuneanu 2006).

Above this combined sequence boundary and flooding surface, a weakly progradational stacking pattern is developed. Updip at Sheep Mountain, the shoreface facies association passes upwards into several tidal flat parasequences that pass upwards into the alluvial plain facies association (Fig. 3.13). At more medial and downdip locations are repeated parasequences with shoreface facies in their lower part and tidal flat facies in their upper part, suggesting a stacking pattern close to aggradational (Fig. 3.13). Alluvial plain facies of the Morrison Formation prograde over these tidal flat and shoreface facies associations of the Windy Hill Sandstone, marking the end of marine deposition (Fig. 3.13). These observations and the overall shallowing upwards trend, combined with the position of these parasequences deposits above deposits of the falling-stage systems tract, imply that the upper portion of the Windy Hill Sandstone and the lower Morrison Formation were deposited in the lowstand systems tract (Van Wagoner et al. 1990; Hunt and Tucker 1992; Catuneanu 2006).

No pronounced flooding surface was identified above these lowstand deposits, indicating the absence of a transgressive surface and transgressive systems tract in the Sheep Mountain area.

Regional Transect

The regional transect is 420 km long and is approximately parallel to depositional dip (Fig 3.4, A-A'). Although sections along this transect were not as closely or evenly spaced, the characterization of stratigraphic architecture at Sheep Mountain makes it possible to recognize similar architectures in columns along the regional line. Additionally, stacking patterns are easier to identify at some of the regional localities, allowing for the recognition of progradationally stacked highstand deposits. Weak progradational stacking is observed in two columns (Fig. 3.15, Newton Lakes SW, Camp Skeeter SW) and is manifested as an increase in the frequency and thickness of isolated sand beds in facies M of the wave-dominated shelf facies association and facies Sr-s of the shoreface facies association. This observed progradational stacking and its position in the section at a stratigraphic level below the falling stage deposits identified at Sheep Mountain are consistent with deposition in the highstand systems tract (Van Wagoner et al. 1990; Hunt and Tucker 1992; Catuneanu 2006).

Surfaces of forced regression were also identified along the regional transect and exhibit the same shingled architecture as was observed at Sheep Mountain, although detailed correlation is generally not possible because of the large spacing between outcrops compared with Sheep Mountain (Fig. 3.13; Fig. 3.15). Only one set of outcrops along the regional transect are less than 5 km apart, and sandstone bodies here are bounded below by surfaces of forced regression. These bodies thin downdip, eventually pinching out completely (Fig. 3.15; Cottonwood Creek SW, Alcova East SW). The surfaces of forced regression observed along the regional transect support the interpretation that the upper Redwater Shale and lower Windy Hill Sandstone record deposition in the falling-stage systems tract.

Distal (i.e. northernmost) localities along the regional transect are similar to Sheep Mountain in that they lack evidence for subaerial exposure above the falling-stage systems tract. Instead, a final surface of forced regression marks the beginning of the lowstand systems tract in the Windy Hill Sandstone (Fig. 3.15). This final surface of forced regression is a marine surface correlative with the sequence-bounding unconformity, and it often occurs at or above the sharp contact between the Redwater Shale and Windy Hill Sandstone. This sharp contact is typically a surface of forced regression, although it is not the same surface throughout the basin, despite the similar stratigraphic position. The interpretation that the contact between the Redwater Shale and Windy Hill Sandstone is generally a surface of forced regression implies that, at updip localities, any existing subaerial unconformity would be at a stratigraphic position above this contact. This is observed in the field, and this unconformity becomes more easily identifiable at increasingly updip locations where the duration of subaerial exposure was presumably longer (Van Wagoner et al. 1990). At medial locations (i.e. Thermopolis SW), this surface is characterized by a sharp contact between the tidal flat or shoreface facies association and the alluvial plain facies association (Fig. 3.15, Thermopolis SW; Fig. 3.16) with unusually large or abundant rip-up clasts (Fig. 3.16). At more updip locations (i.e. Alcova East SW), deposits of the shoreface facies association and the tidal flat facies association become increasingly thinner, culminating in the tidal flat facies association resting directly on the wave-dominated shelf facies association at the most updip column, where iron nodules and iron staining are also present (Fig. 3.15, Seminoe Dam SW; Fig. 3.17). Surfaces of forced regression are also observed below this contact, and the entire transition from the wave-dominated shelf facies association to the alluvial plain facies association is uncharacteristically thin and may represent a telescoped section, supporting the interpretation that deposits below this unconformity belong to the falling-stage systems tract (Fig. 3.17; Van Wagoner et al. 1990; Hunt and Tucker 1992; Catuneanu 2006). While erosional features or other evidence of subaerial exposure are not well developed, this facies change is more abrupt than typically seen at surfaces of forced regression in this study area, and this surface is therefore interpreted as a subaerial unconformity defining a sequence boundary.

Downdip to the north, deposits overlying the sequence boundary are characterized by an aggradational stacking pattern with no net change in water depth until the progradation of the Morrison Formation (Fig. 3.15). The parasequences here are bounded by flooding surfaces resulting from small rises in sea level that interrupt the overall progradation of the Morrison Formation. These flooding surfaces are reflected in transgressive lags that form some of the shell gravels observed in the field (Fig. 3.15, Camp Skeeter SW, Gypsum Spring Road SW). The overall shallowing, along with the position of the deposits relative to the sequence bounding unconformity and the surfaces correlative with it, place this upper portion of the Windy Hill Sandstone and the basal Morrison Formation in the lowstand systems tract (Van Wagoner et al. 1990; Catuneanu 2006).

Red Gulch

No incision or erosional truncation at the sequence boundary was observed along the Sheep Mountain and regional transects. The Red Gulch area is an exception to this pattern and differs in its architecture. At Red Gulch, a single set of large angular forsets is present, and the erosional surface at their base truncates the beds underneath (Fig. 3.18). The erosion at this site was studied in detail, and the depth of incision was measured at approximately 5 m. Previous work reported twice this amount of incision into the Redwater Shale by the Windy Hill Sandstone (McMullen et al. 2014), contributing to the interpretation of this surface as a subaerial sequence boundary. Such incision was not observed in this study, even at the exposures studied by McMullen et al. (2014), and Red Gulch is the only locality in the study area where incision was observed. A depth of incision of 5 m is reasonably attributed to channel-scale erosion, and it is unnecessary to invoke a sequence boundary to explain this feature. That this is a localized occurrence suggests that it is more likely to be channel erosion than a sequence boundary, as one of the criterion for the identification of sequence boundaries is regional extent (Van Wagoner et al. 1990). Furthermore, the single set of large foresets observed immediately overlying the incision surface are consistent with lateral accretion surfaces formed by point bar migration (Fig. 3.18), supporting the interpretation that this feature was formed in a channel setting. Tidal features, such as reversing current ripples, are also present, suggesting that the channel responsible for the incision was a tidal inlet (Uhlir et al. 1988).

Another possible option is that this incision surface is a surface of forced regression with a greater degree of marine erosion, but the appearance is inconsistent with observations of surfaces of forced regression elsewhere in the study area (Fig. 3.18). There also does not appear to be abrupt shallowing, as the tidal inlet facies above is incising into its own shoreface deposits and does not violate Walther's Law. Additionally, progradational stacking of parasequences is observed beneath the incision (Figure 3.18). This further supports the tidal inlet channel interpretation because if the incision were the result of a sequence boundary, surfaces of forced regression would be expected rather than parasequences (Catuneanu 2006). The presence of progradational stacking suggests that this outcrop represents deposition in the highstand systems tract. This is again consistent with the interpretation of these deposits as a tidal inlet because modern tidal inlets are coupled with lagoons or bays that are expected to exist in the highstand systems tract after flooding (Catuneanu 2006). These deposits at Red Gulch represent the shallowest environment that can be attributed to the highstand systems tract in the study area and are markedly different from the offshore-transition deposits of the highstand portions of the Redwater Shale observed along the Sheep Mountain and regional transects. The uniqueness of these deposits suggests a connection to the Sheridan Arch, a structural high that caused locally shallower water depths and thinning of strata during the Jurassic (Schmude 2000). The well-developed progradationally stacked parasequences here are also attributed to the Sheridan Arch, with the uplift resulting in slightly decreased accommodation, favoring progradation as sediment filled the basin.

Discussion

Placement of the J5 Unconformity

The contact between the Redwater Shale and the Windy Hill Sandstone is interpreted here to be multiple surfaces of forced regression rather than a subaerial unconformity. Previous studies have placed a regional unconformity, the J5, at this stratigraphic position (Pipiringos and O'Sullivan 1978; McMullen et al. 2014). In depositionally downdip (northern) areas, physical evidence of the J5 unconformity is limited. To the south, the J5 unconformity has been inferred based on truncation of the Redwater Shale and Pine Butte members of the Sundance Formation (Pipiringos and O'Sullivan 1978). The J5 surface has been variously described as a flat surface lacking channels and erosional relief (Pipiringos and O'Sullivan 1978) to displaying large amounts of incision (McMullen et al. 2014).

Regional placement of the J5 unconformity is likely based on the largely consistent sharp contact between the Windy Hill Sandstone and Redwater Shale. While this is regularly observed in the field, the contact between the Redwater Shale and Windy Hill Sandstone is not the same at every location and a sharp contact does not necessarily mean that there is a subaerial unconformity. Instead, these contacts, interpreted in this study as surfaces of forced regression, get progressively younger downdip according to the principle of superposition, recording the progressive fall in sea level. Although these surfaces of forced regression can be similar in appearance and stratigraphic position, the contact between the Redwater Shale and Windy Hill Sandstone should not be correlated as a single surface. Additionally, the Redwater Shale and Windy Hill Sandstone are lithostratigraphically named units and are, by definition, regionally extensive for mapping purposes. All rocks falling under a specific name, however, were not deposited in the same environment at the same time and chronostratigraphic depositional packages must be considered separately from lithostratigraphic names. Linking up surfaces of forced regression that exist at a given horizon between two lithostratigraphically named units leads to a surface that is artificially regionally extensive and easily misinterpreted as a sequence boundary. Additionally, this can result in interpretations of depositional environments with exceptionally large geographic extents.

At Sheep Mountain and farther north, there is no evidence of subaerial exposure or erosional relief between the Redwater Shale and the Windy Hill Sandstone. Subaerial exposure was observed at updip regional localities, but was identified stratigraphically higher, capping the Redwater Shale at only the most updip locality (Fig. 3.15, Seminoe Dam SW). In these updip (southern) portions of the study area, it is possible that the J5 unconformity lies within the Morrison Formation rather than at the contact between the Redwater Shale and Windy Hill Sandstone. Previous research in Colorado and Utah has indicated the existence of sequence-bounding unconformities within the Morrison Formation based on paleomagnetic data and the identification of paleosols (Steiner 1998; Demko et al. 2004), but it is unknown if any of these Morrison unconformities can be traced north into the study area. In the downdip (northern) portions of the study area, where no subaerial exposure was identified, the last surface of forced regression is correlative with the sequence bounding unconformity (Catuneanu 2006), and the regional J5 surface should be placed here. This last surface of forced regression is also generally higher in the section than the contact between the Redwater Shale and Windy Hill Sandstone, also indicating that the J5 occurs stratigraphically higher than generally interpreted.

This re-evaluation of the position of the J5 unconformity has implications for paleogeographic reconstructions of the Sundance Seaway. The previous interpretation of the J5 unconformity between the Redwater Shale and Windy Hill Sandstone implies that the environments in which they were deposited were temporally distinct and that a regression and transgression would have occurred. This transgression, called the "Windy Hill Sea" by some workers (Pipiringos and O'Sullivan 1978; Johnson 1992), would not have existed if the J5 does not separate the Redwater Shale and Windy Hill Sandstone. Instead, the offshore transition environment represented by the Redwater Shale would have existed contemporaneously downdip of the open-coast tidal flat of the Windy Hill Sandstone and the alluvial plain of the Morrison Formation. This means that all of these deposits are generally time-transgressive

(Fig. 3.1B or 3.1C) and that the Windy Hill Sandstone and Redwater Shale are likely closer in age at any one location than previously thought (Pipiringos and O'Sullivan 1978; McMullen et al. 2014). A significant hiatus in deposition should not be indicated between the Redwater Shale and Windy Hill Sandstone, as deposition was continuous in the medial and distal portions of the study area.

Identification and Occurrence of Tidal Units in a Sequence Stratigraphic Framework

The identification of the Windy Hill Sandstone as an open-coast tidal flat has implications for recognition of other mixed-environment deposits in the rock record. The open-coast tidal flat was recognized in this study primarily based on the criteria outlined in Yang et al. (2005). Perhaps the most noticeable feature is that the Windy Hill Sandstone is similar to a cross-stratified shoreface, but it also preserves abundant tidal features. Both herringbone cross-stratification and climbing ripples are abundant, as predicted by Yang et al. (2005). Mud pebbles are also common, although they were generally found at the base of the shoreface deposits in transgressive lags rather than at the base of storm beds (Yang et al. 2005). Sandstone rip-up clasts are also relatively common (Fig. 3.8) and are attributed to incomplete cementation on a sandy tidal flat as well as to elevated shear stress associated with storms. Furthermore, Yang et al. (2005) predicted that gently inclined lamination typical of beaches would not be found on open-coast tidal flats. This was the case with the Windy Hill Sandstone, and again as predicted, wave ripples and planar lamination were observed (Yang et al. 2005), consistent with modern open-coast tidal flats, where tidal bedding is a common sedimentary structure (Alexander et al. 1991; Park et al. 1995). Modern open-coast tidal flats are described as alternating seasonally between tidal flats and shorefaces, rather than both environments existing simultaneously (Yang et al. 2005). Such seasonality was not identified in the Windy Hill Sandstone, likely because of the short time scales of seasonality with respect to preservation. Recognition of open-coast tidal flats in other settings should likewise consider a potential lack of observable seasonality.

The interpretation of these tidal deposits in an overall regressive position in the late falling-stage to early lowstand systems tracts reinforces the idea that tidal deposits can be found in a wide variety of sequence stratigraphic settings. While common in the transgressive systems tract and in incised valleys, tidal deposits are not specifically tied to deposition in these settings as has been previously suggested (Shanley and McCabe 1991; Van Wagoner 1991; Dalrymple et al. 1992; Cattaneo and Steel 2003; Chentnik et al. 2015; Jordan et al. 2016). Studies of other ancient tidal and mixed-energy deposits, such as the Cretaceous Sego Sandstone of Utah, also indicate the presence of tidal units in regressive settings (Willis and Gabel 2001, 2003; Lee et al. 2007; Desjardins et al. 2012; Willis and Fitris 2012; Legler et al. 2014; Ainsworth et al. 2015; Burton et al. 2016). Likewise, Pleistocene and recent deposits of Korea are tidally dominated through all systems tracts (Park et al. 1998; Lim and Park 2003). Collectively, these argue that tidal influence should not be taken as direct of an estuary or of a particular systems tract. Additionally, process regime changes can act on short times scales (~1000 years) and can influence the appearance of depositional sequences and the interplay of waves and tides (Yoshida 2007; Pontén and Plink-Björklund 2009). This variability must be considered when making sequence stratigraphic interpretations, and stacking patterns and stratigraphic surfaces should be used to identify systems tracts rather than depositional environment and the relative abundance of wave and tide energy.

Continuous Progradation and Tectonic Influence

Throughout the study area, the lower Morrison Formation is interpreted as the lowstand progradation of an alluvial plain over the open-coast tidal flat deposits of the Windy Hill Sandstone. In the study area, these alluvial deposits are characterized by an assortment of variegated mudstones and generally lack the channel-sandstone bodies that would be expected if the Morrison Formation were deposited in a low-accommodation setting equivalent to the marine lowstand systems tract (Boyd et al. 2000; Catuneanu 2006). Many of the features diagnostic of a low-accommodation systems tract, such as multiple and well-developed paleosols, compound incised valleys, and amalgamated sand bodies (Boyd et al. 2000; Catuneanu 2006), were not identified in the study area. Instead, the observed low sand to mud ratio and single-storied channels are consistent with a high-accommodation systems tract in a fluvial setting. The apparent jump from the lowstand Windy Hill to high-accommodation Morrison could potentially be explained by the existence of the transgressive surface near the top of the Windy Hill, but there is no evidence for such a prominent flooding surface at this stratigraphic position. Downdip, there is a poorly developed flooding surface in the upper portion of the Windy Hill Sandstone that is recognized based on the presence of marine fossils, including starfish (Gunderson 2015; Blake and Guensburg 2016). These starfish indicate that some flooding must have occurred to bring the open-coast tidal flats of the Windy Hill into a marine environment prior to the progradation of the Morrison Formation. This flooding, however, does not extend updip and is not as prominent as what would be expected of a transgressive surface.

Alternatively, an increase in sedimentation rate relative to accommodation rate during the progradation of the Morrison Formation could result in the deposition of single-storied channels and a low sand to mud ratio, resulting in deposits that look consistent with the high-accommodation systems tract but actually correspond to a low-accommodation time period. This could be achieved by either increasing the sedimentation rate or by decreasing the accommodation rate, or by some combination of the two. Sedimentation rate is modelled as fairly constant over long time scales, but accommodation can vary markedly based on the tectonic setting, making a decrease in the accommodation rate more likely. Tectonic studies in Utah and Idaho have shown a regional increase in subsidence rates during the Middle Jurassic caused by flexural subsidence in the retroarc foreland basin (Bjerrum and Dorsey 1995). This was followed by a pronounced decrease in subsidence rates at 157 million years, just as progradation of the Morrison Formation was occurring (Bjerrum and Dorsey 1995). The decreased subsidence rate at this time supports the interpretation that the accommodation rate was low relative to the sedimentation rate. The progradational nature of the deposits implies that the accommodation rate was in fact lower than the sedimentation rate, and if the accommodation rate were to remain lower, then continuous progradation would occur. This would form a depositional sequence lacking a transgressive systems tract. Continuous progradation is observed in the study area, and no retrogradational stacking or transgressive surface is present (Fig. 3.18).

The absence of a transgressive systems tract leads to an inability to distinguish the lowstand systems tracts from any highstand deposits that may be present based on their position in the sequence. Additional, this leads to confusion in the name of the systems tract and uncertainty as to what systems tract the deposits should be assigned to in the traditional sequence stratigraphic models such as Van Wagoner et al. (1990) or Hunt and Tucker (1992). It would be possible in this situation to define a new systems tract that would be the conceptual opposite of the shelf margin systems tract of type 2 sequences (Posamentier and Vail 1988; Van Wagoner et al. 1990), but this could add to confusion in the literature regarding systems tracts and relative sea level. Alternatively, the accommodation succession method proposed by Neal and Abreu (2009), may be a more suitable interpretation method, relying purely on stacking patterns and disassociating description of the depositional sequence from relative sea level. This observation-based accommodation succession method has been used with success (Zhu et al. 2012) and explains stacking patterns using the ratio of accommodation rate to sedimentation rate (dA/dS) without implying any link to position on sea-level curves (Neal and Abreu 2009; Neal et al. 2016). This is especially valuable for studies of sequence stratigraphy concerned with deposits in both the marine and terrestrial realms. Because the accommodation succession method is concerned only with stacking patterns, there is no need to switch between the traditional systems tracts in marine sequence stratigraphy (Van Wagoner et al. 1990; Hunt and Tucker 1992) and the low and high accommodation systems tracts of terrestrial sequence stratigraphy (Boyd et al. 2000), minimizing the possibilities of error in interpretation. In the case of the Windy Hill Sandstone and basal Morrison Formation, the accommodation succession method provides a helpful description, as the continuous progradation is explained by a dA/dS ratio that remained less than one (Fig. 3.18). The subsidence rates calculated for the Morrison Formation (Bjerrum and Dorsey 1995) indicate that dA/dS is less than one and decreasing, suggesting that the portions of the Windy Hill Sandstone and the Morrison Formation above the sequence boundary are in the progradational-aggradational (PA) and aggradational-progradational-degradational (APD) systems tracts (Fig. 3.18; Neal and Abreu 2009), although a detailed study of the stratigraphically higher portions of the Morrison Formation is needed to confirm this.

The observationally based dA/dS methods allows a sequence stratigraphic framework to be constructed without making any assumptions about the mechanisms controlling the framework (Neal and Abreu 2009; Neal et al. 2016). Once a framework is in place, deviations are easily identified and the mechanisms of accommodation and sedimentation change can be hypothesized (Neal and Abreu 2009; Neal et al. 2016). The continuous progradation of the Morrison Formation over the Windy Hill Sandstone may be an example of localized tectonics as a mechanism influencing the manifestation of depositional sequences. This is also the case at the Red Gulch area, as the Sheridan Arch produced a deviation from the predicted stratigraphic architecture. This implies that tectonics are not always basin-wide processes and can deviate from typical sinusoidal models of accommodation (Catuneanu 2006). Foreland basins, such as the one containing the Sundance Seaway, are especially prone to variable accommodation as some portions of the basin undergo uplift while others undergo subsidence (Bjerrum and Dorsey 1995; Tankard 1986; White et al. 2002; Liu et al. 2011). Spatial and temporal variability in tectonics has been hypothesized as a mechanism for forming Cretaceous isolated shallow-marine sand bodies in the Bighorn and Uinta Basins that were previously interpreted as offshore sand bars (Fielding et al. 2014; Hutsky and Fielding 2016) similar to the Windy Hill Sandstone. In the Bighorn Basin area specifically, these deposits have many features consistent with the falling-stage systems tract but do not fit completely with traditional systems tract definition (Fielding et al. 2014) and are another example of a case where the accommodation succession method could be applied. Deviations from the architecture that eustasy-driven sequence stratigraphy predicts indicates that other mechanisms also affect the system, and this must be considered when interpretations are made, as tectonic variability can greatly influence the formation of depositional sequences.

Conclusions

1. The Late Jurassic Windy Hill Sandstone member of the Sundance Formation in Wyoming and southern Montana was deposited on an open-coast tidal flat, including both shoreface deposits and sandy tidal flat deposits. This illustrates the importance of considering depositional environments as existing along a spectrum rather than as discrete endmembers and reinforces that tidal features occur in many environments and are not necessarily associated with deposition in an estuary or in a transgressive setting.

This example of an open-coast tidal flat from the Windy Hill Sandstone confirms and expands on the pre-existing criteria for identifying this type of depositional environment.

2. Surfaces of forced regression were identified in the Redwater Shale and Windy Hill Sandstone at stratigraphic positions previously identified as the J5 unconformity. This interpretation places the J5 higher in the section than previously realized and implies that the Redwater Shale and Windy Hill Sandstone are contemporaneous in the basin. Previous placement of the J5 sequence boundary may have relied on the incorrect correlation of temporally distinct surfaces of forced regression and local incision. UAV-based photogrammetry methods were effectively used in this study to minimize data gaps between adjacent measured columns, improving the correlation and allowing for recognition of the shingled stratigraphic architecture of the Windy Hill Sandstone. UAV-based methods were also effectively used to trace bedding and contacts and to characterize depth and extent of incision.

3. The Redwater Shale, Windy Hill Sandstone, and Lower Morrison Formation preserve systems tracts that are part of two third-order depositional sequences. The Upper Redwater Shale deposits represent the late highstand and early falling-stage systems tract. The Windy Hill Sandstone deposits represent the late falling-stage systems tract and the lowstand systems tract, and the Lower Morrison Formation consists of lowstand deposits, but is unexpectedly muddy, suggesting a decrease in the rate of accommodation at 157 million years. These deposits exhibit continuous but unsteady progradation, indicating that certain tectonic settings where accommodation rates are low may form a depositional sequence without a transgressive systems tract. This illustrates that tectonic subsidence and the rate of accommodation may not vary sinusoidally through geologic time and that care must be taken when interpreting sequences deposited in tectonically active regions.

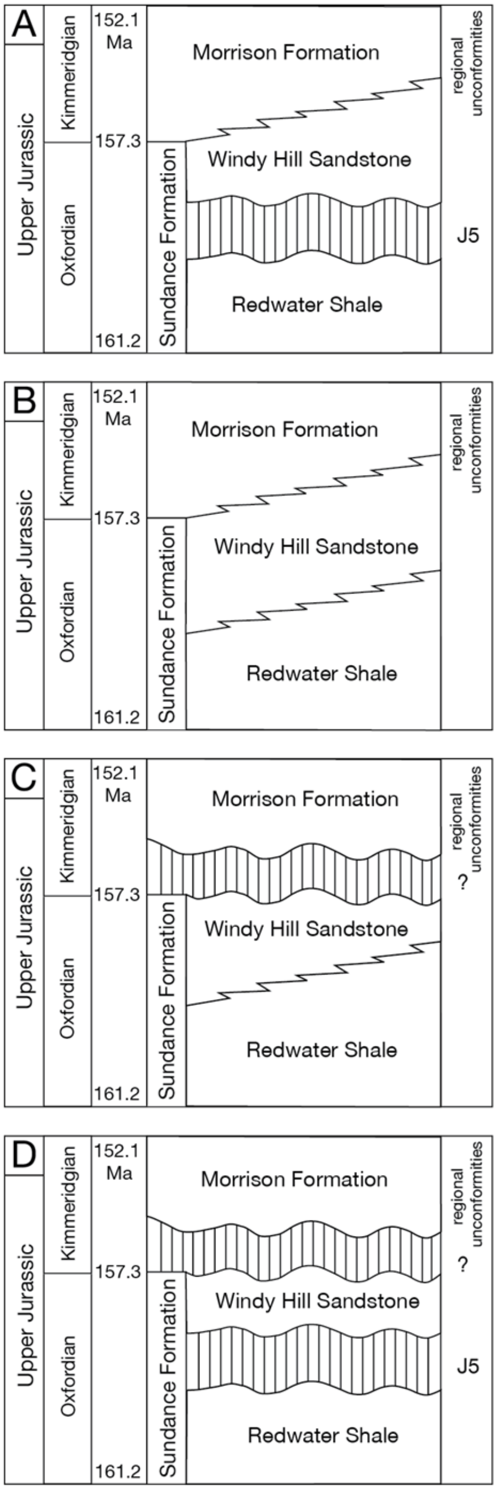

FIG. 3.1—Chronostratigraphic and lithostratigraphic interpretations of units in the Bighorn Basin. **A)** Accepted interpretation showing the J5 unconformity between the Redwater Shale and Windy Hill Sandstone (Pipiringos and O'Sullivan 1978; McMullen et al. 2014; Danise and Holland 2017). **B)** Conformable contacts consistent with delta progradation (Zeiner 1974). **C, D)** Variations of interpretations A and B that include an unconformity at the base of the Morrison Formation.

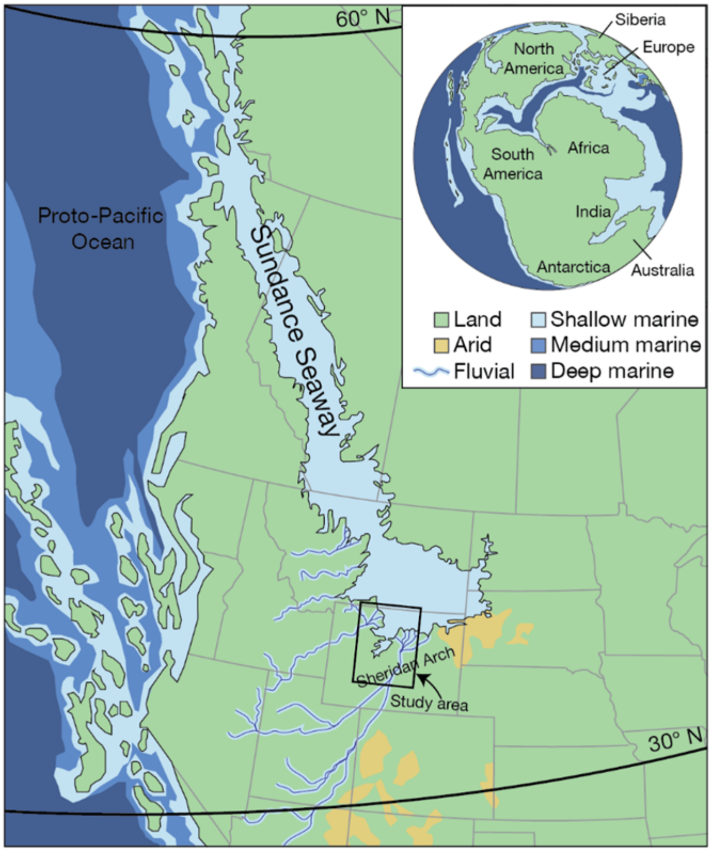

FIG. 3.2—Paleogeographic reconstruction of western North America during the Late Jurassic. Modified from Clement and Holland (2016), based on maps produced by Blakey (2014).

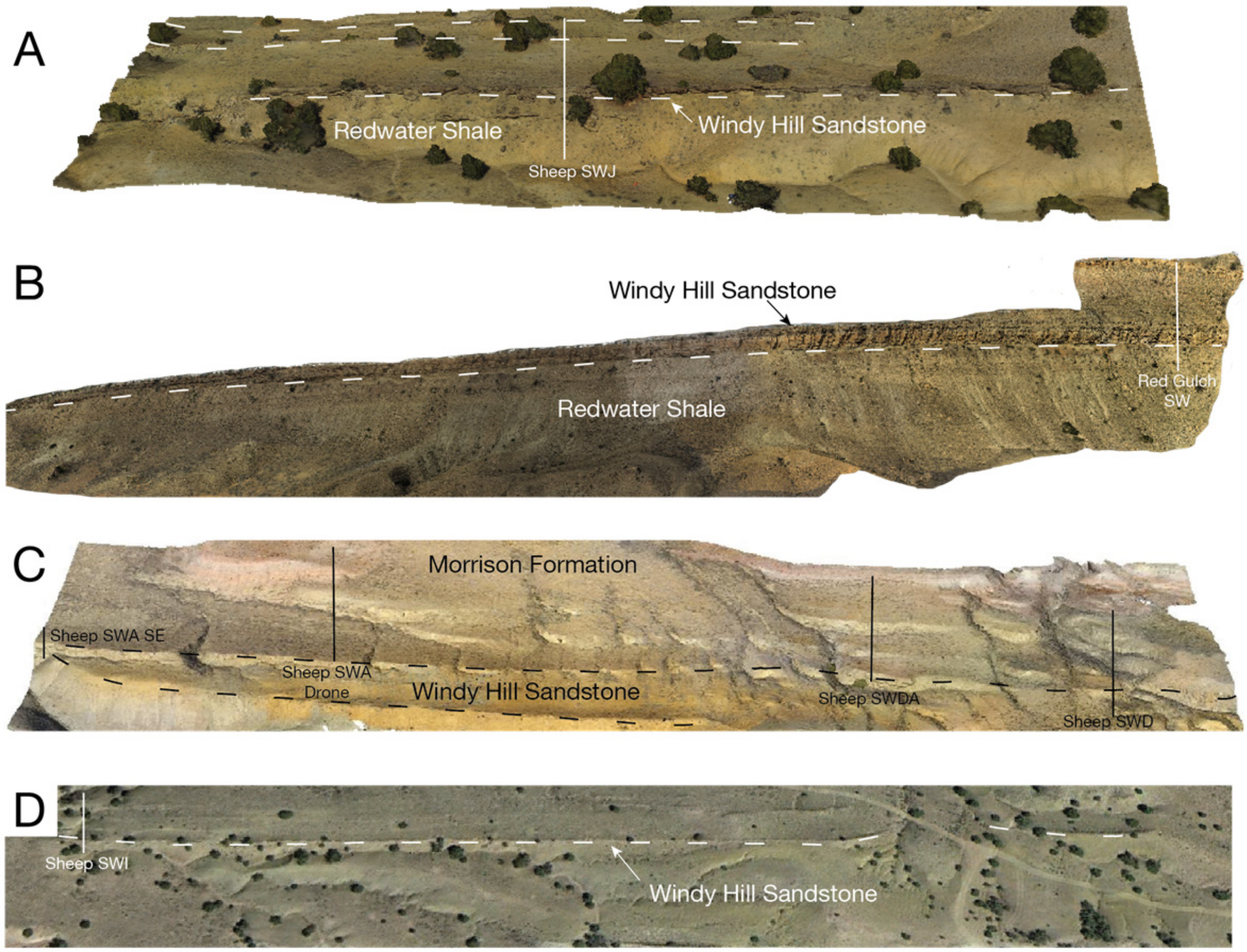

FIG. 3.3—Tabular geometry and laterally extensive ridges of the Windy Hill Sandstone. **A)** Point cloud showing tabular bedding at Sheep SWJ. **B)** Point cloud from Red Dome SW showing tabular bedding with no erosional relief or clinoforms. **C)** Point cloud between Sheep SWA and Sheep SWD viewed from above showing laterally extensive and traceable Windy Hill Sandstone ridges. **D)** Google Earth near Sheep SWI showing laterally continuous Windy Hill ridge with no erosional relief.

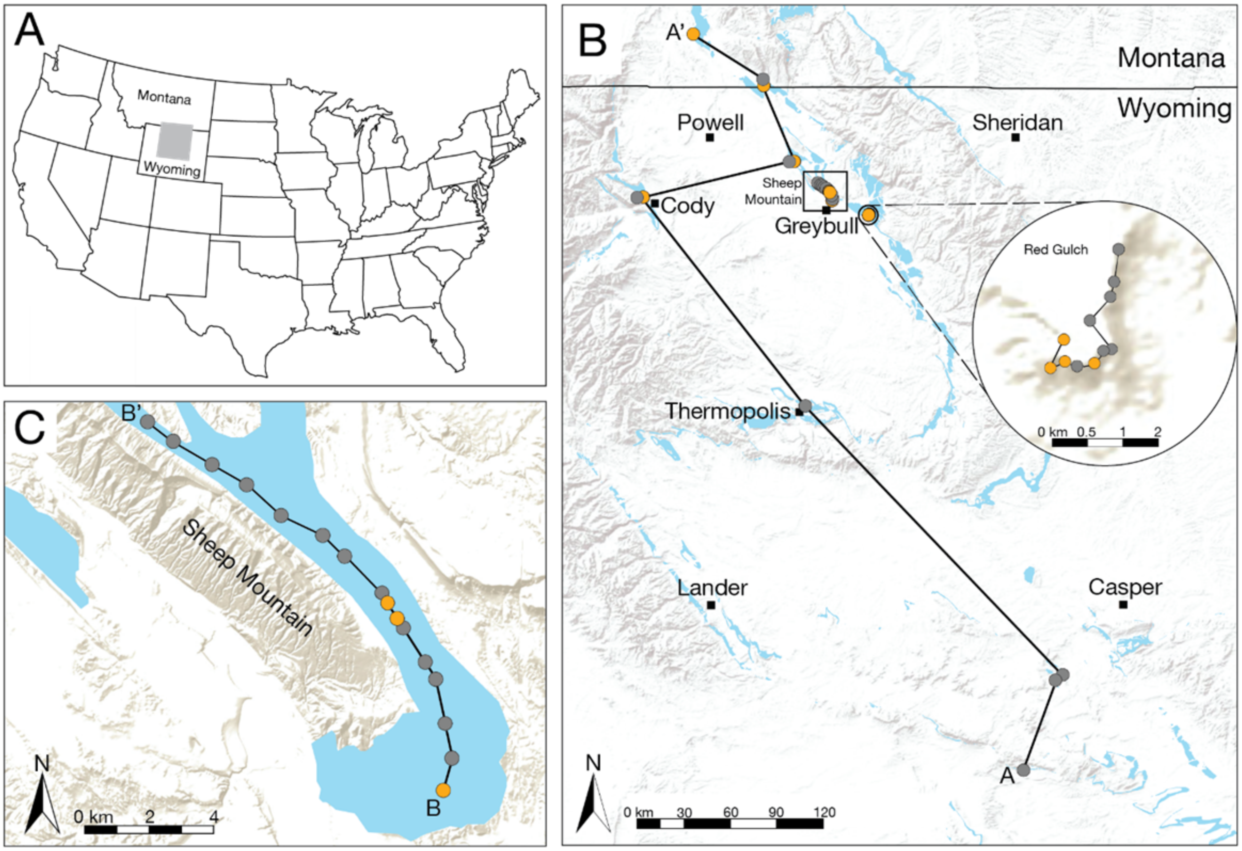

FIG. 3.4—Map of study area. **A)** United States with grey box showing extent of study area. **B)** Detail of study area. Jurassic outcrop shown in light blue, regional cross-section line A-A' shown in black, columns measured by hand shown in gray and columns measured with UAV techniques shown in yellow. Circle shows a zoomed view of the Red Gulch area where columns were measured closely in three dimensions. **C)** Map showing detail of the Sheep Mountain area (boxed portion from panel B). Locations along Sheep Mountain were spaced approximately 1 km apart and form a dip oriented cross-section line from B-B'.

TABLE 3.1—Wave-Dominated Shelf Facies Association

Facies	Sedimentology	Paleontology	Geometry and Contacts
M, mud (offshore transition)	***Mudstone to siltstone***, finely laminated to massive. Glauconitic with local carbonate concretion horizons. Thin sand interbeds locally present.	Body fossils include abundant belemnites (*Pachyteuthis)* and rare ammonites, echinoid spines, and serpulid tubes. Traces are rarely present and are primarily horizontal, including *Planolites, Palaeophycus,* and *Astericites.*	0.1 to over 10 m thick. Coarsens upwards into Facies Sr-s at select localities, regularly sharply overlain by facies of the tidal flat or shoreface association. Encases facies Facies Gc with sharp upper and lower contacts.

TABLE 3.2—Shoreface Facies Association

Facies	Sedimentology	Paleontology	Geometry and Contacts
Sr-s, rippled sand (lower shoreface)	Very fine to medium sand usually containing current and vortex ***ripple lamination***. Beds are very thin to thin and occasionally medium. Bioturbation is generally rare and does not obscure lamination. Planar lamination locally observed.	No complete body fossils, rare shell fragments locally present. Poorly preserved shell fragments locally present in small amounts. Rare trace fossils include *Planolites* and *Palaeophycus*.	0.1–0.7 m thick. Facies Sr-s coarsens gradational upwards into facies Sd-le. Upper contact with facies Gsd and Gst are sharp. Lower contact with facies M is sharp, upper tend to be gradational.
Sd-le, laterally extensive cross-stratified sand (upper shoreface)	Very fine to medium sand, poorly sorted with local shell fragments. Sedimentary structures include trough and tabular ***large-scale cross-stratification***. Set thicknesses generally 15–50 cm. Ripples locally present on foresets. Commonly glauconitic and well cemented with sand and mud rip-ups to 2 cm. Chert and wood fragments locally present.	Trace fossils absent. Body fossils include small bivalves, typically the oyster *Liostrea*, other shell fragments, rarely the belemnite *Pachyteuthis*, and starfish at Red Dome SW.	0.1–5 m thick. Basal contacts are sharp except where overlain by facies Sr-s. Grades upwards into facies Sr-t, Sb-t, Sp-t, and rarely Sr-s. Geometry is tabular.
Gsd, cross-stratified shell gravel (upper shoreface)	Poorly sorted fine to coarse sand with ***abundant large shells***. Trough and tabular ***large-scale cross-stratified*** with set thicknesses ranging from 30 cm to over 1 m. Iron staining and bed amalgamation locally present. Clay intraclasts to 6 cm and sand intraclasts to 8 cm are present. Chert and wood fragments locally present.	No trace fossils. Body fossils include bivalves such as the oyster *Liostrea* and the scallop *Deltoideum,* as well as belemnites. Shells are generally fragmented.	0.3 m–2 m thick. Basal contacts are sharp except when underlain by facies Gst. Basal contacts are occasionally erosional, with relief less than 1 m. Upper contact is sometimes sharp but typically grades into Facies Sd-le, Sr-t, Sb-t, or Sp-t. Composition is heterogeneous and can grade laterally into Facies Sd-le.
Gst, tabular shell gravel (shoreface lag)	Poorly sorted fine to coarse sand with ***abundant large shells***. Bedding is ***tabular*** and beds are generally amalgamated. Beds are thin to medium. Clay intraclasts to 4 cm, wood, chert to 1 cm, mud intraclasts and rare sand intraclasts to 4 cm are observed. Iron staining locally present; beds are well cemented except where iron staining is present.	No trace fossils. Body fossils include large pink recrystallized bivalves, the oyster *Liostrea,* the scallop *Deltoideum*, and rare belemnites.	Typically less than 1 m thick. Upper and lower contacts are sharp and locally irregular. Facies commonly holds up ridges where laterally extensive, but can be discontinuous over a few meters. Shell content is laterally variable.
Gc, *Camptonectes* shell bed	Poorly sorted mudstone with ***abundant large shell fragments*** of the scallop ***Camptonectes****.* Thin-bedded to medium bedded, beds are amalgamated and internally structureless.	No traces fossils. *Camptonectes* are abundant and other bivalves and belemnites are rare. Shells are usually broken into large fragments but are locally well preserved.	0.1–1 m thick. Upper and lower contacts are sharp with all other facies. Bedding geometry is tabular and units are generally laterally continuous.

TABLE 3.3—Tidal Flat Facies Association

Facies	Sedimentology	Paleontology	Geometry and Contacts
Sr-t, rippled sand (sandy tidal flat)	Very fine to medium sand with ***diverse ripple lamination***. Locally argillaceous (Sa). Ripples include current ripples, vortex ripples, herringbone ripples, climbing ripples, and rarely ladderback ripples. Very thin to thin bedded, locally medium bedded. Bioturbation is generally rare and does not obscure lamination.	Traces include both horizontal and vertical burrows such as *Curvolithus, Thalassinoides, Diplocraterion,* and *Asteriacites*. Pterosaur tracks locally present. Body fossils absent.	0.1–2 m thick. Upper contacts are generally sharp but can be gradational and co-occurring with Facies Sm-t or Sp-t. Gradationally overlies facies Sd-ch and facies Sd-le. Sharply overlain by facies Gst, Gsd, Sd-le, and Sd-ch. Rarely sharply overlies facies M.
Sm-t, massive sand (sandy tidal flat)	Very fine lower to medium sand with ***no lamination visible***. Locally argillaceous. Thin bedded to massive.	No trace or body fossils.	0.1–3 m thick. Gradational and co-occurring with facies Sr-t and Sp-t. Gradational overlies facies Sd-ch and Sd-le. Sharply overlain by facies Gst, Gsd, Sd-le, and Sd-ch.
Sp-t, planar laminated sand (sandy tidal flat)	Very fine to medium sand with ***planar lamination***. Very thin to thin bedded with little to no bioturbation.	Horizontal and vertical burrows including *Curvolithus, Thalassinoides, Diplocraterion, Planolites* and *Asteriacites*. Body fossils are absent.	0.1–1.5 m thick. Gradational and co-occurring with facies Sr-t and Sm-t. Sharply overlain by facies Gst, Gsd, Sd-le, and Sd-ch. Gradational overlies facies Sd-ch and Sd-le.
Sd-ch, discontinuous cross-stratified sand (tidal channel)	Very fine upper to medium sand, locally with shell fragments. Generally poorly sorted. Sedimentary structures include trough, tabular and sigmoidal ***large-scale cross-stratification***. Set thicknesses generally 15–50 cm. Ripples locally on foresets. Commonly glauconitic and well cemented with mud rip-ups to 2 cm.	Traces include *Thalassinoides,* and *Curvolithus.* Body fossils are small bivalves, typically *Liostrea*, and other shell fragments.	0.1–3 m thick. Basal contacts are sharp except where underlain by facies Gtl. Grades upwards into facies Sr-t, Sm-t, and Sp-t. Shell content varies laterally.
Gtl, shell gravel (tidal channel lag)	Poorly sorted fine to coarse sand with ***abundant large shells***. Large scale trough cross-stratification occasionally visible. Iron staining locally observed. Clay intraclasts to 6 cm and sand intraclasts to 8 cm. Chert and wood fragments locally present.	Rare *Thalassinoides*. Body fossils include bivalves such as *Liostrea.* as well as belemnites. Shells are generally fragmented.	0.3–1 m thick. Basal contacts are sharp, and rarely erosional with relief less than 0.5 m. Upper contact is often gradational with facies Sd-ch and occasionally gradational with facies Sr-t, Sm-t, and Sp-t. Rarely sharply overlies facies M.

TABLE 3.4—Alluvial Plain Facies Association

Facies	Sedimentology	Paleontology	Geometry and Contacts
Slt, silt with mud (floodplain)	Silt and mud, locally very fine sand, locally argillaceous. Weathers easily and exposure is usually poor. Variegated red, pink, white, green, or gray.	No trace or body fossils.	0.1– >2 m thick. Contacts are poorly exposed in the study area.
Sr-a, rippled sand (fluvial channel)	Very fine lower to medium sand with ***ripple lamination***. Locally argillaceous. Ripples are current ripples and rarely vortex ripples, with ***no tidal influence***. Very thin to medium bedded.	Traces include horizontal burrows, and possibly *Asteriacites*. Body fossils absent.	0.1–2 m thick. Contacts are generally sharp when overlain by facies Sd-a. Gradational into Facies Sm-a or Sp-a. Gradationally overlies Facies Sd-a.
Sm-a, massive sand (fluvial channel)	Very fine to medium sand with ***no lamination visible***. Often white to light tan in color. Beds are very thin to massive. Usually poorly cemented.	No trace or body fossils.	0.1–3 m thick. Gradational with Facies Sr-a and Sp-a. Sharply overlain by Facies Sd.
Sp-a, planar laminated sand (fluvial channel)	Very fine to medium sand with ***planar lamination***. Beds are very thin to thin and there is little to no bioturbation. Often white to light tan in color.	No trace or body fossils.	0.1–1.5 m thick. Gradational with Facies Sr-a and Sp-a. Sharp contacts with Facies Sd.
Sd-a, cross-stratified sand (fluvial channel)	Fine to medium sand. Generally poorly sorted. Sedimentary structures include trough and tabular ***large-scale cross-stratification***. Set thicknesses generally 10–50 cm. Mud intraclasts and wood locally present.	Trace fossils absent. Body fossils include relatively abundant bone fragments.	Up to 2 m thick. Basal contacts are sharp, grades upwards into Facies Sr-a, Sm-a, and Sp-a.

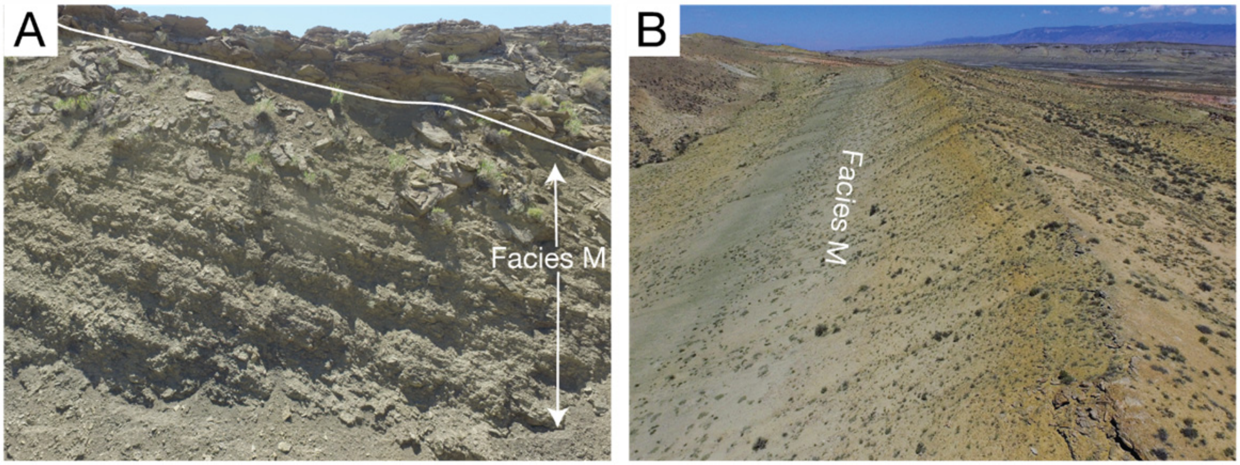

FIG. 3.5—Facies of the wave-dominate shelf facies association. **A)** Facies M with thin sand interbeds in the Redwater Shale, Camp Skeeter SW, 0–9.3 m. **B)** UAV image of facies M in the Redwater Shale near Sheep SWF.

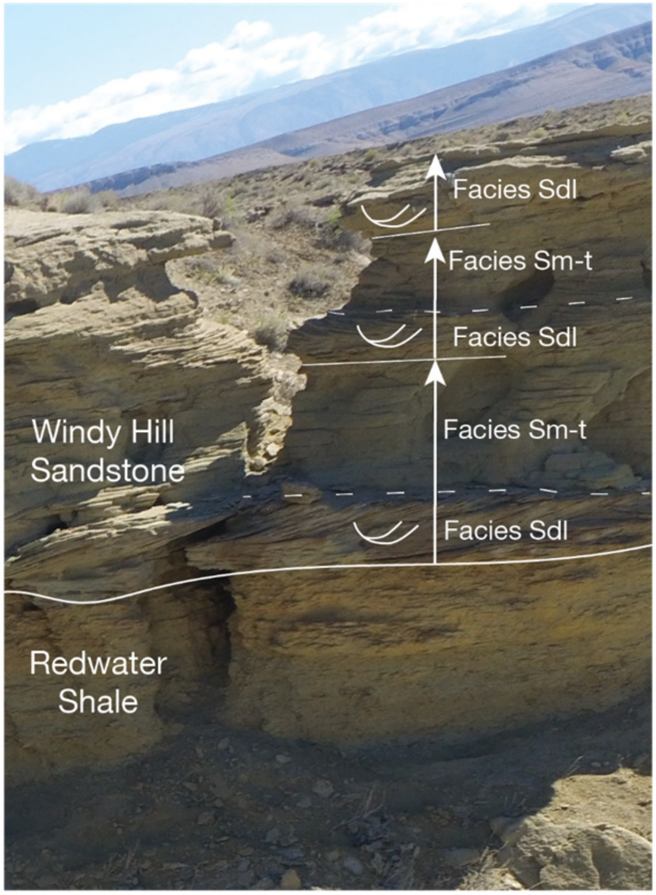

FIG. 3.6— Example of fining-upwards packages in the tidal flat facies association. Arrows indicate packages with cross-stratified sandstone at the base, fining into massive sand. Dotted lines indicate facies contacts, solid lines indicate sharp contacts bounding fining-upwards units. Image from Pantosaurus SW site, 7–12 m.

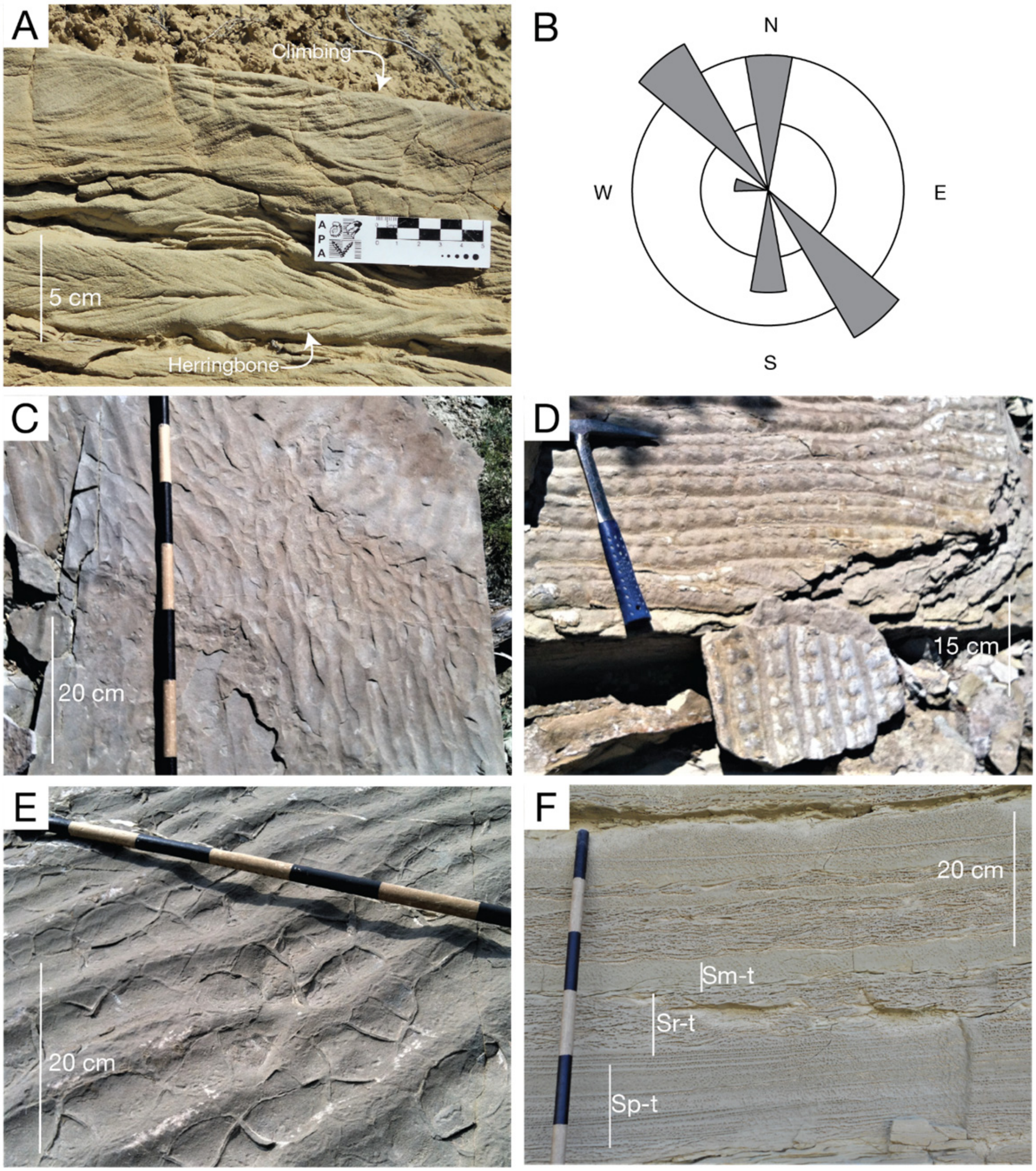

FIG. 3.7—Variety of ripples observed in the tidal flat facies association. **A)** Rippled fine sandstone bedset with herringbone ripples (bottom portion) and climbing ripples (top portion), Sheep SWI, 29.4 m. **B)** Rose diagram showing bimodal flow directions in current ripples. **C)** Interference ripples on a bedding plane indicating multiple flow directions, Cottonwood Creek SW, 7.4 m. **D)** Ladderback ripples on a bedding plane, Alcova East SW, in float, ~ 5 m. **E)** Desiccation cracks superimposed on vortex ripples, Cottonwood Creek SW, 7.8 m. **F)** Vertical face showing the common association between rippled sand (Sr), massive sand (Sm), and planar laminated sand (Sp), Sheep SWH, 7 m.

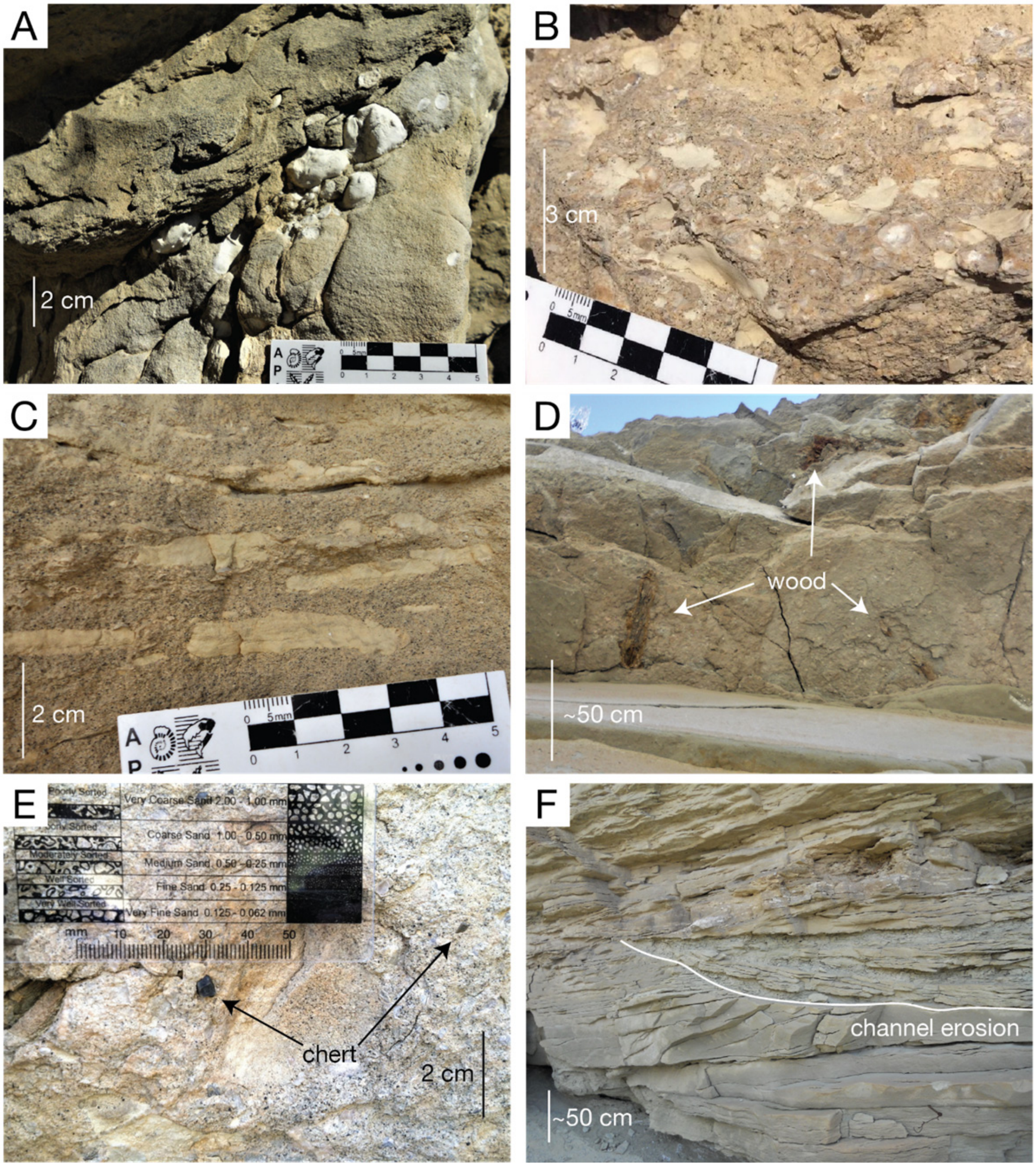

FIG. 3.8—Intraclasts and lag material observed in the shoreface and tidal flat facies associations. **A, B, C)** Sand intraclasts, Sheep SWI, 29.5 m (A), Sheep SWF, 25.7 m (B), Sheep SWH, 10.5 m (C). **D)** Large wood fragments on underside of bed, Pantosaurus SW, 10.2 m. **E)** Chert pebbles, Gypsum Spring Road SW, 6.5 m. **F)** Channel scale erosion and heterolithic fill, Sheep SWH, 10.2 m.

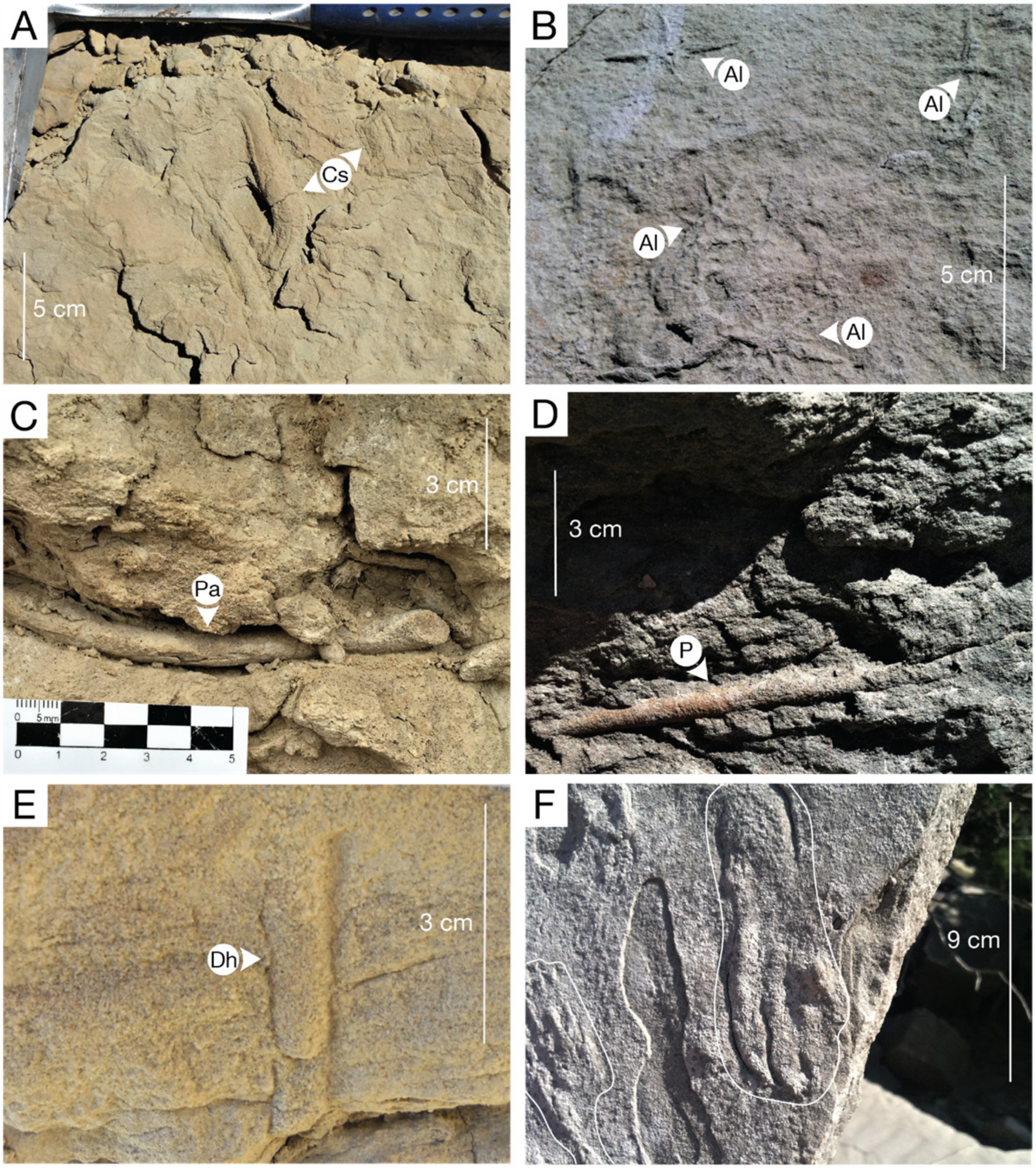

FIG. 3.9—Trace fossils observed in the study area. **A)** *Curvolithus simplex* (Cs), Camp Skeeter SW, 12 m. **B)** *Asteriacites lumbricalis* (Al), formed from ophiuroid trying to escape sedimentation event, Alcova East SW, in float, ~ 12 m. **C)** *Palaeophycus* (Pa), Red Dome SW, 14 m. **D)** *Planolites* (P), Newton Lakes SW, 1.5 m. **E)** *Diplocraterion habichi* (Dh) seen on a vertical face, Red Gulch SWA, 6 m. **F)** Pterosaur tracks on rippled bedding plane, Cottonwood Creek SW, 7.9 m.

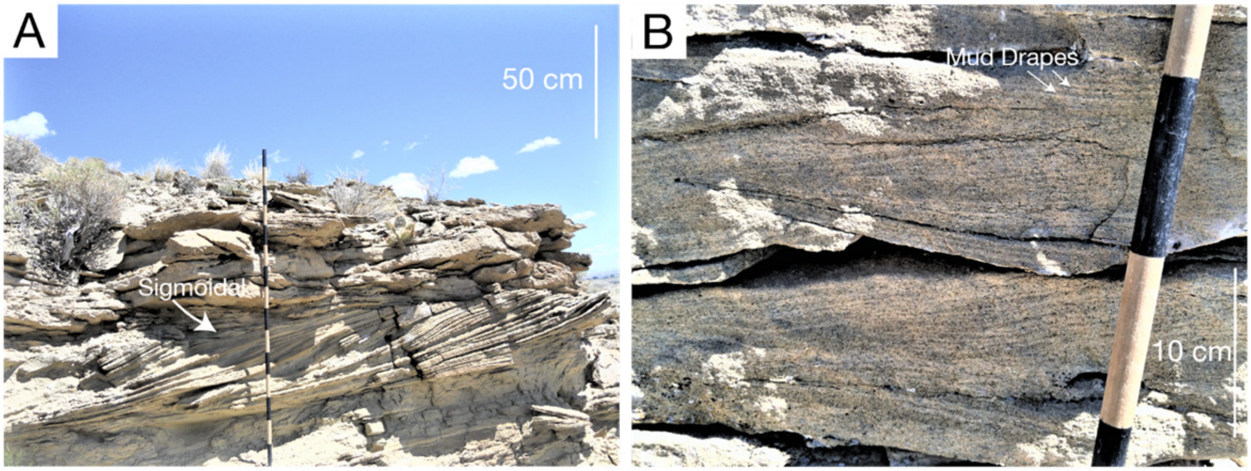

FIG. 3.10—Tidal structures observed in facies Sd-t of the tidal flat facies association. **A)** Sigmoidal cross-stratification, Sheep SWC, 8 m. **B)** Compound dunes with mud drapes, Newton Lakes SW, 14.7 m.

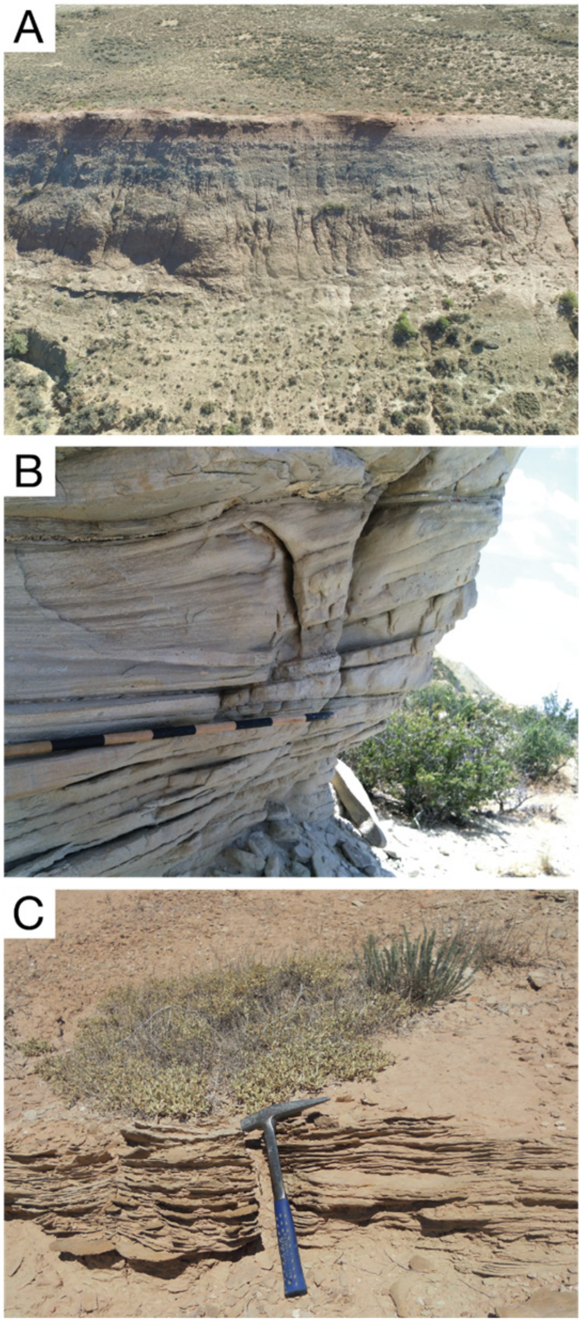

FIG. 3.11—Facies of the alluvial plain facies association. **A)** UAV image of floodplain facies Slt (tan, white, pink) in the Morrison Formation at Sheep Mountain SWA. **B)** Trough cross-stratified sandstone of facies Sd-a at Seminoe Dam SW, ~ 8 m. **C)** Fine grain sand of facies Sr-a and Sp-a in the Morrison Formation at Sheep Mountain SWA Drone, ~ 19 m.

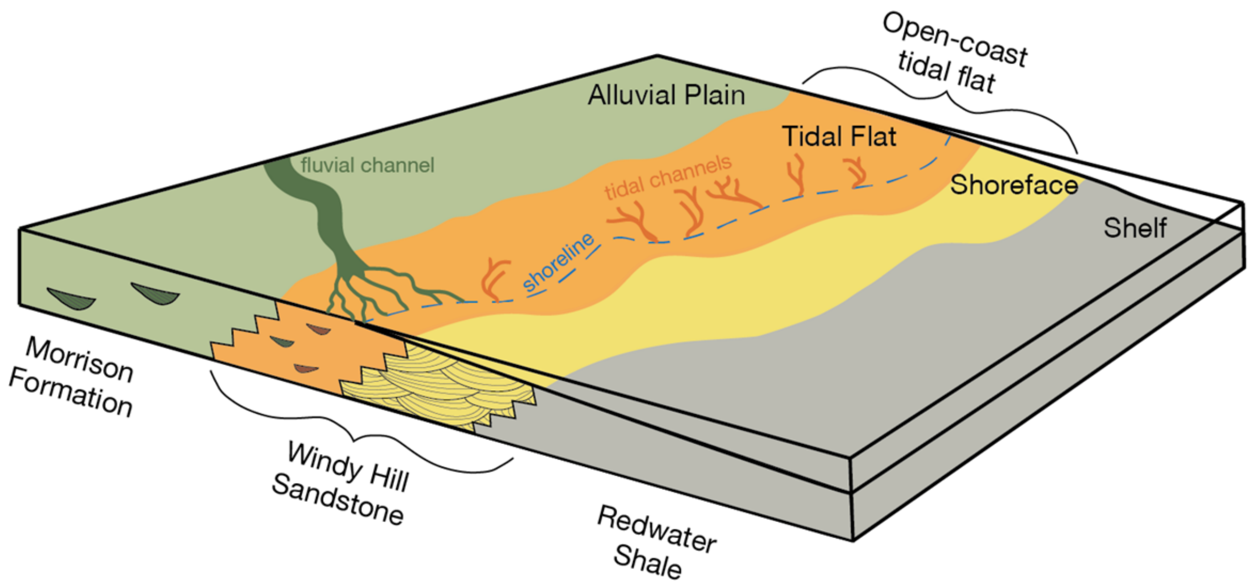

FIG. 3.12—Depositional model showing the relationship of facies associations in the Redwater Shale, Windy Hill Sandstone, and Morrison Formation. The shoreface facies association and the tidal flat facies association together make up an open-coast tidal flat.

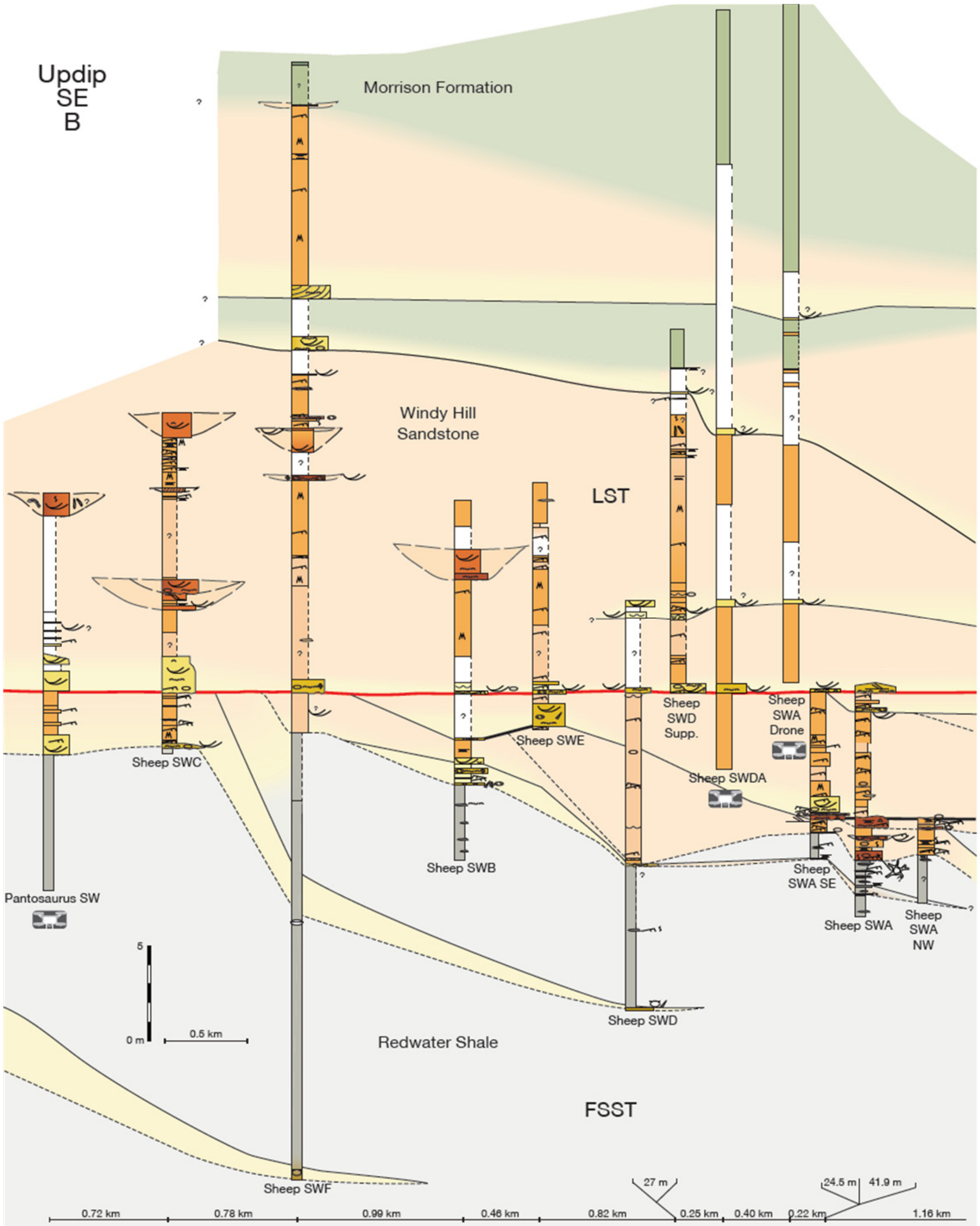

FIG. 3.13—Cross-section and sequence stratigraphic interpretation along depositional dip using closely spaced section from B to B'. See Fig. 3.15 for legend. Shading represents interpreted environments based on facies associations. Extra bold lines indicated contacts that were walked in the field or traced with drone video. FSST=falling-stage systems tract; LST=lowstand systems tract.

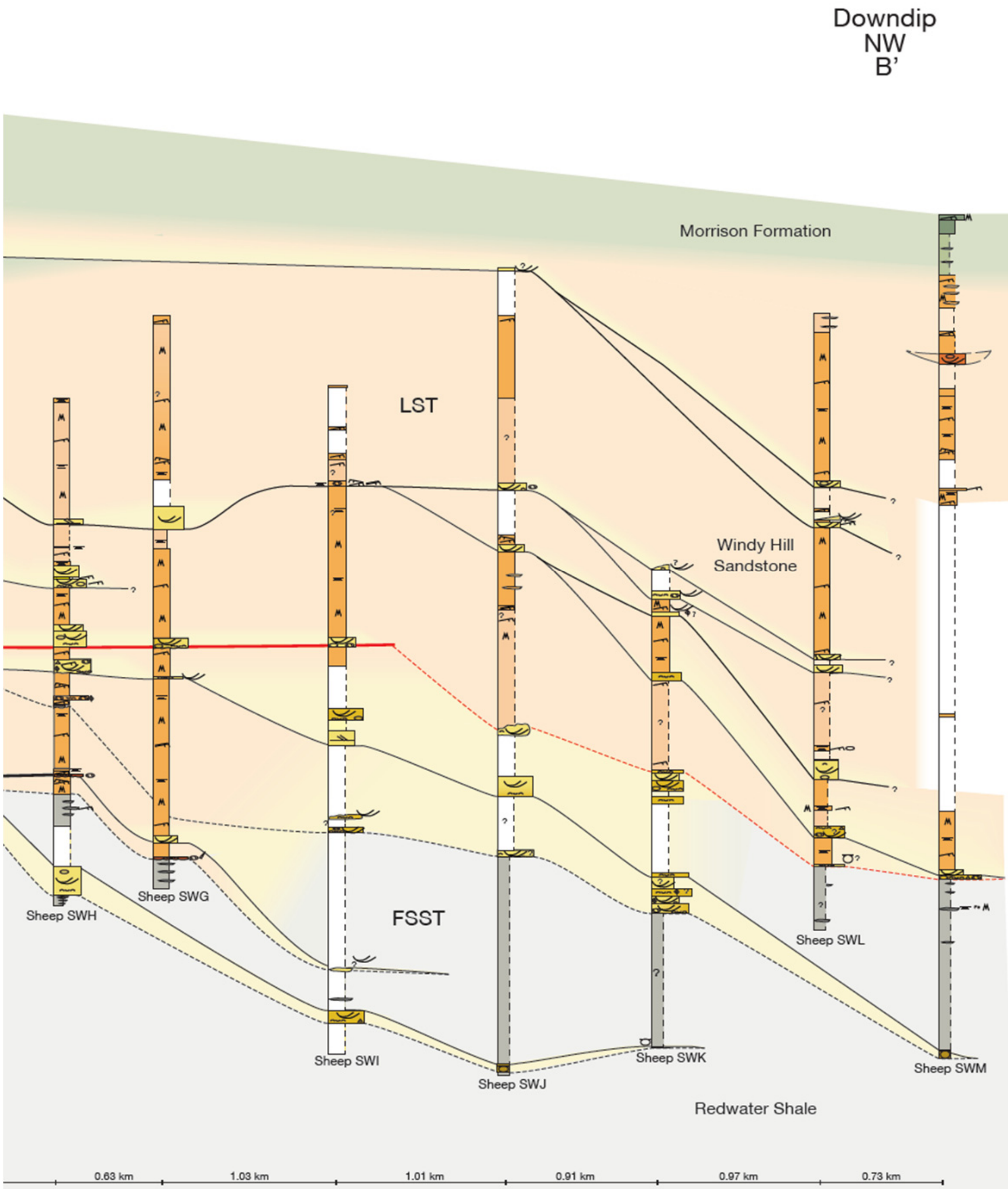

FIG. 3.13 continued.

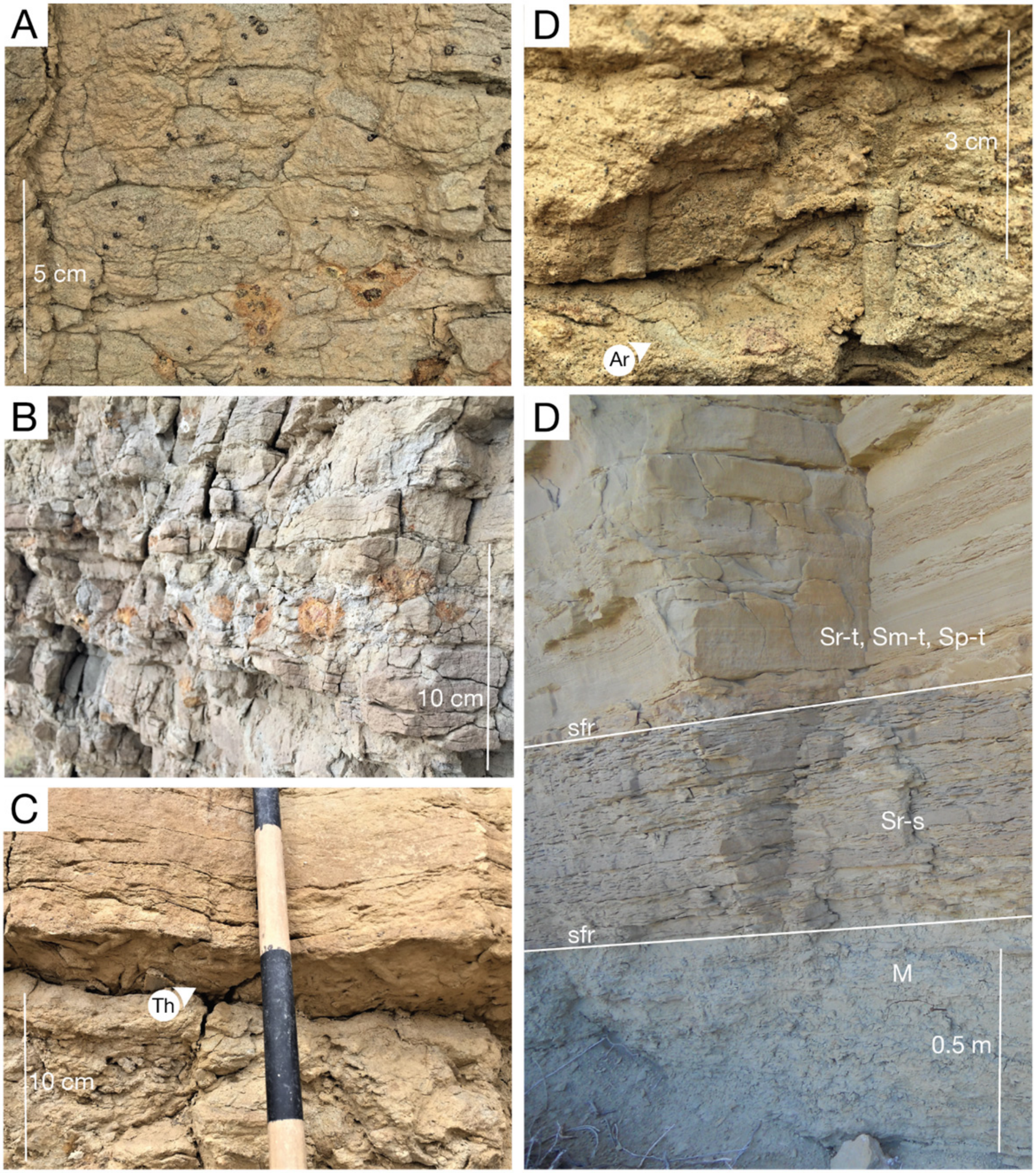

FIG. 3.14—Evidence of stratigraphic condensation and surfaces of forced regression. **A)** Abundant pyrite, Red Dome SW, 13–14 m. **B)** Iron staining on rock face Red Dome SW, 13–14 m. **C)** Trace fossil *Arencolites* (Ar) seen on a vertical face, Red Dome SW, 14 m. **D)** Trace fossil *Thalassinoides* (Th) seen on the sole of the lowest Windy Hill bed, Red Dome SW, 14.2 m. **E)** Telescoped section with two surfaces of forced regression (sfr) separating offshore (M), shoreface (Sr-s), and tidal flat (Sr-t, Sm-t, Sp-t), Sheep SWH, ~5.5–7.5 m.

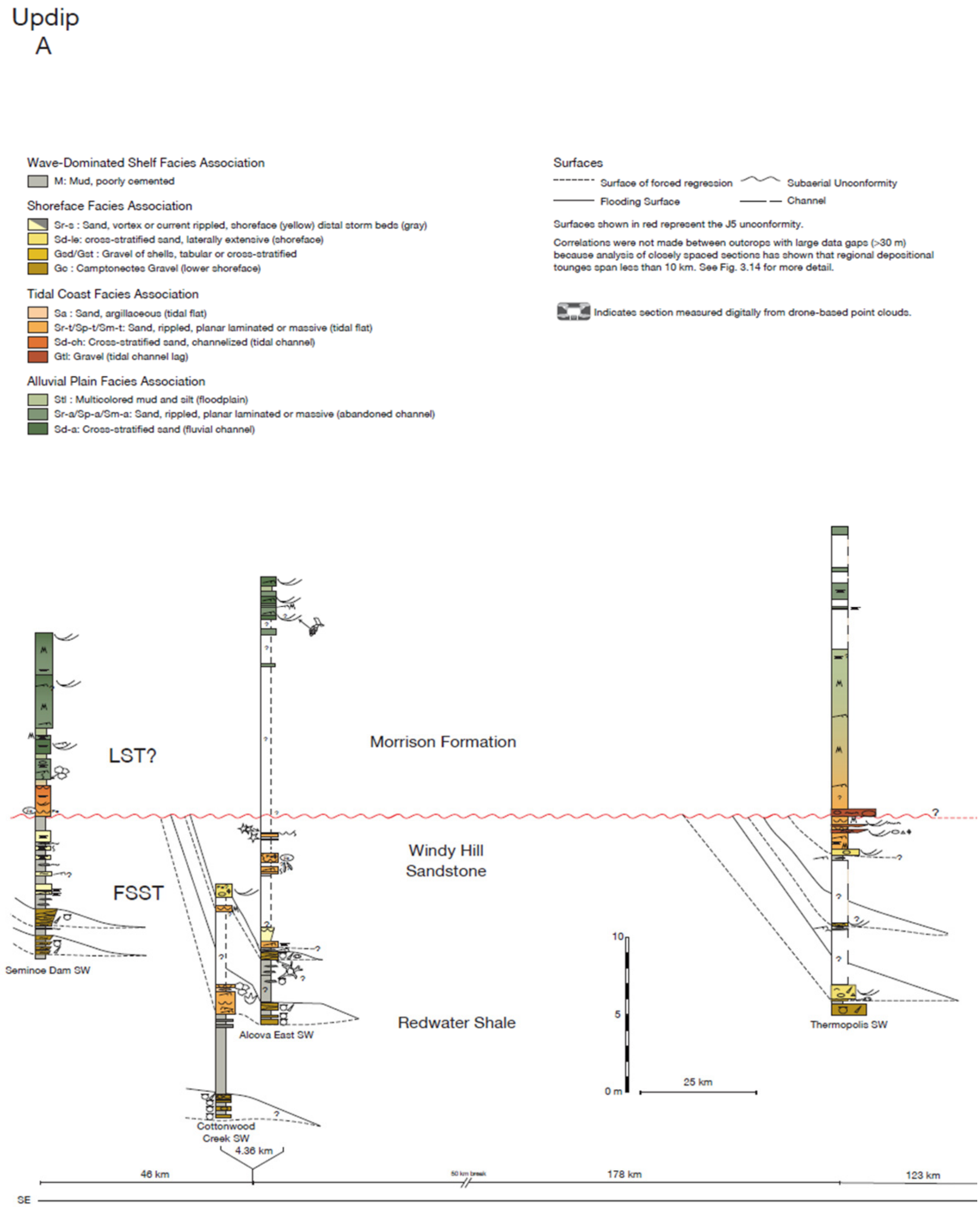

FIG. 3.15—Regional stratigraphic cross-section and sequence stratigraphic interpretation constructed along depositional dip from A to A'. The sequence bounding unconformity is the only surface that can be reasonably regionally correlated. HST=highstand systems tract; FSST=falling-stage systems tract; LST=lowstand systems tract.

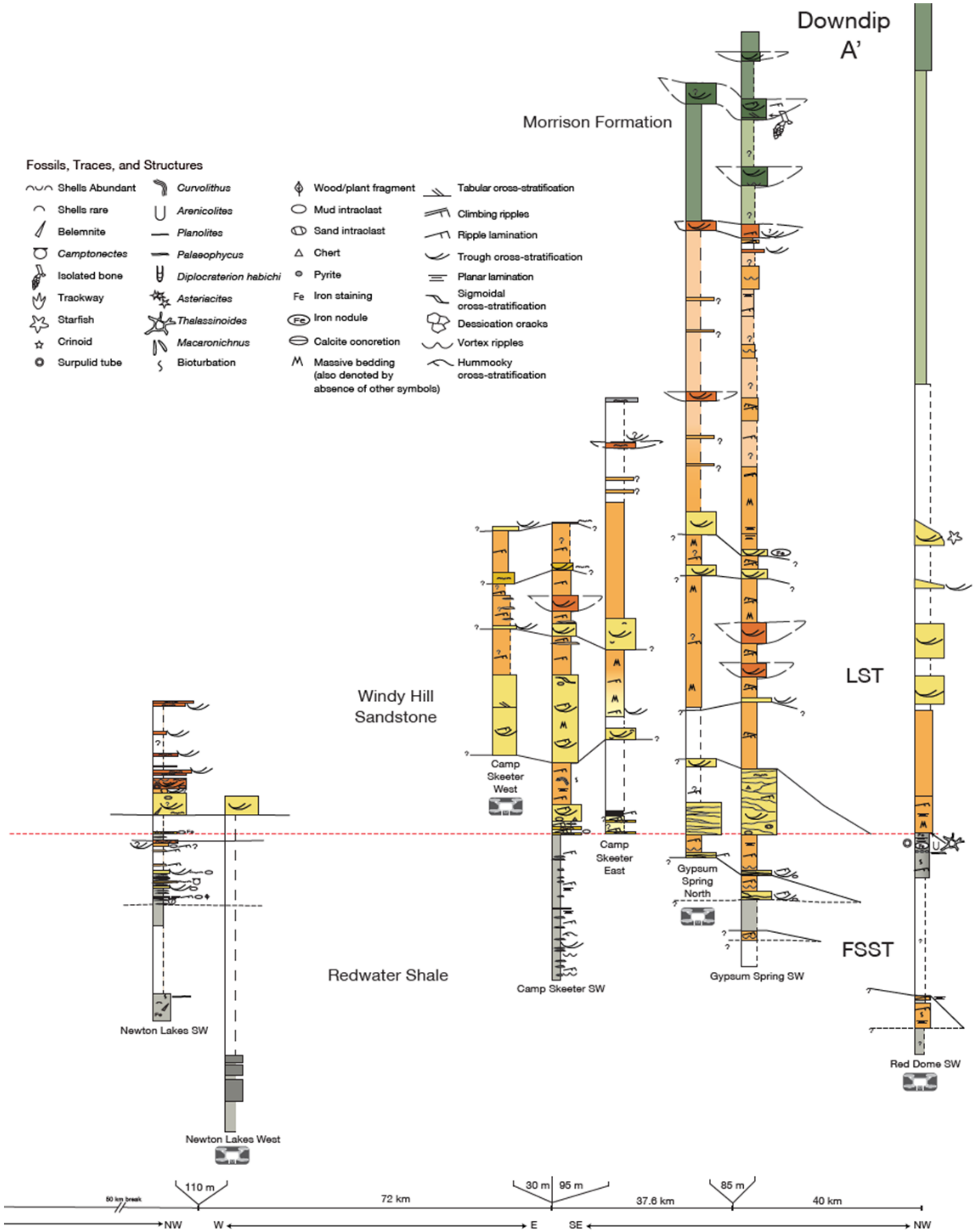

FIG 3.15 continued.

FIG. 3.16—Potential sequence-bounding unconformity. **A)** Sharp contact between the Windy Hill Sandstone and Morrison Formation at Thermopolis SW. **B)** Large rip-up clast at the Windy Hill-Morrison contact, Thermopolis SW, 13 m.

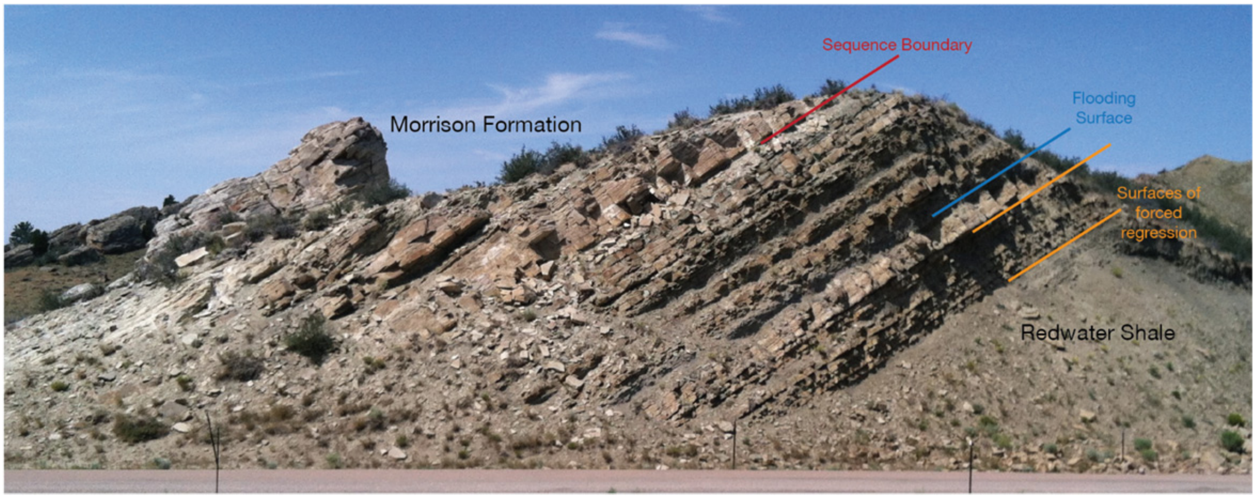

FIG. 3.17—Telescoped section with interpreted surfaces at Seminoe Dam SW. Surfaces of forced regression (orange) and a sequence boundary (red) are observed. The sequence boundary is marked by a distinct change in facies and depositional style from the wave-dominated shelf facies association to the tidal flat facies association.

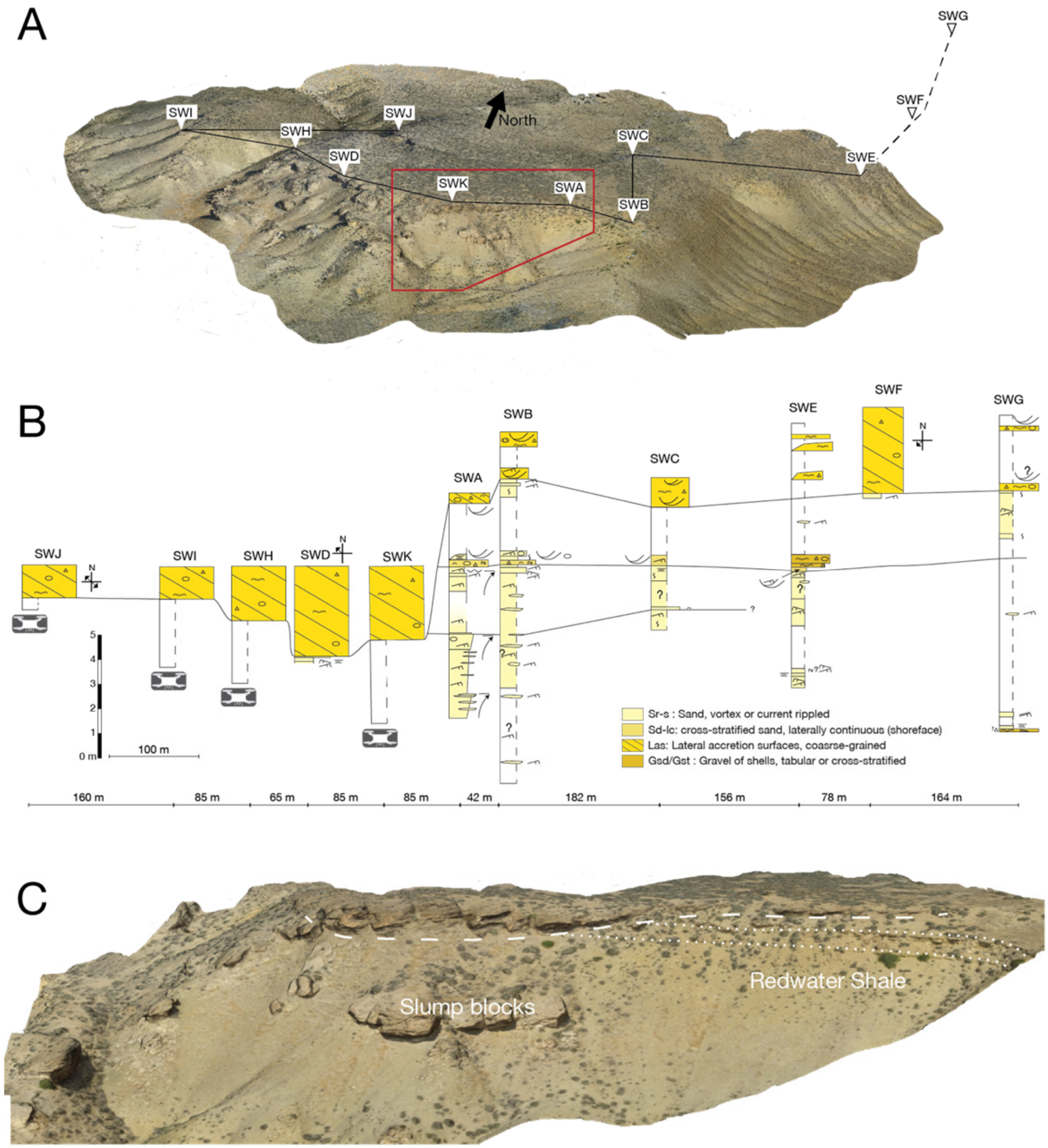

FIG. 3.18—Incision observed at Red Gulch. **A)** Point cloud constructed from drone imagery showing the locations of measured columns in panel B. Red outline shows the location of the point cloud in panel C. **B)** Measured columns from Red Gulch showing incision of ~ 5 m and truncation of beds in the Redwater Shale. See Fig. 3.15 for symbol key. Progradational stacking is denoted with arrows on column SWA. **C)** Point cloud between sections SWD and SWA showing incision consistent with tidal-channel erosion (white dashed line) and truncation of parasequence tops (white dotted lines). Note lateral accretion surfaces dipping to the left above the incision surface.

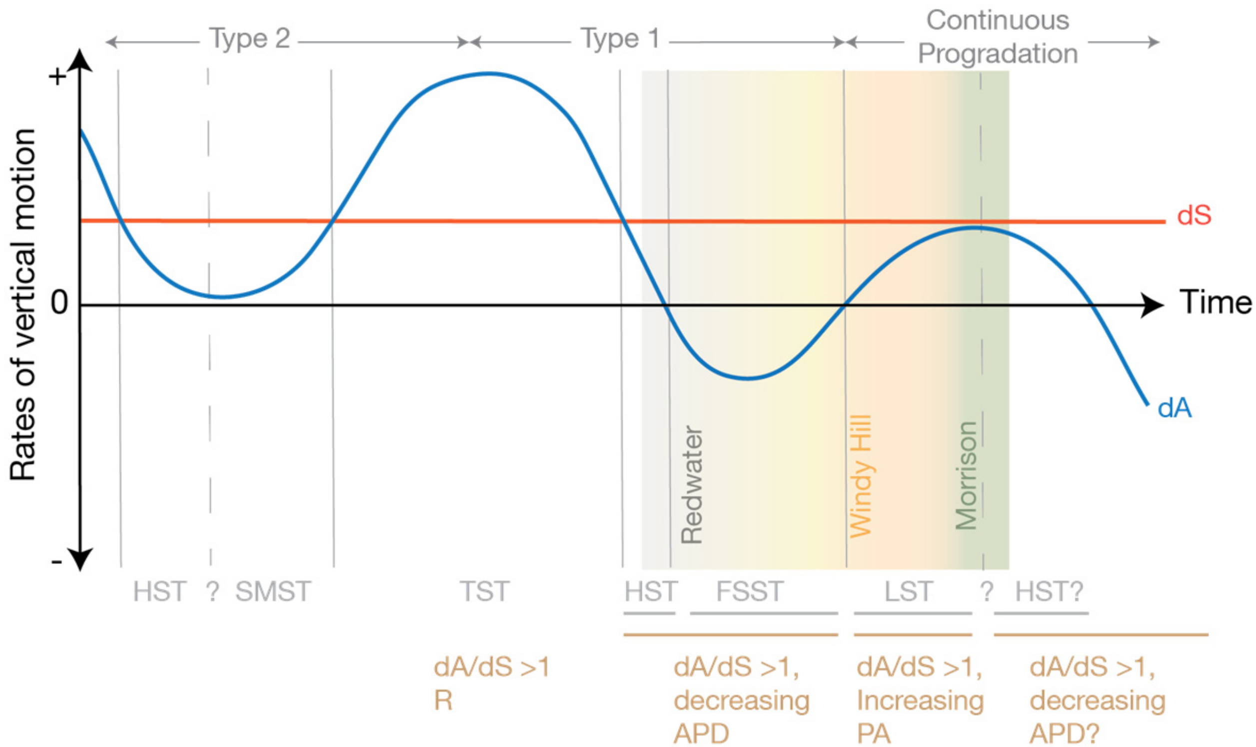

FIG. 3.19—Plot of hypothetical accommodation and sedimentation rates. Type 1 (after Hunt and Tucker 1992) and Type 2 (after Posamentier and Vail 1988) are shown for comparison, and the accommodation succession δA/δS ratios and stacking patterns are labeled in brown (Neal and Abreu 2009). RW=Redwater Shale, WH=Windy Hill Sandstone, MS=Morrison Formation, HST=highstand systems tract, SMST=shelf margin systems tract, TST=transgressive systems tract, FSST=falling-stage systems tract, LST=lowstand systems tract, R=retrogradational, APD=aggradational to progradational to degradational, PA=progradational to aggradational.

CHAPTER 4

CONCLUSIONS

The growing availability of UAV technology has opened new avenues for data collection and analysis in the geosciences. This study showed that UAV-based methods are an effective way to digitally measure stratigraphic columns to minimize data gaps that may result in incorrect correlations of stratigraphic surfaces. The workflow presented in this thesis was applied at outcrops of the Late Jurassic Redwater Shale, Windy Hill Sandstone, and basal Morrison Formation in Wyoming and southern Montana, and greatly assisted in the acquisition of data that would not have been previously available owing to topographic inaccessibility. These additional columns, as well as the ability to view outcrops from above, allowed for a re-evaluation of previous interpretations of the depositional environment and the nature of the basal contact of the Windy Hill Sandstone.

The Redwater Shale, Windy Hill Sandstone, and Lower Morrison Formation preserve portions of four systems tracts composing parts of two third-order depositional sequences. Portions of the highstand systems tract are recognized in the upper Redwater Shale as locally developed progradationally stacked parasequences. Surfaces of forced regression that are characteristic of the falling-stage systems tract are present in the upper Redwater Shale and the Windy Hill Sandstone. An unconformity roughly equivalent to the previously defined J5 sequence boundary is manifested as a subaerial exposure surface at the most updip localities, but is identified as the last surface of forced regression downdip. This means that the J5 is higher in the section than previously thought and that it is not always represented by the contact between the Redwater Shale and Windy Hill Sandstone. The lowstand systems tract is recognized by the progradation of the Morrison Formation over the Windy Hill Sandstone and by its stratigraphic position relative to the falling-stage systems tract. The Lower Morrison Formation is also interpreted as lowstand, but these deposits exhibit continuous progradation and may be an example of a depositional sequence lacking a transgressive systems tract, caused by low rates of accommodation. This illustrates the importance of considering the effect variable tectonics may have on the manifestation of depositional sequences in the rock record.

This study has led to several conclusions regarding the importance of scale in resolving issues related to using lithostratigraphic names for sequence stratigraphic purposes. The Redwater Shale, Windy Hill Sandstone, and Morrison Formation are all lithostratigraphic units that were grouped based on physical appearance. While practical for geologic mapping, lithostratigraphy can be misleading when a sequence stratigraphic understanding is the main goal. Grouping rocks by gross lithology leads also to a spatial separation of them, with the Windy Hill Sandstone always being the first sandstone above the Redwater Shale. This artificially creates a sharp contact with a jump in facies that is regionally extensive, leading to the interpretation of a sequence boundary where one does not exist and separating environments that existed on a spectrum into temporally distinct phases. There are three ways in which considering the scale of features and measurements can alter these interpretations.

The first consideration with regards to scale is the scale at which a depositional environment is expected to exist. This is the case of the Windy Hill Sandstone, where an interpretation based exclusively on the lithostratigraphic names and correlations implies an estuary that is over 360 km long and 150 km wide. This is large even when compared to the largest estuaries today, such as the Patos Lagoon in Brazil, which is about 250 km long and 50 km wide. Additionally, estuaries should show facies variation along their length from variations in marine influence, sediment supply, and water depth. This is inconsistent with observations of the Windy Hill Sandstone where similar facies are observed across Wyoming, making a single estuary an unlikely interpretation. A similar argument could perhaps be made with regards to the open-coast tidal flat interpretation presented in the previous chapter, although shorefaces are accepted as being more laterally extensive than an enclosed environment such as an estuary. Modern open-coast tidal flats are found in areas with a high mesotidal to macrotidal range (Alexander et al. 1991; Park et al. 1995; Yang et al. 2005). Tidal range could influence the areal extent of a depositional environment, as could the geometry of the seaway or coastal gradient where open-coast tidal flats are observed. The closest modern analog to the Sundance Seaway is the Yellow Sea that borders China and

Korea, where open-coast tidal flats are well documented. Like the Yellow Sea, the Sundance Seaway is thought to have been rather shallow, with a long and narrow geometry possibly extending north nearly 2000 km (Blakey 2014). This geometry may have resulted in an amplified tidal influence similar to the macrotidal Yellow Sea, which would have favored extensive tidal flats, but further investigation of tidal amplitude in the Sundance Seaway is necessary to test this.

The concept of scale is also critical in the design of a study and the analysis of its results. In design, outcrops must be spaced such that contacts can be correlated correctly. This is often not possible, but knowledge gained from just a few closely spaced sections should be applied on a more regional level. Even a single column can contain features or surfaces that can greatly assist in correlations. If surfaces of forced regression, for example, can first be recognized in a single section, then the framework is better understood and can be used as the correlation process progresses, yielding results that are more likely to be closer to the actual solution. Without the initial identification of these surfaces, however, it is possible to mistakenly correlate these discontinuities as a single surface, rather than recognizing them as temporally distinct.

This study used UAV-based imagery to construct point clouds. This proved to be an effective way to supplement data between measured sections, measure geographically inaccessible sections, characterize bedding geometry and depth of incision, and trace contacts laterally between outcrops. Although processing time is required to use UAV-based methods, these methods allow columns to be measured at localities that were previously inaccessible. This allows several columns to be measured from one point cloud, decreasing the size of data gaps. Achieving such a small outcrop spacing in the field would be time-consuming, and would not capture the correlations among the columns visible in the point cloud. The UAV-based methods presented here allow for greater repeatability and consistency of column measurement, as well as estimates of uncertainty in those measurements, something that is prohibitively time-consuming in the field. Point clouds are also easily shared among collaborators and can be reinterpreted in the lab. Development of UAV-based methods should continue, with an emphasis on quantifying uncertainty and maximizing data coverage.

REFERENCES

AINSWORTH, R.B., VAKARELOV, B.K., LEE, C., MACEACHERN, J.A., MONTGOMERY, A.E., RICCI, L.P., and DASHTGARD, S.E., 2015, Architecture and evolution of a regressive, tide-influenced marginial marine succession, Drumheller, Alberta, Canada: Journal of Sedimentary Research, v. 85, p. 596–625.

ALEXANDER, C.R., NITTROUER, C.A., DEMASTER, D.J., PARK, Y.A., and PARK, S.C., 1991, Macrotidal mudflats of the southwestern Korean coast: A model for interpretation of intertidal deposits: Journal of Sedimentary Petrology, v. 61, p. 805–824.

ASHLEY, G.M., 1990, Classification of large-scale subaqueous bedforms; a new look at an old problem: Journal of Sedimentary Petrology, v. 60, p. 160–172.

BERGMAN, K.M., and WALKER, R.G., 1999, Campanian Shannon Sandstone: An example of falling stage systems tract deposits *in* Bergman, K.M., and Snedden, J.W., eds., Isolated Shallow Marine Sand Bodies: Sequence Stratigraphic Analysis and Sedimentologic Interpretation: SEPM Special Publication 64, 362 p.

BERNER, R.A., 1981, A new geochemical classification of sedimentary environments: Journal of Sedimentary Petrology, v. 51, p. 359–365.

BJERRUM, C.J., and DORSEY, R.J., 1995, Tectonic controls on deposition of Middle Jurassic strata in a retroarc foreland basin, Utah–Idaho trough, western interior, United States: Tectonics, v. 14, p. 962–978.

BLAKE, D.B., and GUENSBERG, T.E., 2016, An asteroid (Echinodermata) faunule from the Oxfordian Swift Formation (Upper Jurassic) of Montana: Journal of Paleontology, v. 90, p. 1160–1168.

BLAKEY, R.C., 2014, Paleogreography and paleotectonics of the Western Interior Seaway, Jurassic-Cretaceous of North America: AAPG Search and Discovery Article, 30392.

BOYD, R., DALRYMPLE, R.W., and ZAITLIN, B.A., 1992, Classification of clastic coastal depositional environments: Sedimentary Geology, v. 80, p. 139–150.

BOYD, R., DIESSEL, C.F.K., WADSWORTH, J., LECKIE, D., and ZAITLIN, B.A., 2000, Development of a non-marine sequence stratigraphic model *in* Boyd R., Diessel, C.F.K., Francis, S., eds., Advances in the study of the Sydney Basin: Proceedings of the 34th Newcastle Symposium, University of Newcastle, p. 1–14.

BRENNER, R.L., and DAVIES, D.K., 1973, Storm-generated coquinoid sandstone: Genesis of high-energy marine sediments from the Upper Jurassic of Wyoming and Montana: Geological Society of America Bulletin, v. 84, p. 1685–1697.

BRENNER, R.L., and DAVIES, D.K., 1974a, Oxfordian sedimentation in Western Interior United States: AAPG Bulletin, v. 58, p. 407–428.

BRENNER, R.L., and DAVIES, D.K., 1974b, Storm-generated coquinoid sandstone: Genesis of high-energy marine sediments from the Upper Jurassic of Wyoming and Montana: Reply: Geological Society of America Bulletin, v. 85, p. 838.

BRENNER, R.L., and PETERSON, J.A., 1994, Jurassic sedimentary history of the northern portion of the Western Interior Seaway, USA, *in* Caputo, M.V., Peterson, J.A., and Franczyk, K.J., eds., Mesozoic Systems of the Rocky Mountain Region, USA: SEPM, Rocky Mountain Section, p. 217–232.

BRUUN, P., 1962, Sea-level rise as a cause of shore erosion: Proceeedings of the American Society of Civil Engineers, v. 88, p. 117–130.

BUATOIS, L., and MÁNGANO, M.G., 2011, Ichnology: Organsism-substrate interactions in space and time: Cambridge, Cambridge University Press, 358 p.

BURTON, D., FLAIG, P.P., and PRATHER, T.J., 2016, Regional controls on depositional trends in tidally modified deltas: Insights from sequence stratigraphic correlation and mapping of the Loyd and Sego Sandstones, Uinta and Piceance Basins of Utah and Colorado, U.S.A.: Journal of Sedimentary Research, v. 86, p. 763–785.

CALLOMON, J.H., 1984, A review of the biostratigraphy of the post-lower Bajocian Jurassic ammonites of western and northern North America, *in* Westermann, G.E.G., ed., Jurassic–Cretaceous Biochronology and Paleogeography of North America: Geological Association of Canada, Special Paper 27, p. 143–174.

CARRIVICK, J.L., SMITH, M.W., QUINCEY, D.J., and CARVER, S.J., 2013, Developments in budget remote sensing for the geosciences: Geology Today, v. 29, p. 138–143.

CATTANEO, A., and STEEL, R.J., 2003, Transgressive deposits: A review of their variability: Earth-Science Reviews, v. 62, p. 187–228

CATUNEANU, O., 2006, Principles of Sequence Stratigraphy: Boston, Elsevier, 375 p.

CHENTNIK, B.M., JOHNSON, C.L., MULHERN, J.S., and STRIGHT, L., 2015, Valleys, estuaries, and lagoons: Paleoenvironments and regressive-transgressive architecture of the Upper Cretaceous Straight Cliffs Formation, Utah, U.S.A.: Journal of Sedimentary Research, v. 85, p. 1166–1196.

CHESLEY, J.T., LEIER, A.L., WHITE, S., and TORRES, R., 2017, Using unmanned aerial vehicles and structure-from-motion photogrammetry to characterize sedimentary outcrops: An example from the Morrison Formation, Utah, USA: Sedimentary Geology, v. 354, p. 1–8.

CLEMENT, A.M., and HOLLAND, S.M., 2016, Sequence stratigraphic context of extensive basin-margin evaporites: Middle Jurassic Gypsum Spring Formation, Wyoming, U.S.A.: Journal of Sedimentary Research, v. 86, p. 965–981.

CLIFTON, H.E., 2006, A reexamination of facies models for clastic shorelines, *in* Posamentier, H.W., and Walker, R.G., Facies Models Revistited: SEPM Special Publication 84, p. 293–337.

CLIFTON, H.E., HUNTER, R.E., and PHILLIPS, R.L., 1971, Depositional structures and processes in the high energy non-barred nearshore: Journal of Sedimentary Petrology, v. 40, p. 651–670.

CONNELY, M.V., 2006, Paleoecology of pterosaur tracks from the Upper Sundance and Lower Morrison Formations in central Wyoming: New Mexico Museum of Natural History and Science Bulletin, v. 36, p. 199–202.

CROWLEY, P.H., 1992, Resampling methods for computation-intensive data analysis in ecology and evolution: Annual Review of Ecology and Systematics, v. 23, p. 405–447.

DALRYMPLE, R.W., 2010, Tidal depositional systems *in* James, N.P, and Dalrymple, R.W., eds., Facies Models 4: Vancouver , Geological Association of Canada, p. 201–231.

DALRYMPLE, R.W., ZAITLIN, B.A., and BOYD, R., 1992, Estuarine facies models: Conceptual basis and stratigraphic implications: Journal of Sedimentary Petrology, v. 62, p. 1130–1147.

DASHTGARD, S.E., GINGRAS, M.K., and MACEACHERN, J.A., 2009, Tidally modulated shorefaces: Journal of Sedimentary Research, v. 79, p. 793–807.

DANISE, S., and HOLLAND, S.M., 2017, Faunal response to sea-level and climate change in a short-lived seaway: Jurassic of the Western Interior, USA: Palaeontology, v. 60, p. 1–20.

DUMAS, S., ARNOTT, R.W.C., and SOUTHARD, J.B., 2005, Experiments on oscillatory-flow and combined-flow bed forms: Implications for interpreting parts of the shallow-marine sedimentary record: Journal of Sedimentary Research, v. 75, p. 501–513.

DEMKO, T.N, CURRIE, B.S., and NICOLL, K.A., 2004, Regional paleoclimatic and stratigraphic implications of paleosols and fluvial/overbank architecture in the Morrison Formation (Upper Jurassic), Western Interior, USA: Sedimentary Geology, v. 167, p. 115–135.

DESJARDINS, P.R., BUATOIS, L.A., PRATT, B.R., and MÁNGANO, M.G., 2012, Forced regressive tidal flats: response to falling sea level in tide-dominated settings: Journal of Sedimentary Research, v. 82, p. 149–162.

FAN, D., 2012, Open-coast tidal flats *in* Davis, R.A., Jr, and Dalrymple, R.W., eds., Principles of Tidal Sedimentology: New York, Springer, p. 187–229.

FERNÁNDEZ, O., 2005, Obtaining a best fitting plane through 3D georeferenced data: Journal of Structural Geology, v. 27, p. 855–858.

FIELDING, C.R., HUTSKY, A.J., and HURD, T.J., 2014, Deltaic deposits formed under spatially and temporally variable accommodation regimes: A plausible alternative explaination for isolated shallow-marine sandstone bodies: AAPG Bulletin, v. 98, p. 893–909.

FISCHLER, M.A., and BOLLES, R.C., 1981, Random sample concensus: A paradigm for model fitting with applications to image analysis and automated cartography: Communications of the ACM, v. 24, p. 381–395.

FÜRSICH, F.T., and HEINBERGE, C., 1983, Sedimentology, biostratinomy, and paleoecology of an Upper Jurassic offshore bar complex: Bulletin of the Geologic Society of Denmark, v. 32, p. 67–95.

GARCÍA-SELLÉS, D., FALIVENE, O., ARBUÉS, P., GRATACOS, O., TAVANI, S., and MUÑOZ, J.A., 2011, Supervised identification and reconstruction of near-planar geological surfaces from terrestrial laser scanning: Computers and Geoscienes, v. 37, p. 1584–1594.

GINN, C.L., 2014, Sequence stratigraphy of the Silurian Clinch Formation, northeastern Tennessee and southwestern Virginia [M.S. thesis]: Univeristy of Georgia, Athens, Georgia, 75 p.

GUILBERT, J.M., and PARK, C.F., 1986, Epigenetic deposits of doubtful igneous connection, *in* Guilbert, J.M., and Park, C.F., eds., The Geology of Ore Deposits: New York, W.H. Freeman and Company, p. 886–934.

GUNDERSON, J.A., 2015, Asteroid fossils from the Upper Jurassic of south-central Montana: Montana Bureau of Mines and Geology Open-File Report 660, 10 p.

HUNT, D., and TUCKER, M.E., 1992, Stranded parasequences and the forced regressive wedge systems tract: deposition during base-level fall: Sedimentary Geology, v. 81, p. 1–9.

HUTSKY, A.J., and FIELDING, C.R., 2016, The offshore bar revisited: A new depositional model for isolated shallow marine sandstones in the Cretaceous Frontier Formation of the northern Uinta Basin, Utah, U.S.A.: Journal of Sedimentary Research, v. 86, p. 38–58.

IMLAY, R.W., 1956, Marine Jurassic exposed in Bighorn Basin, Pryor Mountains, and northern Bighorn Mountains, Wyoming and Montana: Bulletin of the American Association of Petroleum Geologists, v. 40, p. 562–599.

IMLAY, R.W., 1980, Jurassic paleobiogeography of the conterminous United States in its continental setting: U.S. Geological Survey Professional Paper 1062, 134 p.

IMLAY, R.W., 1982, Jurassic (Oxfordian and late Callovian) ammonites from the Western Interior region of the United States: U.S. Geological Survey Professional Paper 1232, 44 p.

JOHNSON, E.A., 1992, Depositional history of Jurassic rocks in the area of the Powder River basin, northeastern Wyoming and southeastern Montana: United States, U. S. Geological Survey Bulletin 1917-J, 48 p.

JO, J., and CHOI, K., 2016, Morphodynamic and hydrodynamic controls on the stratigraphic architecture of intertidal compound dunes on the open-coast macrotidal flat in the northern Gyeonggi Bay, west coast of Korea: Journal of Sedimentary Research, v. 86, p. 1103–1122.

JORDAN, B.R., 2015, A bird's-eye view of geology: The use of micro drones/UAVs in geologic fieldwork and education: GSA Today, v. 25, p. 50–52.

JORDAN, O.D., GUPTA, S., HAMPSON, G.J., and JOHNSON, H.D., 2016, Preserved stratigraphic architecture and evolution of a net-transgressive mixed wave- and tide-influenced coastal system: The Cliff House Sandstone, Northwestern New Mexico, U.S.A.: Journal of Sedimentary Research, v. 86, p. 1399–1424.

KIDWELL, S.M., 1991, The stratigraphy of shell concentrations, *in* Allison, P.A., and Brings, D.E.G., eds., Taphonomy: Releasing the Data Locked in the Fossil Record: New York, Plenum, p. 211–290.

KOCUREK, G., and DOTT, R.H., 1983, Jurassic paleogeography and paleoclimate of the central and southern Rocky Mountains region, *in* Reynolds, M.W., and Dolly, E.D., eds., Mesozoic Paleogeography of the West-Central United States: SEPM Rocky Mountain Section, Denver, Colorado, p. 101–116.

KOWALLIS, B.J., CHRISTIANSEN, E.H., DEINO, A.L., PETERSON, F., TURNER, C.E., KUNK, M.J., and OBRADOVICH, J.D., 1998, The age of the Morrison Formation: Modern Geology, v.22, p. 235–260.

KVALE, E.P., and VONDRA, C.F., 1985, Upper Jurassic–Lower Cretaceous transitional marine and fluvial sediments in the Bighorn Basin, *in* Flores, R.M., and Harvey, M.D., eds., Field guidebook to modern and ancient fluvial systems in the United States: SEPM Third International Fluvial Sedimentology Conference, Fort Collins, Colorado, p. 33–44.

KVALE, E.P., JOHNSON, A.D., MICKELSON, D.L., KELLER, K., FURER, L.C., and ARCHER, A.W., 2001, Middle Jurassic (Bajocian and Bathonian) dinosaur megatracksites, Bighorn Basin, Wyoming, USA: Palaios, v. 16, p. 233–254.

LAWTON, T.F., 1994, Tectonic setting of Mesozoic sedimentary basins, Rocky Mountain region, United States, *in* Caputo, M.V., Peterson, J.A., and Franczyk, K.J., eds., Mesozoic Systems of the Rocky Mountain Region, USA: SEPM Rocky Mountain Section, p. 1–26.

LEE, K., MCMECHAN, G.A., GANI, M.R., BHATTACHARYA, J.P., ZENG, X., and HOWELL JR., C.D., 2007, 3-D architecture and sequence stratigraphic evolution of a forced regressive top-truncated mixed-influenced delta, Cretaceous Wall Creek Sandstone, Wyoming, U.S.A.: Journal of Sedimentary Research, v. 77, p. 303–323.

LEGLER, B., HAMPSON, G.J., JACKSON, C.,A.-L., JOHNSON, H.D., MASSART, B.Y.G., SARGINSON, M., and RAVNÅS, R., 2014, Facies relationships and stratigraphic architecture of distal, mixed tide- and wave-influenced deltaic deposits: Lower Sego Sandstone, Western Colorado, U.S.A.: Journal of Sedimentary Research, v. 84, p. 605–625.

LI, Y., and BHATTACHARYA, J.P., 2013, Facies-architecture study of a stepped, forced regressive compound incised valley in the Ferron Notom Delta, southern central Utah, U.S.A: Journal of Sedimentary Research, v. 83, p. 206–225.

LIM, D.I., and PARK, Y.A., 2003, Late Quaternary stratigraphy and evolution of a Korean tidal flat, Haenam Bay, southeastern Yellow Sea, Korea: Marine Geology, v. 193, p. 177–194.

LIU, S.F., NUMMENDAL, D., and LIU, L.J., 2011, Migration of dynamic subsidence across the Late Cretaceous United States Western Interior Basin in response to Farallon plate subduction: Geology, v. 39, p. 555–558.

LOCKLEY, M.G., and WRIGHT, J.L., 2003, Pterosaur swim tracks and other ichnological evidence of behaviour and ecology: Geological Society of London Special Publications, v. 217, p. 297–313.

LOGUE, T.J., 1977, Preliminary investigations of pterodactyl footprints at Alcova, Wyoming: Wyoming Geological Association, Earth Science Bulletin, v. 10, p. 29–30.

MACEACHERN, J.A., PEMBERTON, S.G., GINGRAS, M.K., and BANN, K.L., 2010, Ichnology and facies models *in* James, N.P., and Dalrymple, R.W., eds., Facies Models 4: Geological Association of Canada, p. 105–137.

MACHENT, P.G., TAYLOR, K.G., MACQUAKER, J.H.S, and MARSHALL, J.D., 2012, Distribution and petrography of concretionary carbonate in a falling-stage delta-front sandstone succession: Upper Cretaceous Pather Tongue Member, Book cliffs, Utah *in* Morad, S., Ketzer, J.M., and De Ros, L.F., eds., Linking Diagenesis to Sequence Stratigraphy: International Association of Sedimentologists, Special Publication 45, p. 183–206.

MARSHALL, J.D. and PIRRIE, D., 2013, Carbonate concretions; explained: Geology Today, v. 29, p. 53–62.

MASSELING, G. and SHORT, A.D., 1993, The effect of tide range on beach morphodynamics and morphology: a conceptual beach model: Journal of Coastal Research, v. 9, p. 785–800.

MAYNARD, J.B., 1982, Extension of Berner's "New geochemical classification of sedimentary environments" to ancient sediments: Journal of Sedimentary Petrology, v. 52, p. 1325–1331.

MCMULLEN, S.K., HOLLAND, S.M., and O'KEEFE, F.R., 2014, The occurrence of vertebrate and invertebrate fossils in a sequence stratigraphic context; the Jurassic Sundance Formation, Bighorn Basin, Wyoming, U.S.A: Palaios, v. 29, p. 277–294.

MELLERE, D., 1994, Sequential development of an estuarine valley fill: The Twowells Toungue of the Dakota Sandstone, Acoma Basin, New Mexico: Journal of Sedimentary Research, v. 64, p. 500–515.

MIALL, A.D., 2010, Alluvial deposits *in* James, N.P., and Dalrymple, R.W., eds., Facies Models 4: Vancouver, Geological Association of Canada, p. 105–137.

MIRSKY, A., 1962, Stratigraphy of non-marine Upper Jurassic and Lower Cretaceous rocks, southern Bighorn Mountains, Wyoming: AAPG Bulletin, v. 46, p. 1653–1680.

MOBERLY, R., JR., 1960, Morrison, Cloverly, and Sykes Mountain Formations, northern Bighorn Basin, Wyoming and Montana: Geological Society of America Bulletin, v. 71, p. 1137–1176.

NEAL, J.E., and ABREU, V., 2009, Sequence stratigraphy hierarchy and the accommodation succession method: Geology, v. 37, p. 779–782.

NEAL, J.E., ABREU, V., BOHACS, K.M., FELDMAN, H.R., and PEDERSON, K.H., 2016, Accommodation succession ($\delta A/\delta S$) sequence stratigraphy: Observational method, utility and insights into sequence boundary formation: Journal of the Geological Society, v. 173, p. 803–816.

NIEMINSKI, N.M., and GRAHAM, S.A., 2017, Modeling stratigraphic architecture using small unmanned aerial vehicles and photogrammetry: Examples from the Miocene East Coast Basin, New Zealand: Journal of Sedimentary Research, v. 87, p. 126–132.

PARK, Y.A., WELLS, J.T., KIM, B.W., and ALEXANDER, C.R., 1995, Tidal lamination and facies development in the macrotidal flats of Namyang Bay, west coast Korea: Special Publication of the International Association of Sedimentologists, v. 24, p. 183–191.

PARK, Y.A., LIM, D.I., KHIM, B.K., CHOI, J.Y., and DOH, S.J., 1998, Stratigraphy and subaerial exposure of Late Quaternary tidal deposits in Haenam Bay, Korea: Estuarine, Coastal and Shelf Science, v. 47, p. 523–533.

PARRISH, J.T., and PETERSON, F., 1988, Wind directions predicted from global circulation models and wind directions determined from eolian sandstones of the western United States—A comparison: Sedimentary Geology, v. 56, p. 261–282.

PETERSON, F., 1994, Sand dunes, sabkhas, streams, and shallow seas: Jurassic paleogeography in the southern part of the Western Interior Basin, *in* Caputo, M.V., Peterson, J.A., and Franczyk, K.J., eds., Mesozoic Systems of the Rocky Mountain Region, USA: SEPM Rocky Mountain Section, p. 233–272.

PHELPS, R.M., KERANS, C., SCOTT, S.Z., JANSON, X., and BELLIAN, J.A., 2008, Three-dimensional modelling and sequence stratigraphy of a carbonate ramp-to-shelf transition, Permian Upper San Andres Formation: Sedimentology, v. 55, p. 1777–1813.

PIPIRINGOS, G.N., 1968, Correlation and nomenclature of some Triassic and Jurassic rocks in south-central Wyoming: United States, U. S. Geological Survey Professional Paper 594-D, 32 p.

PIPIRINGOS, G.N., and O'SULLIVAN, R.B., 1978, Principal unconformities in Triassic and Jurassic rocks, Western Interior United States; a preliminary survey: U. S. Geological Survey Professional Paper 1035-A, 26 p.

PLINT, A.G., 2010, Wave- and storm-dominated shoreline and shallow marine systems *in* James, N.P., and Dalrymple, R.W., eds., Facies Models 4: Vancouver, Geological Association of Canada, p. 167–199.

PLINT, A.G., and WADSWORTH, J.A., 2003, Sedimentology and palaeogeomorphology of four large valley systems incising delta plains, western Canada Foreland Basin: Implications for mid-Cretaceous sea-level changes: Sedimentology, v. 50, p. 1147–1186.

PONTÉN, A., and PLINK-BJÖRKLUND, P., 2009, Process regime changes across a regressive to transgressive turnaround in a shelf-slope basin, Eocene Central Basin of Spitsbergen: Journal of Sedimentary Research, v. 79, p. 2–23.

POSAMENTIER, H.W., and ALLEN, G.P., 1999, Siliciclastic sequence stratigraphy: concepts and applications, SEPM Concepts in Sedimentology and Paleontology, No. 7, 210 p.

POSAMENTIER, H.W., and VAIL, P.R., 1988, Eustatic controls on clastic deposition II—sequences and systems tract models *in* Wilgus, C.K., Hastings, B.S., Kendall, C.G.St.C, Posamentier, H.W., Ross C.A., and Van Wagoner, J.C., eds., Sea Level Changes—An Integrated Approach: SEPM Special Publication 42, p. 125–154.

POSAMENTIER, H.W., ALLEN, G.P., JAMES, D.P., TESSON, M., 1992, Forced regressions in a sequence stratigraphic framework; concepts, examples, and exploration significance: AAPG Bulletin, v. 76, p. 1687–1709.

DE RAAF, J.F.M., and BOERSMA J.R., 1971, Tidal deposits and their sedimentary structures: Netherlands Journal of Geosciences (Geologie en Mijnbouw), v. 50, p. 479–503.

RAISWELL, R., and FISHER, Q.J., 2000, Mudrock-hosted carbonate concretions: a review of growth mechanisms and their influence on chemical and isotopic composition: Journal of the Geological Society, London, v. 157, p. 239–251.

RAISWELL, R., BOTTRELL, S.H., DEAN, S.P., MARSHALL, J.D., CARR, A., and HATFIELD, D., 2002, Isotopic constraints on growth conditions of multiphase calcite-pyrite-barite concretions in Carboniferous mudstones: Sedimentology, v. 49, p. 237–254.

SAHA, S., GHOSH, A., BANERJEE, S., SARASWATI, P.K, and BURLEY, S.D., 2011, Characteristic of an open coast tidal flat: example from Daman, West Coast of India: Journal Geological Society of India, v. 77, p. 409–418.

SCHMUDE, D.E., 2000, Interplay of paleostructure, sedimentation, and preservation of Middle Jurassic rocks, Bighorn Basin, Wyoming: The Mountain Geologist, v. 37, p. 145–155.

SEILACHER, A., 2007, Trace Fossil Analysis: Berlin, Springer, 226 p.

SHANLEY, K.W., and MCCABE, P.J., 1991, Predicting facies architecture through sequence stratigraphy: an example from the Kaiparowits Plateau, Utah: Geology, v. 19, p. 742–745.

SPECHT, R.W., and BRENNER, R.L., 1979, Storm-wave genesis of bioclastic carbonates in Upper Jurassic epicontinental mudstones, east-central Wyoming: Journal of Sedimentary Petrology, v. 49, p. 1307–1322.

STEINER, M.B., 1998, Age, correlation, and tectonic implications of Morrison Formation paleomagnetic data, including rotation of the Colorado Plateau: Modern Geology, v. 22, p. 261–281.

TANKARD, A.J., 1986, Depositional response to foreland deformation in the Carboniferous of eastern Kentucky: AAPG Bulletin, v. 70, p. 853–868.

UFNAR, D.F., 1994, Sedimentologic and taphonomic analysis of the Jurassic Windy Hill sandstone member, (upper Sundance Formation), northeastern Big Horn Basin, Wyoming [M.S. Thesis]: Vanderbilt University, Nashville, Tennessee, 124 p.

UHLIR, D.M., AKERS, A., and VONDRA, C.F., 1988, Tidal inlet sequence, Sundance Formation (Upper Jurassic), north-central Wyoming: Sedimentology, v. 35, p. 739–752.

VAN WAGONER, J.C., MITCHUM, R.M., CAMPION, K.M., and RAHMANIAN, V.D., 1990, Siliciclastic sequence stratigraphy in well logs, cores, and outcrops; Concepts for high-resolution correlation of time and facies: AAPG Methods in Exploration Series, No. 7, 55 p.

VAN WAGONER, J.C., 1991, High-frequency sequence stratigraphy and facies arhcitecture of the Sego Sandstone in the Book Cliffs of western Colorado and eastern Utah, *in* Van Wagoner, J.C., Nummendal, D., Jones, C.R., Taylor, D.R., Jennette, D.C., and Riley, G.W., eds., Sequence Stratigraphy Applications to Shelf Sandstone Reservoirs: Outcrop to Subsurface Examples: American Association of Petroleum Geologists, Field Conference, p. 1–22.

VASUKI, Y., HOLDEN, E.-J., KOVESI, P., and MICKLETHWAITE, S., 2014, Semi-automatic mapping of geological structures using UAV-based photogrammetric data: An image analysis approach: Computers and Geoscience, v. 69, p. 22–32.

WHITE, T., FURLONG, K., and ARTHUR, M., 2002, Forebulge migration in the Cretaceous Western Interior Basin of the central United States: Basin Research, v. 14, p. 43–54.

WILLIS, B.J, and FITRIS, F., 2012, Sequence stratigraphy of Miocene tide-influenced sandstones in the Minas field, Sumatra, Indonesia: Journal of Sedimentary Research, v. 82, p. 400–421.

WILLIS, B.J., and GABEL, S.L., 2001, Sharp-based, tide-dominated deltas of the Sego Sandstone, Book Cliffs, Utah, USA: Sedimentology, v. 48, p. 479–506.

WILLIS, B.J., and GABEL, S.L., 2003, Formation of deep incisions into tide-dominated river deltas: implications for the stratigraphy of the Sego Sandstone, Book Cliffs, Utah, U.S.A.: Journal of Sedimentary Research, v. 73, p. 246–263.

WRIGHT, R.P., 1971, The marine Jurassic of Wyoming and South Dakota; its paleoenvironment and paleobiology [Ph.D. Dissertation]: Michigan University, Ann Arbor, Michigan, 167 p.

WRIGHT, R.P., 1974, Storm-generated coquinoid sandstone: Genesis of high-energy marine sediments from the Upper Jurassic of Wyoming and Montana: Discussion: Geological Society of America Bulletin, v. 85 p. 837.

YANG, B.C., DALRYMPLE, R.W., and CHUN, S.S., 2005, Sedimentation on a wave-dominated, open-coast tidal flat, south-western Korea: summer tidal flat—winter shoreface: Sedimentology, v. 52, p. 235–252.

YOSHIDA, S., STEEL, R.J., and DALRYMPLE, R.W., 2007, Changes in depositional processes - An ingredient in a new generation of sequence stratigraphic models: Journal of Sedimentary Research, v. 77, p. 447–460.

ZEINER, T.C., 1974, Upper Sundance – lower Morrison sedimentology, Wyoming, and its stratigraphic implications [M.A. Thesis]: Univeristy of Missouri, Columbia, Missouri, 92 p.

ZHU, Y., BHATTACHARYA, J.P., LI, W., LAPEN, T.J., JICHA, B.R., and SINGER, B.S., 2012, Milankovitch-scale sequence stratigraphy and stepped forced regressions of the Turonian Ferron Notom deltaic complex, south-central Utah, U.S.A.: Journal of Sedimentary Research, v. 82, p. 723–746.

APPENDIX A

EQUATIONS AND CODE USED IN UAV-BASED METHODS

Calculation of Best Fit Plane using Least-squares

For a plane of the form of

$$z = Ax + By + C$$

the coefficients A, B, and C that describe this plane are found by solving the linear set of equations (Davis 2002):

$$\begin{bmatrix} \sum_{i=1}^{m} x_i^2 & \sum_{i=1}^{m} x_i y_i & \sum_{i=1}^{m} x_i \\ \sum_{i=1}^{m} x_i y_i & \sum_{i=1}^{m} y_i^2 & \sum_{i=1}^{m} y_i \\ \sum_{i=1}^{m} x_i & \sum_{i=1}^{m} y_i & \sum_{i=1}^{m} 1 \end{bmatrix} \begin{bmatrix} A \\ B \\ C \end{bmatrix} = \begin{bmatrix} \sum_{i=1}^{m} x_i z_i \\ \sum_{i=1}^{m} y_i z_i \\ \sum_{i=1}^{m} z_i \end{bmatrix}$$

where x_i, y_i, and z_i refer to the i^{th} values, and n is the number of points measured on the bedding surface.

Calculation of Strike, Dip, and Dip-direction

Strike is calculated as the line (s) formed by the intersection of the horizontal plane (h) and the plane of the bed (a), given by the cross-product of those two planes:

$$s = \begin{bmatrix} A & B & C \end{bmatrix} \times \begin{bmatrix} 0 & 0 & 1 \end{bmatrix}$$

This strike must be subsequently converted from a unit circle reference frame to a compass-direction reference frame. Dip direction lies at 90° to strike, with the direction determined by the slope of the best-fit plane. Dip (d) is calculated as

$$d = arctan(A\sqrt{B^2/A^2 + 1}))$$

Rotation of Point Cloud

From the dip and dip direction, the entire point cloud is rotated to return bedding to a horizontal position. This rotation is accomplished in three steps, first by a horizontal clockwise rotation of the point cloud (P) so that the dip direction (g) points in a positive direction along the x-axis, which simplifies the rotation to remove the dip. For example, if the point cloud consists of six columns, with x, y, and z coordinates in the first three columns, followed by three additional data columns, such as the red, green, and blue color values of each point, the first rotation operation would be:

$$P' = P \begin{bmatrix} cos(g) & sin(g) & 0 & 0 & 0 & 0 \\ -sin(g) & cos(g) & 0 & 0 & 0 & 0 \\ 0 & 0 & 1 & 0 & 0 & 0 \\ 0 & 0 & 0 & 1 & 0 & 0 \\ 0 & 0 & 0 & 0 & 1 & 0 \\ 0 & 0 & 0 & 0 & 0 & 1 \end{bmatrix}$$

In this example, the fourth through sixth columns and rows are the identity matrix, which preserves unchanged any additional information stored in the point cloud, such as color values or other attributes. The number of rows and columns of these rotation matrices must equal the number of columns in the point cloud data. From this horizontally rotated point cloud (P'), a second rotation is applied to remove the dip (d):

$$P'' = P' \begin{bmatrix} 1 & 0 & 0 & 0 & 0 & 0 \\ 0 & cos(d) & sin(d) & 0 & 0 & 0 \\ 0 & -sin(d) & cos(d) & 0 & 0 & 0 \\ 0 & 0 & 0 & 1 & 0 & 0 \\ 0 & 0 & 0 & 0 & 1 & 0 \\ 0 & 0 & 0 & 0 & 0 & 1 \end{bmatrix}$$

Finally, this doubly-rotated point cloud (P") is rotated horizontally counter-clockwise to return it to its correct orientation relative to geographic north, in effect, undoing the first of the three rotations:

$$P''' = P'' \begin{bmatrix} cos(g) & -sin(g) & 0 & 0 & 0 & 0 \\ sin(g) & cos(g) & 0 & 0 & 0 & 0 \\ 0 & 0 & 1 & 0 & 0 & 0 \\ 0 & 0 & 0 & 1 & 0 & 0 \\ 0 & 0 & 0 & 0 & 1 & 0 \\ 0 & 0 & 0 & 0 & 0 & 1 \end{bmatrix}$$

Code for the Above Calculations

R code for calculation of a best-fit plane to a series of x-y-z coordinates obtained from a bed, using the method of least squares, for calculating the dip and dip direction from the best-fit plane, and for rotating a point cloud based on dip and dip direction. Most of these are helper functions for the few functions that need to be called, as shown in the example workflow below:

```
# Fit a plane to points from one bed that should be horizontal.
# x, y, z are the coordinates of points on that bed from the point cloud.
bestFitPlane <- planeForPoints(x, y, z)

# Optionally, the r-squared of the fitted plane can be calculated.
rSquaredPlane(x, y, z, bestFitPlane)

# The dip and dip direction (and optionally, the strike) of the fitted plane
# should be calculated.
dip <- dip(bestFitPlane)
dipDirection <- dipDirection(bestFitPlane)
strike <- strike(bestFitPlane)

# Using these, the entire point cloud can be rotated so that all bedding
# is horizontal.
rotatedPointCloud <- flattenDip(pointCloud, dipDirection, dip)

# The rotated point cloud can now be opened in the point-cloud software.
# At this point, the z-coordinate is stratigraphic position, allowing
# stratigraphic thicknesses to be measured.

# FUNCTIONS ---------------------------------------------------------------

planeForPoints <- function(x, y, z) {
# 3 Planar Fitting of 3D Points of Form (x, y, f(x,y))
# returns column vector [A, B, C], where z = Ax + By + C

  xi <- sum(x)
  yi <- sum(y)
  zi <- sum(z)
  xi2 <- sum(x^2)
  yi2 <- sum(y^2)
  xiyi <- sum(x*y)
  xizi <- sum(x*z)
  yizi <- sum(y*z)
  n <- length(x)
  M1 <- matrix(data=c(xi2, xiyi, xi, xiyi, yi2, yi, xi, yi, n), nrow=3)
  M2 <- matrix(data=c(xizi, yizi, zi), nrow=3)
  solution <- solve(M1, M2)
  return(solution)
}

rSquaredPlane <- function(x, y, z, plane) {
  # plane is the output of planeForPoints(), a column vector [A, B, C],
  #   where z-hat = Ax + By + C
  zHat <- plane[1]*x + plane[2]*y + plane[3]
  SSE <- sum((z-zHat)^2)
  SST <- sum((z-mean(z))^2)
  Rsquared <- 1 - SSE/SST
  Rsquared
}
```

```
vcrossprod <- function(a, b) {
  # returns line that forms intersection of two planes a and b
  # returns column vector [x, y, z] of the line in three dimensions
  c1 <- a[2]*b[3] - a[3]*b[2]
  c2 <- a[3]*b[1] - a[1]*b[3]
  c3 <- a[1]*b[2] - a[2]*b[1]
  c <- matrix(c(c1, c2, c3), nrow=3)
  return(c)
}

azimuthFromUnitCircle <- function(theta) {
  # converts angle theta on a unit circle to compass azimuth
  #  - unit circle has origin at 90° on compass with values increasing
counterclockwise
  #  - need origin at 0° on compass with values increasing clockwise
  # input and output are in degrees, not radians
  azimuth <- 450 - theta
  if (azimuth > 360) {
    azimuth = azimuth - 360
  }
  return(azimuth)
}

strike <- function(a) {
  # returns the azimuth of the strike (in degrees) of plane a
  #   where strike is the intersection of plane a and the horizontal plane.
  #   uses east-half rule (i.e., strike is always 0-180°)
  horizontalPlane <- matrix(data=c(0,0,1), nrow=3)
  strikeLine <- vcrossprod(a, horizontalPlane)
  theta <- atan(strikeLine[2]/strikeLine[1]) * 180 / pi
  azimuth <- azimuthFromUnitCircle(theta)
  return(round(azimuth, 1))
}

dipDirection <- function(a) {
  # returns the azimuth of the dip direction (in degrees) from plane a
  strikeAzimuth <- strike(a)
  xSlope <- a[1]
  ySlope <- a[2]
  dipAzimuth <- strikeAzimuth
  if (xSlope > 0) {
    if (ySlope >= 0) {
      dipAzimuth <- strikeAzimuth - 90    # SE dip
    } else {
      dipAzimuth <- strikeAzimuth + 90    # NW dip
    }
  } else {
    if (ySlope > 0) {
      dipAzimuth <- strikeAzimuth - 90    # SW dip
    } else {
      dipAzimuth <- strikeAzimuth + 90    # NE dip
    }
  }
  return(dipAzimuth)
}

dip <- function(a) {
  # returns the true dip (in degrees) of plane a
  xSlope <- a[1]
  ySlope <- a[2]
  if (xSlope == 0) {  # add negligible amounts to prevent dividing by zero
    xSlope <- 0.000001
  }
  if (ySlope == 0) {
```

```
    ySlope <- 0.000001
  }
  alphaX <- atan(xSlope)
  alphaY <- atan(ySlope)
  dipRadians <- atan(tan(alphaX) * sqrt(tan(alphaY)^2 / tan(alphaX)^2 + 1))
  dipDegrees <- dipRadians * 180 / pi
  if (dipDegrees < 0) {
    dipDegrees = - dipDegrees
  }
  return(round(dipDegrees, 1))
}

flattenDip <- function(surface, dipDirection, dip) {
  # Returns coordinates on point cloud surface that has been rotated to
  # make bedding horizontal. Point cloud surface should contain x coordinate
  # in column 1, y in column 2, and z in column 3. Point cloud surface may
  # contain additional columns of data that will also be returned, unchanged
  # by the rotation. The values of dipDirection and dip should be in degrees,
  # not radians. The functions dipDirection() and dip(), shown above, return
  # their results in degrees.

  colnames <- colnames(surface)
  surface <- as.matrix(surface)

  # rotate the dip direction first (x-y plane)
  dipDirectionRadians <- dipDirection / 180 * pi
  operator <- diag(ncol(surface))
  operator[1, 1] <-  cos(dipDirectionRadians)
  operator[2, 1] <- -sin(dipDirectionRadians)
  operator[1, 2] <-  sin(dipDirectionRadians)
  operator[2, 2] <-  cos(dipDirectionRadians)
  firstRotation <- surface %*% operator

  # rotate the dip second (y-z plane)
  dip <- - dip  # dip is downward
  dipRadians <- dip / 180 * pi
  operator <- diag(ncol(surface))
  operator[2, 2] <-  cos(dipRadians)
  operator[3, 2] <- -sin(dipRadians)
  operator[2, 3] <-  sin(dipRadians)
  operator[3, 3] <-  cos(dipRadians)
  secondRotation <- firstRotation %*% operator

  # back-rotate the dip direction to restore original x-y coordinates
  operator <- diag(ncol(surface))
  operator[1, 1] <-  cos(dipDirectionRadians)
  operator[2, 1] <-  sin(dipDirectionRadians)
  operator[1, 2] <- -sin(dipDirectionRadians)
  operator[2, 2] <-  cos(dipDirectionRadians)
  thirdRotation <- secondRotation %*% operator

  rotatedData <- data.frame(thirdRotation)
  colnames(rotatedData) <- colnames
  return(rotatedData)
}

deg2rad <- function(theta) {
  # converts angles in degrees to radians
  theta/180 * pi
}

rad2deg <- function(theta) {
  # converts angles in radians to degrees
  theta/pi * 180
```

```
}
```

Bootstrapping Code

```
# Creates a bootstrapped distribution of dip measurements with 95% confidence
intervals.
# In example below 'data' refers to the entire set of points picked on an
individual bedding plane.
# n can be varied between 3 and the number of points in the initial data set.
40 is shown in example below because it was determined to be the threshold
value after which estimates of dip did not appreciably change. 10000
iterations were used for all trials in this study.

# Required Parameters
n <- 40
iterations <- 10000
confidence <- 0.95

# Function: Assigns indices to rows in the data table and randomly samples
'n' rows with replacement, then builds a new data frame from these rows. Uses
this new data frame to calculate a best-fit plane using a least-squares
regression and then calculates and returns the dip of that plane. See
function planeForPoints and Dip in previous section for more information.

bootstrappedDip <- function(data, n) {
      indices <- 1:nrow(data)
      bootstrappedIndices <- sample(indices, size=n, replace=TRUE)
      bootstrappedFrame <- data[bootstrappedIndices, ]
      plane <- planeForPoints(bootstrappedFrame$X, bootstrappedFrame$Y,
bootstrappedFrame$Z)
      dip(plane)
}

# Distribution is then built by calling function many times
bootstrap <- replicate(iterations, bootstrappedDip(data, n))

# Calculate dip estimate and uncertainty
mean(bootstrap)                      # estimate
quantile(bootstrap, 1-confidence)    # lower limit
quantile(bootstrap, confidence)      # upper limit
```

Bootstrapped Dip Plots

Plots of bootstrapped dip estimates and 95% confidence interval for individual beds:

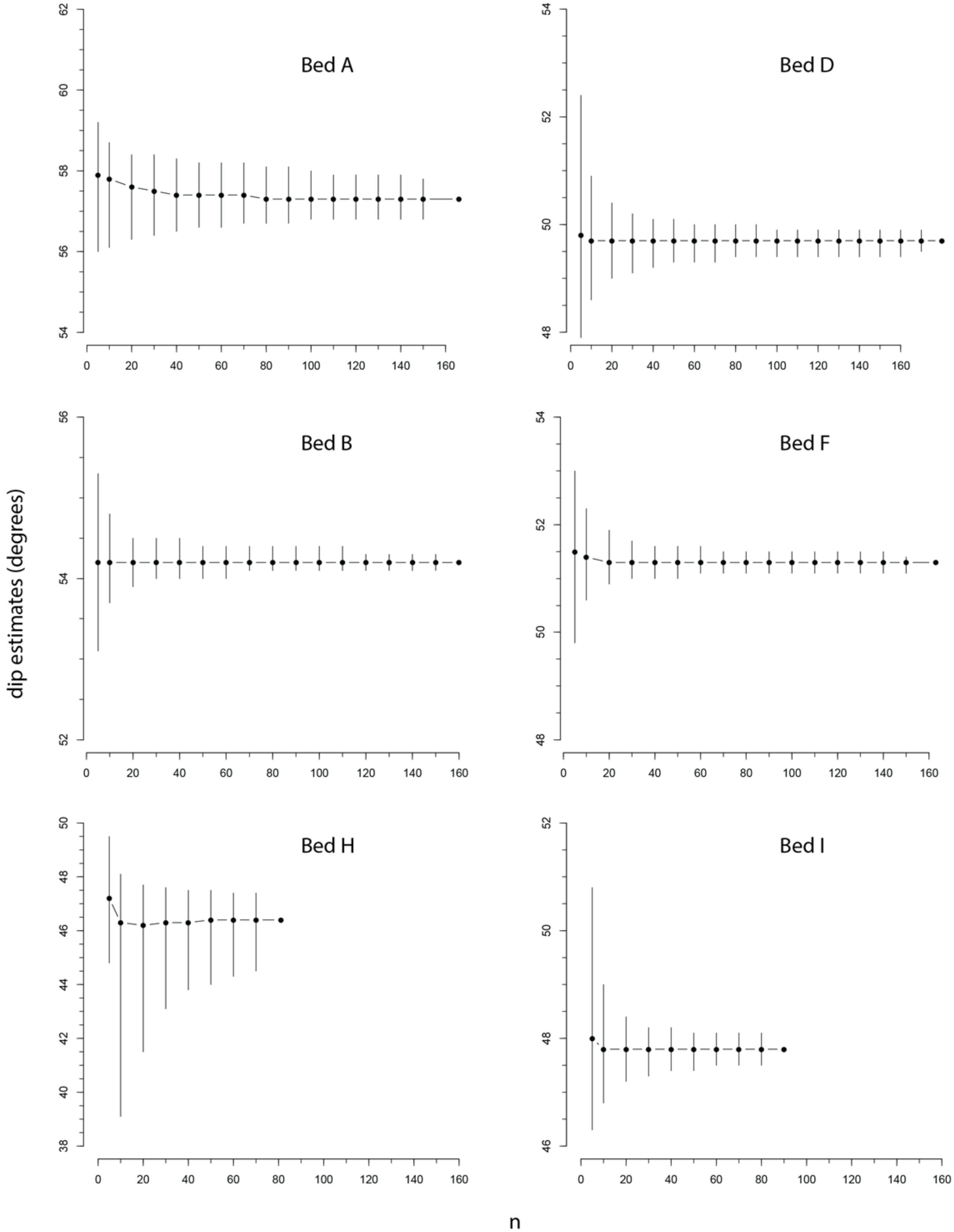

APPENDIX B

SAMPLES AND THIN SECTIONS

Facies Associations: SA=Shoreface Association, TCA=Tidal Flat Association, WDSA=Wave-dominated Shelf Association, APA=Alluvial Plain Association.

Name	**Location**	**Position**	**Facies Association**	**Facies**	**Thin Section**
RG3a	Red Gulch SWA	6.2 m	SA	Sd-lc	Y
RG3b	Red Gulch SWA	6.2 m	SA	Sd-lc	Y
RG1	Red Gulch SWD	1.4 m	SA	Las	Y
RG2	Red Gulch SWD	3.5 m	SA	Las	Y
RGRW1	Red Gulch SWG	0.1 m	SA	Gst	Y
SheepSWC1	Sheep SWC	8.2 m	TFA	Sd-ch	
SWC2	Sheep SWC	7.9 m	TFA	Sd-ch	Y
SWF1	Sheep SWF	51.5 m	TFA	Sr-t/Sp/Sm	
SheepSWD1	Sheep SWD	0.1 m	SA	Gc	
SWD2	Sheep SWD	4.2 m	WDSA/SA	M/Sr-s	Y
SWDS1	Sheep SWD Supp.	15.4 m	APA	Sd-a	Y
SMA1	Sheep SWA	11.7 m	SA	Gsd	Y
SWH1	Sheep SWH	6.8 m	TFA	Gtl	Y
SWH2	Sheep SWH	7.0 m	APA?	Sp-a	Y
SWLRW1	Sheep SWL	3.1 m	SA	Gc	Y
SWL2	Sheep SWL	15.5 m	TFA	Sr-t/Sp/Sm	Y
SWLM3	Sheep SWL	31.8 m	APA?	Sm?	Y
SWMRW1	Sheep SWM	7.6 m	WDSA?/SA	M/Sr-s?	Y
RD1	Red Dome SW	2 m	TFA	Sr-t/Sp/Sm	Y
RD2	Red Dome SW	13.6 m	WDSA/SA	M/Sr-s	Y

RD3a	Red Dome SW	14 m	TFA	Sr-t/Sp/Sm	Y
RD3b	Red Dome SW	14 m	TFA	Sr-t/Sp/Sm	Y
RD4	Red Dome SW	14.3	TFA	Sr-t/Sp/Sm	Y
SW1	Thermopolis SW	0.5 m	SA	Gc	
SW2	Thermopolis SW	1.5 m	SA	Sd-lc	Y
SW3	Thermopolis SW	5.7 m	SA	Gst	Y
SW4	Thermopolis SW	10.5 m	SA	Sd-lc	Y
SW5	Thermopolis SW	15.4 m	TFA	Sr-t	
SW6	Thermopolis SW	31.5 m	APA	Sm-a?	Y
SDSW1	Seminoe Dam SW	8.0 m	SA?	Sr-s?	Y
SDSW2	Seminoe Dam SW	3.6 m	APA?	Sd-a	
SDSW3	Seminoe Dam SW	21.0 m	APA	Sd-a	Y
AESW1	Alcova East SW	4.5 m	SA	Gc	
AESW2	Alcova East SW	5.3 m	TFA	Sr-t/Sm/Sp	Y
AESW3	Alcova East SW	6.8 m	APA?	Sr-a?	Y
CCSW1	Cottonwood Creek SW	7.6 m	TFA	Sr-t	
CCSW2	Cottonwood Creek SW	13.6 m	APA	Sm-a?	Y

APPENDIX C

LOCALITIES

All coordinates are based on the WGS84 global reference system. Sections that were digitally measured with data obtained from quadcopter UAV are indicated by an asterisk.

Locality Name	**Longitude (°W)**	**Latitude (°N)**
Alcova East SW	-106.68391	42.53262
Camp Skeeter SW	-108.24412	44.69333
Camp Skeeter SW East	-108.24364	44.69326
*Camp Skeeter SW West	-108.24524	44.69334
Cottonwood Creek SW	-106.72655	42.50928
Gypsum Spring SW	-108.42121	45.00704
*Gypsum Spring SW North	-108.42118	45.00779
Newton Lakes	-109.12267	44.54500
*Newton Lakes West	-109.12381	44.54553
*Red Dome SW	-108.83316	45.21835
Red Gulch SWA	-107.81043	44.47059
Red Gulch SWB	-107.81006	44.47072
Red Gulch SWC	-107.81143	44.47203
Red Gulch SWD	-107.81225	44.46995
Red Gulch SWE	-107.80987	44.47304
Red Gulch SWF	-107.80991	44.47378
Red Gulch SWG	-107.80933	44.47512
*Red Gulch SWH	-107.81262	44.47011
*Red Gulch SWI	-107.81310	44.47000
*Red Gulch SWJ	-107.81258	44.47126
*Red Gulch SWK	-107.80897	44.47033
Seminoe Dam SW	-106.91127	42.12273
*Pantosaurus SW	-108.02512	44.53042

Sheep SWA	-108.04257	44.56978
Sheep SWA SE Supplemental	-108.04208	44.56926
Sheep SWA NW Supplemental	-108.04231	44.56985
*Sheep SWA Drone	-108.03974	44.56746
Sheep SWB	-108.02723	44.55262
Sheep SWC	-108.02273	44.53683
Sheep SWD	-108.03697	44.56237
Sheep SWD Supplemental	-108.03635	44.56306
*Sheep SWDA	-108.03769	44.56519
Sheep SWE	-108.03017	44.55604
Sheep SWF	-108.02461	44.54377
Sheep SWG	-108.05935	44.58054
Sheep SWH	-108.05284	44.57717
Sheep SWI	-108.07055	44.58525
Sheep SWJ	-108.08041	44.59093
Sheep SWK	-108.08994	44.59538
Sheep SWL	-108.10075	44.59984
Sheep SWM	-108.10792	44.60397
Thermopolis SW	-108.17967	43.67436